Drift instabilities, anomalous transport, and heating in low-temperature plasmas

A dissertation submitted to the
College of Graduate and Postdoctoral Studies
in partial fulfillment of the requirements
for the degree of Doctor of Philosophy
in the Department of Department of Physics and Engineering Physics
University of Saskatchewan
Saskatoon

By
Arash Tavassoli

Permission to Use

In presenting this dissertation in partial fulfillment of the requirements for a Postgraduate degree from the University of Saskatchewan, I agree that the Libraries of this University may make it freely available for inspection. I further agree that permission for copying of this dissertation in any manner, in whole or in part, for scholarly purposes may be granted by the professor or professors who supervised my dissertation work or, in their absence, by the Head of the Department or the Dean of the College in which my dissertation work was done. It is understood that any copying or publication or use of this dissertation or parts thereof for financial gain shall not be allowed without my written permission. It is also understood that due recognition shall be given to me and to the University of Saskatchewan in any scholarly use which may be made of any material in my dissertation.

Disclaimer

Reference in this dissertation to any specific commercial products, process, or service by trade name, trademark, manufacturer, or otherwise, does not constitute or imply its endorsement, recommendation, or favoring by the University of Saskatchewan. The views and opinions of the author expressed herein do not state or reflect those of the University of Saskatchewan, and shall not be used for advertising or product endorsement purposes.

Requests for permission to copy or to make other uses of materials in this dissertation in whole or part should be addressed to:

Head of the Department of Physics and Engineering Physics
163 Physics Building
116 Science Place
University of Saskatchewan
Saskatoon, Saskatchewan
Canada
S7N 5E2

OR

Dean
College of Graduate and Postdoctoral Studies
University of Saskatchewan
116 Thorvaldson Building, 110 Science Place
Saskatoon, Saskatchewan S7N 5C9 Canada

Abstract

Plasma is an ideal gas of charged particles (ions and electrons) in addition to neutral particles. The presence of charged particles results in the generation of electric and magnetic fields that serve as the primary mechanism of the interaction and coupling of particles. As a result, various nonlinear collective phenomena occur in the plasma, the understanding of many of which remains elusive today. On the other hand, plasmas have many applications in different branches of science and technology. Different kinds of plasmas are studied in the atmospheric and space sciences. In the semiconductor industry, the fabrication of electronic chips relies heavily on plasma etching. Plasma is used in modern electrical thrusters for producing the driving force of satellites and spacecrafts. It is also used in future fusion reactors for producing abundant clean energy. Therefore, understanding the complicated phenomena in plasma is important for predicting and controlling its behaviours in various conditions. In this regard, nonlinear phenomena, such as turbulence, are formidable barriers to understanding plasma behaviours. These phenomena are described by nonlinear differential equations that can be barely understood by analytical means and are usually investigated by numerical simulations. Because of this, it is also important to understand the effect of numerical artifacts on simulations.

In this thesis, we investigate the nonlinear characteristics of drift instabilities and the role of numerical methods in our understanding of these instabilities. The drift instabilities are driven by excess free energy that exists due to the average (drift) velocities of electron and ion components in plasmas. As a result of these instabilities, the amplitude of fluctuations grows while the drift energy converts into electrostatic energy. This growth continues until the nonlinear effects, such as turbulence, trapping, and wave-wave interactions, become active. As a result of these nonlinear effects, the growth of the fluctuations saturates.

In this thesis, our focus will be on two particular types of drift instabilities, namely the Buneman instability and electron-cyclotron drift instability (ECDI). The Buneman instability is driven when a beam of electrons is injected into the stationary ions, while both electrons and ions are unmagnetized. In the ECDI, however, the electrons are magnetized and are also influenced by an external electric field, perpendicular to the magnetic field. This configuration of fields leads to the $E \times B$ drift of the electrons that drives the ECDI. Many kinetic simulations are performed, and several nonlinear phenomena such as trapping, heating, anomalous transport, backward waves, and transition of magnetized plasmas to the unmagnetized regime are studied with regard to both instabilities. For the study of the nonlinear effects of drift instabilities, a grid-based Vlasov code is developed and used. The numerical method used in this code is the "semi-Lagrangian" method, which is among the most popular methods for continuum simulations of plasma. In the study of the drift instabilities, we compare the results of the semi-Lagrangian Vlasov simulations with the more traditional particle-in-cell (PIC) method. The results of these benchmarking studies reveal several similarities and discrepancies between Vlasov and particle-in-cell simulations, showing how the numerical methods can interfere with the physics of the problems.

Acknowledgements

I would like to heartily appreciate the great support of my beloved family; Soheila Boroujerdian, Ahmad Tavassoli, Azin Tavassoli, Pouyan Ahmadpanah, and Sooshi Tavassoli. Moreover, I gratefully acknowledge the support of my supervisors Profs. Andrei Smolyakov and Raymond Spiteri. I acknowledge the fundamental backing of Dr. Magdi Shoucri for developing the numerical code used in this dissertation and for his illuminating guidance. I am deeply grateful to all my groupmates in Theoretical Plasma Physics and the Numerical Simulation Lab of the University of Saskatchewan; especially Mina Papahn Zedeh, Oleksandr Chapurin, and Kevin Green whose support particularly helped. Part of this dissertation is based on a published article that is co-authored by Lénaïc Couëdel, Marilyn Jimenez, Meghraj Sengupta, and Trevor Zintel, whose contribution is greatly appreciated. Many thanks to my friends, Mojtaba Abdollahnejad, Mohsen Asadi Bagloue, Farzin Tayarani, Sana Daneshamouz, Mina Tayarani, Mahta Abdollahzadeh Zare, William Elock, Andy Sabo, Shahab Bahreini, Abbas Mehraban, Alireza Zangouie, and Mohsen Zarepour for all their support during my work on this dissertation.

To Mother Nature, for her endless support.

Contents

List of Tables

List of Figures

List of Abbreviations

SPT	Stationary plasma thruster
ECDI	Electron cyclotron drift instability
PIC	Particle-in-cell
αD	α spatial dimensions, considered in the Vlasov equation.
αDβV	α spatial directions and β velocity directions, considered in the Vlasov equation
MTSI	Modified two-stream instability
PPC	Particles per cell
FFT	Fast Fourier transform
DFT	Discrete Fourier transform
CFL	Courant-Friedrichs-Lewy
SNR	Signal to noise ratio
SE	Standard error
VDF	Velocity distribution function
ps	Picoseconds
ns	Nanoseconds
RHS	Right hand side
ES	Electrostatic

1 Introduction

1.1 Motivation and thesis outline

Plasma is an ionized gas that consists of charged particles and, sometimes, neutral particles. It is considered the most abundant substance in the observable universe. Plasma exists in different layers of the Earth's atmosphere and contributes to many atmospheric phenomena that can affect life on our planet. Although plasma does not naturally exist around us, it is artificially created and used for many industrial purposes, such as chip etching in semiconductor industries [1], plasma propulsion in space industries [2], and in future nuclear fusion reactors [3]. Due to its various applications, it is important to understand the underlying mechanism of many complicated behaviours that plasmas can exhibit. However, many of these phenomena are described by nonlinear differential equations that can be barely understood by analytical means. In the modern era, the study of nonlinear plasma behaviours largely depends on computational simulations. Therefore, understanding the numerical methods and their signature on the simulations is an important part of these studies.

In space industries, plasma thrusters are a modern technology for producing the driving force of space vehicles. The main advantage of this type of thruster over traditional chemical thrusters is their higher mass efficiency. The reason for this mass efficiency is the high velocity of propellants, achieved at the exhaust of the thruster, that allows for a smaller mass fraction of the carried fuel [4, 5]. One of the commonly used plasma thrusters is the Hall thruster, also called "stationary plasma thruster" (SPT) [6, 7]. Fig. 1.1 shows a schematic of the Hall thruster. It can be seen that the Hall thruster has a cylindrical geometry with the axial, radial, and azimuthal axes. The ions are created by the ionization of the neutral atoms that are injected at the anode location. The electrons are emitted by a hollow cathode, and some of them travel towards the anode [7]. The electrons are required to create plasma through ionization in the region close to the anode (called the "ionization region") and also to neutralize the extracted ions in the exhaust (plume) region.

Between the anode and the cathode, an electric field is generated inside the plasma in the axial direction (Fig. 1.1). The electric field is largest (about 20000 V/m or more) closer to the exhaust, in a region called the "acceleration region", but it is much smaller in the ionization region [6]. This electric field extracts the heavy ions (usually Xenon or Argon) from the thruster producing the thrust. To efficiently generate a large electric field in the acceleration region, the electron mobility in the axial direction must be small. Therefore, a radial magnetic field is generated to trap the electrons and reduce their axial mobility. The ions, however, remain mainly unmagnetized because their Larmour radius is larger than the dimensions of the plasma channel.

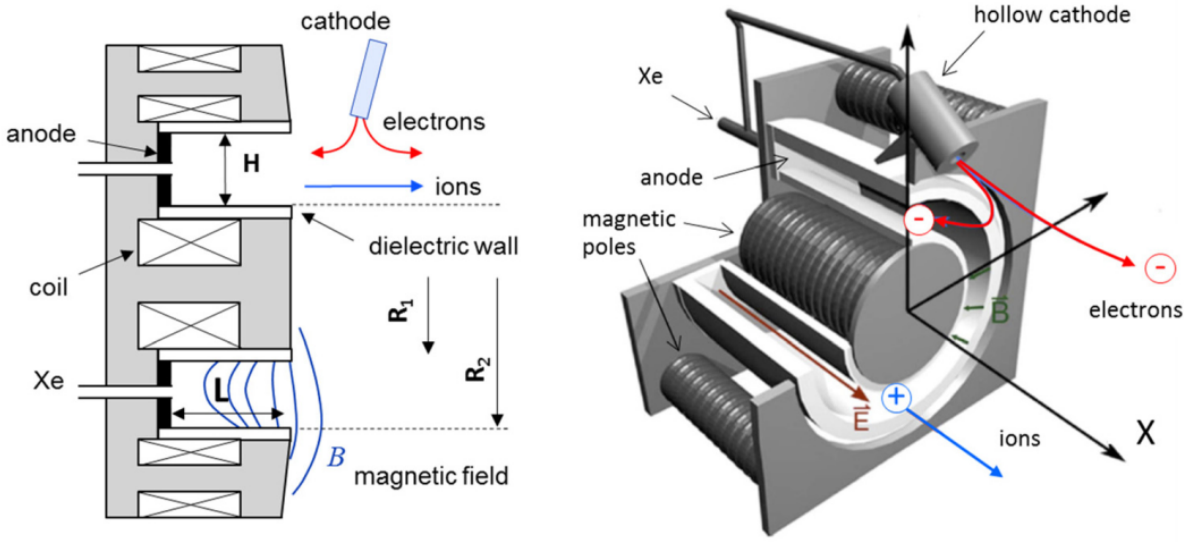

Figure 1.1: A schematic figure of the Hall thruster. The left shows a side view of the right. This figure is taken from Ref. [6].

The axial electron current in the thruster is required to provide energy input to the plasma and sustain the discharge. The classical theory of the cross-field transport predicts that the axial electron current can be generated due to collisions [8, 5]. However, it is widely believed that the collision frequency of the electrons is not enough to generate the axial mobility that is inferred from the experimental evidence [9]. The axial electron mobility that is beyond the predictions of the classical theory is called "anomalous mobility". The origin of anomalous transport has been the subject of many discussions [6]. It is believed that the fluctuations in the azimuthal direction can be an important reason behind anomalous transport. The leading theory for explaining such fluctuations is the electron cyclotron drift instability (ECDI), also called the electron drift instability (EDI) [10, 11, 12, 8, 9, 13].

The ECDI is driven by the $E \times B$ drift velocity of the electrons, whereas such drift is absent for unmagnetized ions. This instability is particularly important in the acceleration region, where the electric field is large and other effects, such as the magnetic field or density gradient, are not important. Various simulations and calculations have shown the generation of cross-field anomalous current in the nonlinear regime of the ECDI [10, 14, 15, 11, 12, 8, 9, 13]. In simulations, this process happens in conjunction with fast heating that is well above the experimental values. The details of these are still not well understood [8, 11, 12, 14].

Another class of instabilities that are relevant to the anomalous current and the operation of Hall thrusters are the unmagnetized drift instabilities, in particular, the Buneman-type and ion-sound instabilities. These instabilities are driven by the relative drift velocity between the electrons and ions and can be investigated as a proxy for understanding nonlinear effects and anomalous transport. The Buneman-type instabilities are considered an important source of the electric potential in the hollow cathodes used in the Hall thrusters,

which create high energy ions [16, 17, 18, 19].

Another problem addressed by our studies is the relation of the ECDI to the ion-sound modes. In the linear regimes, the linear ECDI is reduced to the unmagnetized ion-sound instability when there is considerable propagation along the magnetic field [12]. Even for exclusive propagation across the magnetic field, a theory suggests that the ECDI will reduce to the ion-sound instability in its nonlinear regime [20, 21]. This theory is, however, debated by some other studies [11, 12, 22, 23].

The implications of the study of drift instabilities reach far beyond plasma propulsion. The ECDI has also been demonstrated and studied in the collisionless shockwaves [24, 25]. The Buneman-type instabilities are used for explaining the turbulence and anomalous resistivity in space sciences [26, 27, 28, 29, 30] for generating the short-wavelength radiations [31] and for compressing the beams of charged particles [32].

Numerical methods are an indispensable tool for investigating nonlinear phenomena such as anomalous transport and heating. Different physical models are suggested for the simulation of plasmas. In some fluid models, the anomalous mobility is used empirically to make the results of the simulation consistent with experimental observations (e.g., in Ref. [33]). In kinetic simulations, such as in our studies, the anomalous transport emerges from the underlying dynamics of the plasma. The particle-in-cell (PIC) is a popular method for kinetic simulations. The kinetic simulations are computationally much more intensive than the fluid simulations. To decrease the computational cost of the PIC simulations, a limited number of markers are usually used. This can lead to unwanted noise, which can compromise the accuracy of the results. Therefore, it is important to verify and validate the results of the PIC simulations.

An effective method for the verification of the simulations is benchmarking. Benchmarking requires comparing the results produced by different codes. The codes can be different implementations of one numerical algorithm, or they can be based on different numerical algorithms. Benchmarking is more effective if it includes diverse codes with diverse numerical algorithms or implementations. An alternative to the PIC method is the continuum Vlasov method, which is believed to introduce less numerical noise in the simulations. As an important outcome of this thesis, we have developed a semi-Lagrangian Vlasov code. This code was used to produce many results here and for the verification of the results of the PIC simulations through benchmarking. The ECDI Vlasov simulations we present in this thesis are, to the best of our knowledge, the first Vlasov simulations performed on this problem.

Generally, the exact picture of nonlinear processes and anomalous transport often remains elusive. The picture gets even more complicated when one considers the role of the computational artifacts associated with different numerical methods used for simulations. The primary motivation for this thesis is to investigate the nonlinear characteristics of the drift instabilities and the role of the numerical methods in our understanding of these characteristics. Our focus is on two types of drift instabilities, namely, the unmagnetized Buneman-type instabilities and the ECDI.

The outline of the rest of the thesis is as follows. In the rest of Chapter 1, we introduce the concept of plasma and the kinetic and fluid theories of plasma. In Chapter 2, we explain the details of the numerical

methods used in the development of the Semi-Lagrangian Vlasov code. In Chapter 3, we introduce the Buneman instability and show how the numerical noise in the PIC simulations can lead to inaccuracies in the linear regime of this instability. In Chapter 4, the nonlinear regime of the Buneman instability and a phenomenon called the "backward waves" are investigated. The backward waves exist in the nonlinear regime of the Buneman instability and propagate in a direction opposite to the initial relative drift. These waves have a significant effect on transport, and therefore, understanding their behaviors can have important implications in understanding anomalous transport and other related phenomena. In Chapter 5, the ECDI is introduced. In addition, a detailed comparison between the results of the PIC simulation and the Vlasov simulation of the ECDI is done. It is shown that the noise of the PIC simulation can have an important effect on the nonlinear regime of this instability. The effect of the size of the system on the simulations is also studied. In Chapter 6, we present the results of the Vlasov simulation of the ECDI. Many nonlinear characteristics of the ECDI, including transport and heating, are investigated. It is also shown that the transition to ion-sound instability is not likely to happen in the nonlinear regime of ECDI. In Chapter 7, the findings of the thesis are summarized.

1.2 Plasma properties

1.2.1 Important plasma parameters

On large scales, plasma is a quasi-neutral gas. This means that, in contrast to the small scales, on large scales the electron density n_e is approximately equal to the ion density n_i. As a result, any applied electric field will be exponentially damped, with a particular exponent inside a plasma. This exponent is the characteristic range that an external electric field survives inside the plasma and is called Debye length. One can calculate the Debye length in simple conditions as $\lambda_D = \sqrt{\epsilon_0 T_e / n_0 e^2}$ [34], where T_e is the electron temperature, e is the electron charge, ϵ_0 is the permittivity of vacuum, and n_0 is the plasma density which is equal to both the ion and electron density in the quasi-neutral condition. The Debye length is one of the smallest length scales of interest in plasma.

Because of the quasi-neutrality, when some electrons of a plasma in the steady state are slightly displaced by an external force, an electric force is created as a result of the charge separation that tends to oppose the displacement. This results in plasma oscillations. The frequency of these oscillations is the "plasma frequency" ω_{pe}, which is typically one of the largest frequencies in a plasma. For a simple case, it can be shown that the $\omega_{pe} = \sqrt{n_0 e^2 / \epsilon_0 m_e}$, where m_e is the mass of an electron [34]. In the case of warm plasma, these oscillations propagate as a "Langmuir wave" inside the plasma. Similarly, the "ion plasma frequency" as $\omega_{pi} = \sqrt{n_0 e^2 / \epsilon_0 m_i}$ characterize oscillations of ions, where m_i is the mass of ions.

Assuming that the plasma is in equilibrium, i.e., particle velocities obey the Maxwellian distribution, the thermal velocity of each species is defined as the root-mean-square of the velocity of that species; i.e. $v_{ts} = \sqrt{T_s / m_s}$. In magnetized plasma, two important parameters are the cyclotron frequency and the Larmor

radius. The cyclotron frequency is a measure of the frequency of rotation of a charged particle in a magnetic field B_0 and is defined by $\omega_{cs} = q_s B_0/m_s$, where q_s is the charge of species s. The Larmor radius is a measure of the radius of rotation and is defined by $v_\perp/\omega_{cs}$, where $v_\perp$ is the velocity component perpendicular to the magnetic field.

The initial condition of the simulations we have performed in this thesis is Maxwellian. It is because we have assumed that the instabilities start from an equilibrium condition and, in this condition, the distribution of plasma is always Maxwellian. When the velocity subspace has D_v dimensions, the Maxwellian distribution is

$$f_s(\mathbf{x}, \mathbf{v}, 0) = \frac{n_0}{(2\pi v_{ts}^2)^{D_v/2}} \exp\left(-\frac{v^2}{v_{ts}^2}\right), \tag{1.1}$$

where $v_{ts} = \sqrt{T_{s0}/m_s}$ is the thermal velocity, and T_{s0} is the initial temperature of species s. The Maxwellian distribution in plasma is often a result of collisions. The plasmas that we are simulating are essentially collisionless; i.e., the mean free path of particles is much larger than the Debye length. However, the collisions might still exist, and in a long time, they can relax the distribution function to a Maxwellian.

1.2.2 Definition of plasma

The classical plasma can be defined by three conditions [34]

$$\begin{aligned} &\lambda_D \ll L, \\ &\omega_{pe} > \frac{1}{\tau}, \\ &N_D \gg 1, \end{aligned} \tag{1.2}$$

where L is the system length, τ is the meantime of collisions of charged particles and neutral atoms, and $N_D = \frac{4}{3}\pi n \lambda_D^3$ is the number of particles in a sphere with radius λ_D (named the Debye sphere).

In Eq. (1.2), the first criterion ensures that the plasma preserves its quasi-neutral nature. The second criterion is required because the collisions with neutral atoms should not be so frequent that they dominate the plasma interactions. On the contrary, the effect of electromagnetic interactions should always be significant. The third criterion ensures that (within the spatial scales larger than the Debye length) the fluctuations are small. Therefore, the plasma behaves like an ideal gas, and the statistical mechanics of gases remain relevant.

1.3 An introduction to the kinetic and fluid theories of plasma

Inside a plasma, the charged particles can interact with internal and/or external electromagnetic fields. This interaction leads to various complicated phenomena that are described by a set of nonlinear equations. These equations are often kinetic or fluid equations, in addition to the Maxwell equations.

The kinetic model provides the most accurate description of the classical plasmas and is based on Boltz-

mann's equation [35]

$$\frac{\partial f_s}{\partial t} + \mathbf{v}.\nabla f_s + \frac{q_s}{m_s}(\mathbf{E} + \mathbf{v} \times \mathbf{B}).\nabla_{\mathbf{v}} f_s = C(f_s). \tag{1.3}$$

Here, $f_s(\mathbf{x}, \mathbf{v}, t)$ is the distribution function; s is the index of particle species and can refer to ions, electrons, or neutrals, with the charge of q_s and the mass of m_s. In this thesis, we use e as the electron index and i as the ion index. $\mathbf{E}$ is the electric field and $\mathbf{B}$ is the magnetic field. $C(f_s)$ is the collision operator, and depending on the problem setup, it can have different functional forms. In the problems considered in this thesis, the collisions are negligible, and we can assume $C(f_s) = 0$. In such cases, the Boltzmann equation is reduced to the Vlasov equation. Because the phenomena of our interest are mainly happening in collision-less plasmas, the focus of this thesis will be on the Vlasov equation. The Vlasov equation results from the equation of motion of particles and the Klimontovitch equation after averaging out the fast variations in the microscopic fields and the distribution function [36].

The moments of the Boltzmann equation provide the equations of the fluid model. The zeroth moment is resulted from of the integration of Eq. (1.3) [35] and is called the continuity equation

$$\frac{\partial n_s}{\partial t} + \nabla \cdot (n_s \mathbf{V}_s) = S, \tag{1.4}$$

where S is the rate of creation or annihilation of particles due to collisions and ionization, and

$$n_s = \int f_s \mathrm{d}\mathbf{v}, \tag{1.5}$$

$$\mathbf{V}_s = \frac{1}{n_s} \int \mathbf{v} f_s \mathrm{d}\mathbf{v}. \tag{1.6}$$

Here, n_s is called the density and the $\mathbf{V}_s$ is called the average (fluid) velocity of species s.

The first moment results from multiplying the Eq. (1.3) by $\mathbf{v}$ and integrating over the velocity [35] which leads to the momentum balance equation

$$m_s n_s \left(\frac{\partial \mathbf{V}_s}{\partial t} + (\mathbf{v}_s \cdot \nabla)\mathbf{V}_s \right) = q_s n_s (\mathbf{E} + \mathbf{V}_s \times \mathbf{B}) - \nabla p_s - m_s S \mathbf{V}_s + \mathbf{R}_s \tag{1.7}$$

The collision term $\mathbf{R}_s$ is the summation of $\mathbf{R_{ss'}}$ terms, which is the transfer rate of momentum from species s' to s:

$$\mathbf{R}_s = \sum_{s', s' \neq s} \mathbf{R}_{ss'} \tag{1.8}$$

In the many cases, $R_{ss'}$is approximated as a friction force $R_{ss'} = m_s n_s \nu_{ss'} (\mathbf{V}_{s'} - \mathbf{V}_s)$ where $\nu_{ss'}$ is the "collision frequency" of species s' with s. In Eq. (1.7), p is the pressure and is defined by

$$p_s = \frac{1}{3} m_s \int (\mathbf{v} - \mathbf{V}_s)^2 f_s \mathrm{d}\mathbf{v}. \tag{1.9}$$

We note that the temperature T_s is defined by $p_s = n_s T_s$. The second moment of the Boltzmann equation results from multiplying $\frac{1}{2} m_s \mathbf{v}^2$ by Eq. (1.3) and integrating over the velocity [35]. The second moment (that we do not show here for the sake of brevity) is the energy conservation equation. In the fluid model, the moments that are higher than the second or the third are usually neglected. For example, under the

assumption of thermal equilibrium, the second moment reduces to the state equitation of an ideal gas $\frac{\nabla p}{p} = \gamma \frac{\nabla n}{n}$, where γ is the adiabatic index, and the system of equations is closed. Neglecting the higher moments of the Boltzmann equation is called the "closure approximation" and mainly works well in the presence of a large collision frequency, where the shape of the distribution function is close to Maxwellian. In cases where the collisions are rare, the distribution function can significantly deviate from the Maxwellian distribution, and the fluid model does not work well. In such cases, the full kinetic model, as described by Eq. (1.3), should be used. The fluid model is not used in this thesis, and instead, we solve the full Vlasov equation.

The electric field and magnetic field in Eq. (1.3) are found from the Maxwell equations

$$\nabla \times \mathbf{E} = -\frac{\partial \mathbf{B}}{\partial t}, \tag{1.10}$$

$$\nabla \times \mathbf{B} = \mu_0 \epsilon_0 \frac{\partial \mathbf{E}}{\partial t} + \mu_0 \mathbf{J}, \tag{1.11}$$

$$\nabla \cdot \mathbf{E} = \frac{\rho}{\epsilon_0}, \tag{1.12}$$

$$\nabla \cdot \mathbf{B} = 0, \tag{1.13}$$

where μ_0 is the vacuum permeability. The variables ρ and the $\mathbf{J}$ are the charge density and the current density, respectively, and are defined by

$$\rho = \sum_{s=i,e} q_s n_s(\mathbf{x}, t), \tag{1.14}$$

$$\mathbf{J} = \sum_{s=i,e} q_s n_s \mathbf{V}_s, \tag{1.15}$$

where the charge of the electrons $q_e = -e$, and the charge of the ions $q_i = Ze$, where Z is the ionization number. In this thesis, we always take $Z = 1$, which is often the case in low-temperature plasmas.

Eqs. (1.3) and (1.10) to (1.13) make a closed system of equations that is called Vlasov–Maxwell system. In the problems that are considered in this thesis (the Buneman instability and the ECDI), the electrostatic approximation ($\nabla \times \mathbf{E} = 0$) is commonly applied [21]. With this approximation, Eq. (1.3) and Eq. (1.12) (called the Gauss law) make a closed system of equations. Therefore, the other Maxwell equations are not considered. We note that if we define the electrostatic potential (ϕ) by $-\nabla\phi = \mathbf{E}$, the Eq. (1.12) leads to the Poisson equation $\nabla^2\phi = -\rho/\epsilon_0$, and Eqs. (1.3) and (1.12) is called the Vlasov–Poisson system.

1.4 Plasma instabilities

Like other gasses, plasma remains in equilibrium as long as its free energy is minimum, i.e., there is no excess free energy in the system. However, in plasmas, there might exist a particular type of excess energy that drives instability. The type of this excess free energy determines the type of instability. As a result of the instability and in the linear regime, the energy stored in the electric or magnetic fields grows exponentially. An electrostatic drift instability is excited when the kinetic energy of the particles due to their drift ($\frac{1}{2} m_s \mathbf{V}_s^2$) is converted to the electrostatic energy ($\frac{1}{2} \int \epsilon_0 E^2 \mathrm{d}x$). In the drift instabilities considered in this thesis, this

kinetic energy is always a result of the drift velocity of the electrons with respect to the ions. In other words, our problems are defined in the ions' frame of reference.

For exciting the Buneman instability, a beam of electrons is injected inside the equilibrated ions. The electrons in this beam, have a Maxwellian distribution centred around $\mathbf{V}_e$. This means that the electron population carries a drift energy of $\frac{1}{2}m_e\mathbf{V}_s^2$ that is then converted into the electrostatic energy, driving the instability. In the electrostatic approximation, in the Buneman instability, the plasma particles are unaffected by any magnetic field. Therefore, this instability can be studied by the 1-dimensional Vlasov equation (Eq. (3.1)). Although the ECDI is also driven by the drift energy of the electron population, the electron drift velocity has a different origin. In the ECDI, the drift velocity of the electrons is in fact the $E\times B$ drift [34], which is resulted from the applied electric and magnetic fields (see Fig. 2.1 for the configuration of fields). The interaction of the magnetic field with the electron in the ECDI, leads to complicated phenomena that are discussed in the following chapters.

The linear regime of an instability is when the amplitude of fluctuations is small, and the distribution is a Maxwellian function. In the linear regime, a single mode of the electric field is defined by

$$\mathbf{E}(\mathbf{k}) = \mathbf{A}e^{-i\omega(\mathbf{k})t}, \tag{1.16}$$

where $\mathbf{A}$ is an arbitrary constant, $\mathbf{k}$ is the wave vector, and ω is the total frequency that can be a complex function; i.e., $\omega = \omega_R + i\gamma$. Here, $\omega_R(\mathbf{k})$ is the real frequency and $\gamma(\mathbf{k})$ is the linear growth rate. In the next chapters, the term "frequency" refers to the real frequency ω_R. By applying the perturbation methods on the Eq. (1.3) and Eq. (1.12), one can derive an algebraic equation between ω and $\mathbf{k}$ called the "dispersion relation" [37, 38]. The general form of the dispersion relation is

$$G(\omega, \mathbf{k}) = 0, \tag{1.17}$$

where G is a nonlinear function. By solving the dispersion relation, one can calculate the ω_R and γ and study the linear regime analytically. An unstable mode (corresponding to a real and fixed $\mathbf{k}$) has a positive γ that indicates its exponential growth. On the other hand, a damping mode has a negative γ.

The specific dispersion relations of the Buneman instability and the ECDI are shown in the corresponding chapters. For solving the linear dispersion relation of the Buneman instability we used the Matlab `solve` function. For solving the dispersion relation of the ECDI, we use a Python code, developed by Oleksander Chapurin, that works based on the iterative algorithm discussed in Ref. [39]. In this method, Eq. (1.17) is first converted to the form of $F(\omega) = \omega$, for each value of $\mathbf{k}$. Starting from an initial guess of ω, $F(\omega)$ is calculated and substituted back into the F. This process is repeated until the ω remains approximately constant (within the desired error). The final ω is then returned as the solution.

After the linear regime, the instability saturates and the nonlinear regime starts. The saturation is a nonlinear process that can barely be explained by analytical means. Numerical simulations are usually used to study the saturation and the nonlinear regime of instabilities.

2 Numerical simulations and the semi-Lagrangian Vlasov code

While the fluid equations are in three-dimensional spatial space, Eq. (1.3) is an equation in the six-dimensional phase space (consisting of 3 spatial axes and 3 velocity axes). A large number of dimensions means a large volume of space that needs to be resolved in the simulations and provides the main challenge in the numerical modelling of the Vlasov equation. Another challenge is that the Vlasov equation is, by definition, free of any damping mechanism and, therefore, susceptible to numerical instabilities [40].

The particle-in-cell (PIC) and the continuum Vlasov are the main methods for integrating the Vlasov equation. In the PIC method, the phase space volume is resolved using many markers (called macroparticles), while in the Vlasov method, a high-dimensional phase space grid is used to resolve the phase space. The PIC method is more popular than the grid-based Vlasov method because it is less demanding on computer resources. In the past, the PIC method has been successful in demonstrating and predicting many physical characteristics of plasma behavior in various conditions [41]. Its well-known problem is, however, the high level of statistical noise that it introduces in the simulations due to the limited number of macroparticles that can be used for sampling the phase space. This noise, which also exists in the Monte-Carlo simulations [42], scales as $1/\sqrt{N_{ppc}}$, where N_{ppc} is the number of macroparticles. The Vlasov simulations, on the other hand, do not use macroparticles and are free of statistical noise.

In this thesis, we compare the accuracy and efficiency of the PIC and Vlasov simulations in chosen problems. We show that the noise of the PIC simulations can interfere with the physics of our simulations. In the study of the Buneman-type instability, we show that the noise of the PIC simulations can lead to deviation of the simulated linear growth rates from the theory. In another problem of the electron cyclotron drift instability (ECDI), we show that the noise of the PIC simulations compromises the results in both linear and nonlinear regimes of the simulations. These problems are largely mitigated in the Vlasov simulations. In theory, the noise of the PIC simulations can be reduced by increasing the number of macroparticles. However, the computational resources usually limit the number of macroparticles that can be used in practice. Therefore, the grid-based Vlasov method is a more feasible approach to high-accuracy simulations.

The problems that we consider are the Buneman instability in unmagnetized plasma and the electron cyclotron drift instability in magnetized plasma. In both problems, the Vlasov equation and the Gauss law are solved self-consistently using the semi-Lagrangian Vlasov code that we have developed. Both problems have one spatial dimension for the wave propagation; i.e., we are assuming that the plasma inhomogeneity

along other directions is not significant. In the simulations of the Buneman instability, the absence of a magnetic field and external electric field means that many components of the coefficient of $\boldsymbol{\nabla}_{\mathbf{v}} f_s$ in Eq. (1.3) vanish. In this case, only the velocity component along with the spatial direction remains in the Vlasov equation, and therefore, these simulations are called 1D1V (1 spatial direction and 1 velocity direction are considered in the Vlasov equation). In the simulations of the ECDI, however, another velocity component perpendicular to the magnetic field remains in the Vlasov equation. Therefore, these simulations are called 1D2V (1 spatial direction and 2 velocity directions are considered in the Vlasov equation). We note that the kinetic simulation in the full 3D3V phase space is a challenging problem even for the most powerful supercomputers available today. Using the recent advances in the field of high-performance computing, some three-dimensional simulations have been performed [43, 44, 45]. However, the validation and applications of these simulations remain challenging [46].

One issue with the semi-Lagrangian simulations is the negativity of the distribution function. This negativity is usually considered a result of the numerical oscillations that might over-shoot to negative values. In the literature, there are some approaches for positivity-preserving of the distribution function, each of which with its own advantages and disadvantages [47]. In our simulations, quite a few negative values (with an absolute value close to zero) are occasionally observed in the distribution function. Because of their minor number and their close-to-zero values, we decided not to treat them in a particular way, but flooring them to zero.

2.1 The semi-Lagrangian Vlasov code

An important outcome of this thesis is the development of a grid-based Vlasov code capable of solving the Vlasov equation and the Gauss law in the ECDI configuration. This code uses the semi-Lagrangian method introduced in Refs. [48, 49] and is used in many other studies [50]. The semi-Lagrangian method is among the most popular numerical schemes because its time step is not restricted by the CFL condition. Although this method solves the Vlasov equation on an Eulerian phase space grid, it still relies on the equation of motion of particles (characteristic equations). Because of the relevance of particle trajectories to the numerical scheme, it is called "semi-Lagrangian". Some details of the semi-Lagrangian method and the advantages of the splitting scheme inherent in it are discussed in Ref. [51]. The implementation of this code is done in FORTRAN 90. This code was developed with the great help of Dr. Magdi Shoucri. Dr. Shoucri provided the basic subroutines, such as the interpolation subroutines, and initialization subroutine, in FORTRAN 70. The contribution of the author of this thesis was the development of the code in FORTRAN 90, writing the electric field solver, cleaning, reshaping some components, debugging the code, testing with simple problems, the parallelization of the code, applying the method of time-varying boundaries, writing a user interface, and running the code on the high-performance computing machines.

2.1.1 The semi-Lagrangian method applied to the ECDI problem

The configuration of fields in the ECDI problem can be seen in Fig. 2.1. In this figure, E_0 is the external electric field, B_0 is the external magnetic field, and E_x is the self-consistent electric field that is found from the Poisson equation. With this configuration, Eq. (1.3) reads

$$\frac{\partial f_s}{\partial t} + v_x \frac{\partial f_s}{\partial x} + \frac{q_s}{m_s}(E_x - B_0 v_z)\frac{\partial f_s}{\partial v_x} + \frac{q_s}{m_s}(E_0 + B_0 v_x)\frac{\partial f_s}{\partial v_z} = 0. \tag{2.1}$$

Here $s = \{i, e\}$, where i is the ion index and e is the electron index. The charge q_s is $-e$ for the electrons and e for the ions. The ions used in plasma propulsion are usually heavy noble gases and in particular, argon and xenon. In the simulation of the ECDI, we use xenon with a mass of 131.293 u. A common practice in the studies of ECDI is the assumption of unmagnetized ions. The reasons behind this assumption are that the Larmor radius of the ions is much greater than the considered size of the system, and the time for their gyration is much greater than the time of our simulations. Therefore, in the Vlasov equation for the ions, we take $B_0 = 0$. In the absence of the magnetic field, we also usually take $E_0 = 0$ for the ions to prevent their acceleration in the z direction.

Inside the code, we use the normalized (dimensionless) quantities. We normalize the length to the Debye length l_d, the mass to the ion mass m_i, and the time to $1/\omega_{pi}$, where ω_{pi} is the ion plasma frequency. Therefore, the velocities are normalized to the ion sound velocity $c_s = \sqrt{T_{e0}/m_i}$ (T_{e0} is the initial electron temperature), the electric field is normalized to $m_i\omega_{pi}c_s/e$, the magnetic field is normalized to $m_i\omega_{pi}/e$, the energy is normalized to T_{e0}, and the frequencies are normalized to ω_{pi}. With these normalizations, the complete set of equations becomes

$$\frac{\partial f_i}{\partial t} + v_{xi}\frac{\partial f_i}{\partial x} + (E_x - v_{zi}\omega_{ci})\frac{\partial f_i}{\partial v_{xi}} + (E_0 + v_{xi}\omega_{ci})\frac{\partial f_i}{\partial v_{zi}} = 0, \tag{2.2}$$

$$\frac{\partial f_e}{\partial t} + v_{xe}\frac{\partial f_e}{\partial x} - \frac{1}{m_e}(E_x - v_{ze}\omega_{ci})\frac{\partial f_e}{\partial v_{xe}} - \frac{1}{m_e}(E_0 + v_{xe}\omega_{ci})\frac{\partial f_e}{\partial v_{ze}} = 0, \tag{2.3}$$

$$\frac{\partial E_x}{\partial x} = \int f_i \,\mathrm{d}v_{xi}\,\mathrm{d}v_{zi} - \int f_e \,\mathrm{d}v_{xe}\,\mathrm{d}v_{ze} \equiv n_i(x,t) - n_e(x,t) = \rho(x,t), \tag{2.4}$$

where the ω_{ci} is the ion cyclotron frequency and ρ is the charge density. We note that all quantities in Eqs. (2.2) to (2.4) are normalized. For the rest of this chapter, we only work with the normalized quantities.

Eqs. (2.2) and (2.3) are solved using the Strang second order splitting scheme [52]. Eq. (2.3) is split to three advection equations in the x, v_{xe}, and v_{ze} directions:

$$\frac{\partial f_e}{\partial t} + v_{xe}\frac{\partial f_e}{\partial x} = 0, \tag{2.5}$$

$$\frac{\partial f_e}{\partial t} - \frac{1}{m_e}(E_0 + v_{xe}\omega_{ci})\frac{\partial f_e}{\partial v_{ze}} = 0, \tag{2.6}$$

$$\frac{\partial f_e}{\partial t} - \frac{1}{m_e}(E_x - v_{ze}\omega_{ci})\frac{\partial f_e}{\partial v_{xe}} = 0. \tag{2.7}$$

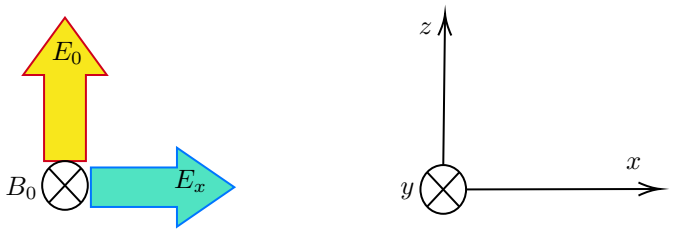

Figure 2.1: The configuration of fields in the ECDI problem.

In the same way Eq. (2.2) is also split into three equations:

$$\frac{\partial f_i}{\partial t} + v_{xi}\frac{\partial f_i}{\partial x} = 0, \tag{2.8}$$

$$\frac{\partial f_i}{\partial t} + (E_0 + v_{xi}\omega_{ci})\frac{\partial f_i}{\partial v_{zi}} = 0, \tag{2.9}$$

$$\frac{\partial f_i}{\partial t} + (E_x - v_{zi}\omega_{ci})\frac{\partial f_i}{\partial v_{xi}} = 0. \tag{2.10}$$

After the first integration of Eqs. (2.5) and (2.8), in the sequence, Eq. (2.4) is solved for finding the E_x and using it in Eq. (2.7). Therefore, a complete scheme for integrating Eqs. (2.2) to (2.4) in one time step (between time t to $t + \Delta t$) is

Step 1 Integrate Eq. (2.8) from t to $t + \Delta t/2$.

Step 2 Integrate Eq. (2.5) from t to $t + \Delta t/2$.

Step 3 Integrate Eq. (2.4).

Step 4 Integrate Eq. (2.6) from t to $t + \Delta t/2$.

Step 5 Integrate Eq. (2.7) from t to $t + \Delta t$, using the E_x calculated at step 3.

Step 6 Integrate Eq. (2.6) from $t + \Delta t/2$ to $t + \Delta t$.

Step 7 Integrate Eq. (2.5) from $t + \Delta t/2$ to $t + \Delta t$.

Step 8 Integrate Eq. (2.9) from t to $t + \Delta t/2$.

Step 9 Integrate Eq. (2.10) from t to $t + \Delta t$, using the E_x calculated at step 3.

Step 10 Integrate Eq. (2.9) from $t + \Delta t/2$ to $t + \Delta t$.

Step 11 Integrate Eq. (2.8) from $t + \Delta t/2$ to $t + \Delta t$.

We note that, in each step, the latest update of f_s is used as the initial condition. Inside the code, there is an option for turning off the effect of E_0 and/or B_0. In case both of these fields have no effect, Eqs. (2.6) and (2.9) is trivial, and therefore, steps 8 and 10 are skipped. Another capability of the code is to use a

larger time step for the ions than the electrons (electron sub-cycling). If the ratio of the ion time step to the electron time step is n_{cyc}, then steps 2 to 7 are repeated n_{cyc} times before moving to step 8. Because the ions' mass is much larger than the electrons, the electron sub-cycling can be used to reduce the computation cost. However, we do not use this capability of the semi-Lagrangian Vlasov code in the simulations presented in this thesis.

2.1.2 The method of characteristics for numerical integration of the advection equations

Eqs. (2.5) to (2.10) are integrated using the method of characteristics [53]. The exact solution of Eqs. (2.5) and (2.8) between t_0 to $t_0 + \Delta t$ is

$$f_s(x, v_{xs}, v_{zs}, t_0 + \Delta t) = f_s(x - v_{xs}\Delta t, v_{xs}, v_{zs}, t_0). \tag{2.11}$$

In the same way, the exact solution of the Eqs. (2.6) and (2.9) is

$$f_s(x, v_{xs}, v_{zs}, t_0 + \Delta t) = f_s\big(x, v_{xs}, v_{zs} - \Delta t(E_0 + v_{xs}\omega_{ci})/m_s, t_0\big), \tag{2.12}$$

and the exact solution of Eqs. (2.7) and (2.10) is

$$f_s(x, v_{xs}, v_{zs}, t_0 + \Delta t) = f_s\big(x, v_{xs} - \Delta t(E_x - v_{zs}\omega_{ci})/m_s, v_{zs}, t_0\big). \tag{2.13}$$

Note that the normalized m_s is 1 for the ions. The right-hand sides (RHS) of each of the Eqs. (2.11) to (2.13) is a shift in its corresponding direction in phase space. Because the results of the shifts might be points in between the grid points, interpolation is used to calculate them. Several interpolation schemes are proposed in the literature (see Ref. [54] for a review of many interpolation schemes). In our code, we use the cubic spline interpolation [55], which is one of the most successful interpolation schemes used in the semi-Lagrangian codes [54]. The details of the cubic spline implementation are discussed in Ref. [56]. The boundary condition is periodic in the spatial subspace and open in the velocity subspace. The algorithm of the cubic spline interpolation scheme depends on the boundary conditions. Therefore, two different subroutines are used for the interpolation in the position and the velocity subspaces.

2.1.3 Solving the Gauss law using the fast Fourier transform

Eq. (2.4) is solved using its Fourier transform on a periodic domain with length L

$$E(k) = \frac{-i\rho(k)}{k}, \tag{2.14}$$

where $E(k)$ is the Fourier transform of the electric field and $\rho(k)$ is the Fourier transform of the charge density. k is the magnitude of the wave vector and can take the values in the form of $k = 2\pi m/L$, where $m = 0, 1, 2, \ldots$, is the mode number. In the code, the Fourier transforms are approximated by the discrete Fourier transform (DFT), which is calculated using the fast Fourier transform (FFT). The Intel Math Kernel

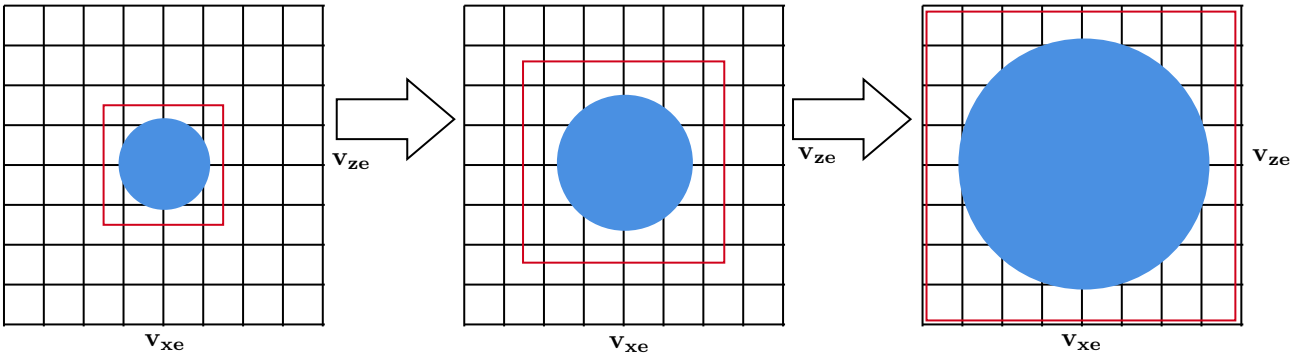

Figure 2.2: A schematic figure of the time-dependent boundaries of the electron velocity subspace. The red squares represent the time-dependent boundaries, and the blue circles represent the area occupied by electrons. The simulation advances from left to right while the electrons heat up.

Library [57] is used to calculate the FFT. After finding $E(k)$ from Eq. (2.14), the inverse FFT is used to calculate $E(x)$.

2.1.4 Performance considerations and parallelization of the code

The code solves the Vlasov equation and the Gauss law on a three-dimensional grid. For the ECDI problem, two high-resolution grids (one grid for electrons with typically $O(10^9)$ points and another grid for ions with typically $O(10^8)$ points) are used, making the computations intensive. To reduce the computation time, we use two methods: time-dependent grid boundaries and parallelization. In combination, these methods can help reduce the computation time by more than one order of magnitude.

The method of time-dependent boundaries uses the fact that in the ECDI simulations (and many other simulations of plasma instabilities), the particle temperature significantly rises, especially late in the simulations. Therefore, we can start with a small grid in the velocity subspace, which gets larger as the simulation time passes. Fig. 2.2 shows a schematic figure of the time-dependent boundaries of the velocity subspace. During the early times of the instability, the temperature is low, and the particles are predominantly concentrated in a small area in the center of the velocity subspace. Therefore, a relatively small grid with a few points can encapsulate all the particle velocities. As time passes, the electron temperature rises, and the area occupied by particle velocities becomes larger, and with it, the time-dependent boundaries will extend.

For a typical 1D ECDI simulation, about 70 percent of the computation time is spent on the interpolations in Eqs. (2.12) and (2.13) on the electrons velocity subspace. Therefore, we only use the time-dependent boundaries in this subspace. The important point in using this method is to tune the pace of extension of boundaries so that the resolved area is the minimum that can encapsulate all the particle velocities. In the code, a subroutine is called from time to time that checks the electron temperature and extends the boundaries accordingly. An adjustable parameter inside the code controls the pace of the extension of the

boundaries. Our investigations show that using this method alone can make the simulations run several times faster, without compromising the accuracy in a significant way.

The parallelization of the code is done using the shared-memory method and OpenMP tools [58]. This method is described in Ref. [59]. This method uses the fact that each of the shifts in Eqs. (2.5) to (2.10) happens only in one dimension in the phase space. Therefore, the other dimensions can be divided into several independent chunks, each of which is passed to a computation thread for doing interpolations. For example, in Eq. (2.5), the only variable along which the interpolations are done in Eq. (2.11) is x. Therefore, v_{xe} and v_{ze} are constants in this equation, and the whole phase space grid can be split into many chunks along v_{xe} and v_{ze}, where the interpolation can be done independently in each chunk. In the same way, for solving Eq. (2.7), the grid can be split into many independent chunks along the x and the v_{ze}. This method can be used to calculate all the interpolations in parallel. After integrating each of the Eqs. (2.5) to (2.10), the solutions are passed to the master thread, and if required, the electric field or the diagnostics are calculated on this thread. Finally, we have used a method described in Ref. [43] for decreasing the cache missing in the interpolation loops, which led to about 50 percent speedup.

3 The role of noise in PIC and Vlasov simulations of the Buneman instability

3.1 Preface

The Buneman instability is an instability caused by the relative drift of electron and ion components in plasma, i.e., by plasma current. Such instability produces high-energy fluctuations, anomalous transport, and heating in unmagnetized plasmas and is relevant to many experimental plasma conditions in space and laboratories. The high-energy fluctuation can lead to many complicated phenomena, which are mainly studied through numerical simulations. Due to the role of the numerical methods, it is important to understand their signature on the simulation results.

In this chapter, we introduce the Buneman instability and investigate the role of the initial noise in PIC simulations on the linear regime of the instability. Using many simulations with PIC and continuum Vlasov methods, we show how the noise of the PIC simulations can undermine the accuracy of the results in these simulations. We show that the PIC results can be improved by the "quiet start" initialization method. In this method, The initial velocity of macroparticles is chosen in a particular order, so that the resultant velocity distribution function is a noise-free Maxwellian. This is in contrast to the "random start" initialization method, which uses a random number generator to sample the initial velocities from a Maxwellian distribution.

This chapter is based on an article published in the Physics of Plasma journal [60]. The author of this thesis (A. Tavassoli) is the first author of the published article and had the highest contribution among the co-authors of this article. This contribution is as follows.

- Leading the conceptualization, investigation, and formal analysis of the study.
- Managing comments, suggestions, and discussions of the co-authors and reflecting them in the text of the article.
- Organizing, writing, and preparing most of the text of the article throughout the preparation and submission processes.
- Having a dominant role in the development of the "semi-Lagrangian Vlasov" code used in this article.

- Running all the simulations that are referred to as "VL1" in the article and producing the data for making the corresponding figures.
- Post-processing with Python and producing some figures of the article.
- Being the corresponding author of the article. All correspondence with the editorial office during the publication process was done through the corresponding author.
- Reflecting the comments of the reviewers in the text of the article and preparing the text of the reply to reviewers, after discussing them with the co-others.

For clarifying the contribution of co-authors in producing figures, their names are printed in the caption of the figures.

3.2 Abstract

The effects of noise in particle-in-cell (PIC) and Vlasov simulations of the Buneman instability in unmagnetized plasmas are studied. It is found that, in the regime of low drift velocity, the linear stage of the instability in PIC simulations differs significantly from the theoretical predictions, whereas in the Vlasov simulations it does not. A series of highly resolved PIC simulations with increasingly large numbers of macroparticles per cell is performed using a number of different PIC codes. All the simulations predict highly similar growth rates that are several times larger than those calculated from the linear theory. As a result, we find that the true convergence of the PIC simulations in the linear regime is elusive to achieve in practice and can easily be misidentified. The discrepancy between the theoretical and observed growth rates is attributed to the initial noise inherently present in PIC simulations, but not in Vlasov simulations, that causes particle trapping even though the fraction of trapped particles is low. We show analytically that even weak distortions of the electron velocity distribution function (such as flattening due to particle trapping) result in significant modifications of the growth rates. It is also found that the common quiet-start method for PIC simulations leads to more accurate growth rates but only if the maximum growth rate mode is perturbed initially. We demonstrate that the quiet-start method does not completely remedy the noise problem because the simulations generally exhibit inconsistencies with the linear theory.

3.3 Introduction

Kinetic simulations are a powerful tool for studies of the linear and nonlinear behavior of plasmas. The particle-in-cell (PIC) method and the continuum Vlasov method are two widely used simulation approaches. The PIC method, which has been available for several decades, has successfully captured many physical phenomena in various scenarios. The PIC method, however, is also known for relatively large levels of numerical noise introduced by the discretization and the limited number of macroparticles used to resolve

the phase space [61]. The noise in PIC simulations exists during the first time step (initial noise), but it also evolves during simulations, thus affecting the results. An alternative to the PIC method, the continuum Vlasov method, is well known as a method that is free of statistical noise. The availability of high-performance computational resources has led to a steady increase of interest and applications of continuum simulations for many physical phenomena and situations that are poorly amenable to the PIC approach [62, 63].

It is well known that the noise in the PIC simulations may significantly undermine the physical results of the simulations. For example, the PIC simulations of electron temperature gradient modes [64, 65] yielded a level of turbulent heat transport that deviated greatly from results of gyrokinetic Vlasov simulations of Refs. [66, 67, 68]. The origin of this discrepancy is investigated in Ref. [69]. It is shown that the discrete particle noise effects in the PIC simulations of Refs. [64, 65] undermine the dynamics of the instability, strongly modifying the predictions for the heat transport levels [69, 70]. The role of the PIC noise has also been discussed in the study of electrodynamic filamentation instability [71]. It is shown that the noise in PIC simulation affects the mechanism of the instability and results in an incorrect instability threshold. In another study, it is shown that the noise of the PIC simulations can lead to significant artificial heating of plasma in the presence of the Monte Carlo collision operator [72]. In Refs. [73, 74, 70], it is emphasized that the role of the discrete particle noise in PIC simulations has to be carefully analyzed and evaluated for each physical situation. For this purpose, several approaches have been proposed in the literature [75, 70, 76, 77, 78]. One approach is to benchmark the physical results with different simulation methods in order to build confidence in simulation results and determine the roots of discrepancies and possible numerical artifacts. Benchmarking has been successfully used as a verification tool for numerical codes in several publications [78, 79, 80]. One feature of benchmarking is that it tests the entire simulation code as opposed to individual units, and it can also be used on the specific problems of interest rather than synthetic test cases [78, 77]. Benchmarking with different numerical methods, such as PIC and Vlasov methods, provides additional confidence in the reliability of the simulations as well as highlighting the causes of possible discrepancies.

In this study, we use several PIC and Vlasov codes to investigate the impact of noise in PIC simulations of the Buneman instability. We show that the linear growth rates of the instability are significantly affected by the noise inherent to the PIC simulations. We identify the trapping of electrons (a nonlinear effect) in the early noise-driven potential as a source of the inconsistencies with the linear theory. This relationship is confirmed by continuum (Vlasov) simulations for the same parameters and initial states (and respectively the same level of noise) as in the corresponding PIC simulations. It is also supported by analytical calculations that show a high sensitivity of the linear growth rates in this problem to small distortions of the Maxwellian velocity distribution function. Therefore, we propose that early trapping of electrons induces a small plateau in the velocity distribution function, leading to the much higher linear growth rates observed in PIC simulations.

The similarities and differences between the PIC and Vlasov simulations are presented through a number of simulations. We begin with PIC simulations of the cold-plasma limit, when $v_0 = 6v_{te}$ is relatively large. In this case, the simulated growth rates are shown to be consistent with the theoretical ones. A set of simulations

is then presented for a relatively low value of the streaming velocity, $v_0 = 2v_{te}$, where $v_{te} = \sqrt{T_e/m_e}$ is the thermal velocity of the electrons, T_e is the initial temperature of the electrons, and m_e is the electron mass. In each simulation, we measure the linear growth rates of several modes and compare them with the results of the linear theory. Some Vlasov simulations are started with an extremely small perturbation that is required by this method to excite the instability. We refer to these simulations as "low-noise" Vlasov simulations (VL1 and VL2 in Table 3.2). The growth rates measured by the low-noise Vlasov simulations are shown to be consistent with the linear theory. On the other hand, some PIC simulations are started with macroparticles randomly distributed in phase space. We refer to these simulations as "random-start" PIC simulations (PIC1, PIC2, PIC3, PIC4, and PIC 5 in Table 3.2). The growth rates measured using random-start PIC simulations deviate significantly (up to a factor of 3) from the linear theory. This discrepancy in linear growth rates persists in the random-start PIC simulations using up to 10^5 macroparticles per cell. In addition, we show that starting a Vlasov simulation with the same level of initial noise as the PIC simulations (VL3 in Table 3.2) leads to a similar discrepancy between the simulated and the theoretical growth rates.

Reflecting its statistical origin, the noise in PIC simulations scales as $1/\sqrt{N_{ppc}}$, where N_{ppc} is the number of macroparticles in each grid cell. The initial noise is a result of the random distribution of the macroparticles in phase space before the first time step. To reduce the adverse effects of the initial noise, a "quiet-start" initialization has been proposed [81, 82]. In contrast to the random-start method, in the quiet-start method, the macroparticles are distributed regularly or semi-regularly with appropriate weights in phase space. Accordingly, the initial noise level is made much smaller. We show that using the quiet-start method does not completely solve the noise problem in PIC simulations. Another outcome of the current study is to show how the quiet-start method should be used to improve the accuracy of the observed linear growth rates in PIC simulations. We first show that although the quiet-start can improve the results by reducing initial noise, the growth of modes is still subject to statistical noise, making an accurate measurement of the linear growth rates difficult. However, initially perturbing the mode with the maximum growth rate helps to achieve better consistency with the linear theory.

The outline of the next sections is as follows. In section 3.4, we review the linear theory of our problem and introduce the general setup for the simulations. In section 3.5, we show some results for a large v_0 ($v_0 = 6v_{te}$) value that show good agreement between the theoretical linear growth rates and the growth rates measured from the theory. In section 3.6, we show various simulations with the PIC and Vlasov methods. As a result, we show how the initial noise of random-start PIC simulations adversely influences with the linear growth and undermines the accuracy of growth rate measurements, a problem that does not appear in the low-noise Vlasov simulations. In section 3.7, we show that a small flattening in the distribution function can increase the observed linear growth rates by several factors. This provides a hypothesis as to the source of the problem in random-start PIC simulations. In section 3.8, we show that, although it does lead to some improvements, the quiet-start method is unlikely to completely solve the problem of the noise in PIC simulation. In section 3.9, we summarize the conclusions of this study.

3.4 The Buneman instability and the problem setup

The Buneman-type instabilities are driven by the relative drift v_0 of electrons with respect to ions in an unmagnetized plasma. The instabilities can be categorized according to the magnitude of v_0 [83]. The Buneman instability regime occurs for $v_0 > v_{te}$. On the other hand, the ion-sound instability occurs for $v_{ti} < v_0 < v_{te}$, where $v_{ti} = \sqrt{T_i/m_i}$, T_i is the initial temperature of the electrons, and m_i is the ion mass. Streaming Buneman-type instabilities are important in many topical problems of plasma physics. For example, they are considered as candidates for explaining the turbulence and anomalous resistivity in solar plasmas [84, 28, 27] and hollow cathode plasmas in Hall thrusters [16] as well as sources of nonlinear effects in ion-beam fusion applications [32].

The Buneman instability has been broadly investigated through numerical simulation [85, 86, 87, 88]. Most of the numerical simulations focus on the nonlinear regimes of the instability, assuming that the linear regime is well understood via analytical dispersion relations. However, the comparison of the linear regime in numerical simulations with the linear theory provides a valuable test for the simulation methods, revealing the validity range of the linear approximation for a particular approach. In this study, we focus on the verification of the linear regime of the Buneman instability in PIC and Vlasov simulations.

The considered equations in the setup of our problem are

$$\frac{\partial f_{i,e}}{\partial t} + v\frac{\partial f_{i,e}}{\partial x} + \frac{qE_x}{m_{i,e}}\frac{\partial f_{i,e}}{\partial v} = 0,$$
$$\frac{\partial E_x}{\partial x} = e(n_i - n_e), \tag{3.1}$$

where $f_{i,e}$ is the distribution function for ions and electrons, respectively, E_x is the electric field, $n_{i,e} = \int f_{i,e}\,\mathrm{d}v$ are the ion and electron densities, and q is the charge, which is $+e$ for the ions and $-e$ for the electrons. The ions are taken to be Hydrogen with mass $m_i = 1$ amu. The initial temperature for both ions and electrons is $T_0 = 0.2$ eV; the initial plasma density is $n_0 = 10^{17}$ m^{-3}. The initial conditions are

$$f_i(x, v, 0) = \frac{n_0}{\sqrt{2\pi}\, v_{ti}} \exp\left(-\frac{v^2}{2v_{ti}^2}\right), \tag{3.2}$$

$$f_e(x, v, 0) = \frac{n_0(1 + \epsilon\cos(k_0 x))}{\sqrt{2\pi}\, v_{te}} \exp\left\{-\frac{(v - v_0)^2}{2v_{te}^2}\right\}. \tag{3.3}$$

The quantities ϵ, and k_0 parameterize a small initial perturbation. In the low-noise Vlasov and quiet-start PIC simulations, these parameters are required to excite the instability. In the low-noise Vlasov simulations, we take $\epsilon = 10^{-5}$, while in the quiet-start PIC simulations we take $\epsilon = 10^{-8}$. In the random-start PIC simulations, there is no need for this perturbation, and we take $\epsilon = 0$. In all the simulations reported, we use periodic boundary conditions in a system of length 6 mm discretized with a grid of 2048 points. This length is large enough to allow excitation of several modes with mode numbers $m \equiv kL/2\pi$. The time step used in the simulations is $\Delta t = 2.39 \times 10^{-4}$ ns. All the time-dependent data are collected at intervals of 500 Δt. The relative drift between ions and electrons (v_0) drives the instability in several modes identified by the linear

dispersion relation

$$1 - \frac{\omega_{pi}^2}{2k^2 v_{ti}^2} Z'\left(\frac{\omega}{\sqrt{2}|k|v_{ti}}\right) - \frac{\omega_{pe}^2}{2k^2 v_{te}^2} Z'\left(\frac{\omega - kv_0}{\sqrt{2}|k|v_{te}}\right) = 0, \tag{3.4}$$

where $\omega \equiv \omega_R + i\gamma$ with γ the linear growth rate, ω_R the frequency, k is the wave vector, ω_{pi} is the ion plasma frequency, ω_{pe} is the electron plasma frequency, and Z is the plasma dispersion function.

3.5 Linear growth rates from PIC simulations for large drift velocity, $v_0 = 6v_{te}$

By choosing the drift velocity of $v_0 = 6v_{te}$, we approach the cold-plasma limit of the Buneman instability. We perform PIC simulations in this limit with 10^4 macroparticles per cell. Fig. 3.1a shows the growth of some select modes. These modes are chosen for the linear growth analysis of the case $v_0 = 6v_{te}$ and include the maximum growth rate mode $m = 16$. We can see a distinct linear growth region in the early evolution of the modes. By fitting a line to this region, we calculate the growth rate of each mode. In Table 3.1, the calculated growth rates are shown to be quite consistent with the results from the linear theory. The standard error (SE) associated with the measurement of the growth rates is also reported in this table. The SEs of the fits are quite small, showing that the growth of the chosen modes is quite linear and not oscillatory. Our other investigations (not reported here) show that even for as few as 10^3 macroparticles per cell, PIC simulations with $v_0 = 6v_{te}$ produce accurate linear growth rates.

The mean of the derivative of the spectral growth over the same time period is an equivalent measure of the growth rate. Variations about the mean provide a measure of the power of the noise present in the growth region. The square of the growth rate over the square of the power of noise was calculated as the signal-to-noise ratio (SNR) of the growth rate [89]. The average SNR of the chosen modes is 21.25 dB, which is much greater than 1. This indicates that the power of noise carried in this case is quite low in the linear growth region. In all the simulations reported in this study, we see that the value of the SNR does not vary much among the chosen modes. Therefore, we only report the SNR averaged over the four chosen modes of each simulation.

3.6 Linear growth rates from Vlasov and random-start PIC simulations for low drift velocity, $v_0 = 2v_{te}$.

In this section, we report on linear growth rates from several PIC and Vlasov simulations for the case of $v_0 = 2v_{te}$. As we show, this regime of relatively low drift velocity can be problematic for the PIC simulations. Therefore, we investigate this regime more extensively by performing several PIC and Vlasov simulations. Due to the large number of these simulations, we assign a specific name to each one in this regime. These simulations are listed and described in Table 3.2.

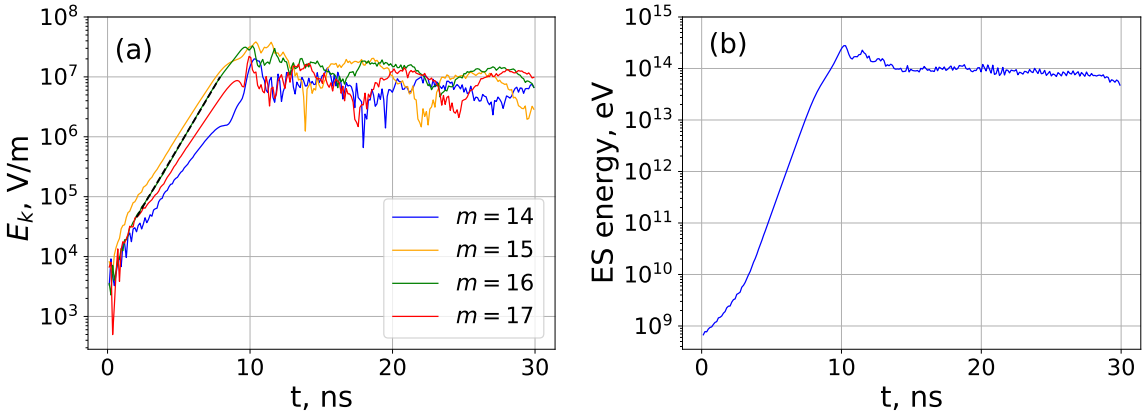

Figure 3.1: a) The evolution of individual modes of the electric field. The dashed black line shows the fitted line on the $m = 16$ mode. b) The evolution of the electrostatic energy. Both figures are from VSim PIC simulations for the case $v_0 = 6v_{te}$. 1 ns =17.84 ω_{pe}^{-1} and ES energy/(6×10^{14})=ES energy per particle [The data used for the production of this figure are produced by Marilyn Jimenez].

m	γ (Theory) $\times 10^8$ s^{-1}	γ (Simulation) $\times 10^8$ s^{-1}	SE (Simulation) %
14	7.08	7.09	1.03
15	8.67	8.60	0.30
16	9.46	9.20	0.24
17	8.13	8.12	0.10
Average	8.34	8.25	0.42

Table 3.1: Comparison of theoretical growth rates with growth rates observed in VSim PIC simulations with $v_0 = 6v_{te}$.

Simulation	Numerical code	Initial condition	macroparticles per cell
VL1	Semi-Lagrangian Vlasov	$m = 1$ perturbed	—
VL2	BOUT++	$m = 1$ perturbed	—
PIC1	EDIPIC	Random start, no perturbation	10^4
PIC2	VSim	Random start, no perturbation	10^4
PIC3	XES1	Random start, no perturbation	10^4
PIC4	EDIPIC	Random start, no perturbation	10^5
PIC5	VSim	Random start, no perturbation	10^5
VL3	Semi-Lagrangian Vlasov	Identical to PIC2	—
PIC6	EDIPIC	Quiet-start, $m = 44$ perturbed	10^4
PIC7	VSim	Quiet-start, $m = 44$ perturbed	10^4
PIC8	XES1	Quiet-start, $m = 44$ perturbed	10^4
PIC9	VSim	Quiet-start, $m = \{31, 37, 44, 51\}$ perturbed	10^4
PIC10	EDIPIC	Quiet-start, no perturbation	10^4
PIC11	EDIPIC	Quiet-start, $m = 1$ perturbed	10^4
PIC12	EDIPIC	Quiet-start, $m = 31$ perturbed	10^4

Table 3.2: The list of simulations with $v_0 = 2v_{te}$.

The first simulation (VL1) is performed by a locally developed semi-Lagrangian code. The semi-Lagrangian Vlasov scheme is a well-known and tested scheme for solving the Vlasov–Poisson equations [48, 90]. In this scheme, the Vlasov equation is split into a convection equation and a force equation. Each of these equations is then solved by the method of characteristics using cubic spline interpolation. The Poisson equation is solved by a spectral method, the FFT. The second Vlasov simulation (VL2) is done with the BOUT++ framework. BOUT++ is a modular platform for 3D simulations of an arbitrary number of fluid equations in curvilinear coordinates using finite-difference methods [91, 92]. Time integration of partial differential equations (PDEs) in BOUT++ is based on the method of lines. The time stepping is performed with the CVODE ODE solver from the SUNDIALS package [93] using variable-order, variable-step multistep methods and is suitable for stiff and nonstiff problems. Spatial derivatives are treated with the third-order weighted essentially non-oscillatory (WENO) scheme for upwind terms and a fourth-order central-difference scheme for other first-order derivatives. In the Vlasov simulations, the velocity boundary conditions are open, and the velocity grid consists of 2001 points. This leads to a velocity resolution of 0.027 c_s and 0.53 c_s for the ions and electrons, respectively, where $c_s = \sqrt{T_0/m_i}$ is the ion sound velocity. We start the low-noise Vlasov simulations (VL1 and VL2) with an extremely small initial perturbation ($\epsilon = 10^{-5}$).

Fig. 3.2 shows the evolution of electrostatic (ES) energy in the low-noise Vlasov simulations (VL1 and VL2), and from here, the linear growth and the nonlinear saturation can be seen. The ES energy in the VL2 simulation starts growing from a larger value than the VL1 simulation. This difference is likely due to the

Poisson solver used in the BOUT++ code that introduces some initial noise that is not present in the semi-Lagrangian code. The ES energy in VL2 simulation, however, damps to a value close to the starting energy in VL1 after about 100 ns. This damping leads to some phase difference between the two simulations so that after 350 ns, the ES energy is higher in the VL2 simulation. The linear growth regimes, which come after about 100 ns in VL1 and 125 ns in VL2, are highly similar in both simulations. For the calculation of linear growth rates, we have chosen four individual modes of the electric field. These modes are $m = \{30, 37, 44, 51\}$ in all simulations (PIC and Vlasov) for the case $v_0 = 2v_{te}$. According to the linear theory, mode $m = 44$ has the maximum linear growth rate in our setup. In Fig. 3.3, the linear growth region is clearly seen for each mode. Table 3.3 shows the values of the linear growth rates calculated from the low-noise Vlasov simulations and the linear theory are quite consistent with each other. The low SEs reported in Table 3.3 reflect the fact that the growth is essentially linear. The average SNR of the chosen modes in the linear growth region are 49.13 dB in the VL1 simulation and 17.75 dB in the VL2 simulation. Because the SNR in both simulations is much greater than unity, we can say the power of noise carried in the growth region is quite small.

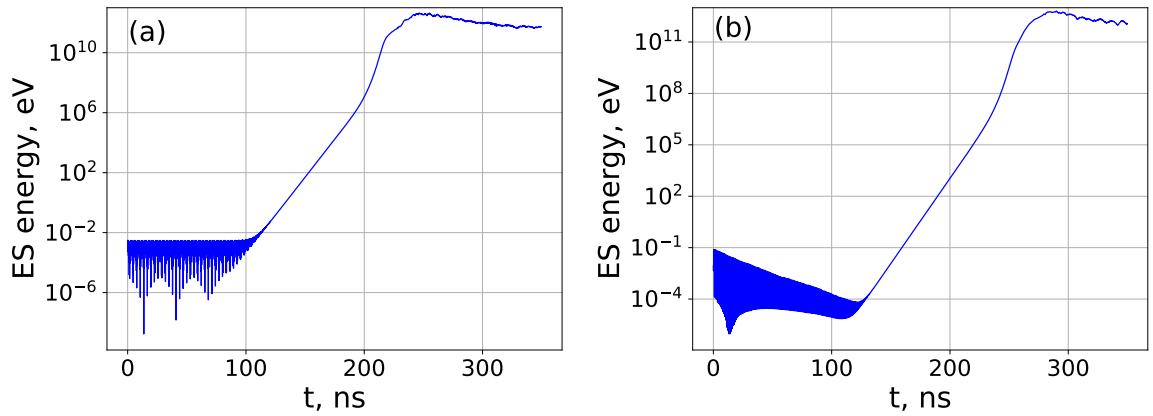

Figure 3.2: The evolution of the electrostatic energy in the low-noise Vlasov simulations (VL1 and VL2). a) Semi-Lagrangian (VL1) and b) BOUT++ (VL2). 1 ns =17.84 ω_{pe}^{-1} and ES energy/(6×10^{14})=ES energy per particle [The data used for the production of (a) and (b) are produced by Arash Tavassoli and Oleksandr Chapurin, respectively].

The PIC simulations are performed with the codes EDIPIC, VSim, and XES1. EDIPIC is a locally developed code that uses the direct-implicit method to integrate the Vlasov–Poisson system of equations in a 1D3V (one spatial dimension and three velocity dimensions) geometry [94]. VSim is a commercial PIC package that uses the VORPAl computation engine [95] to simulate plasmas. In addition, we perform some simulations with XES1 [41]. For the simulations PIC1, PIC2, and PIC3, the calculation of the linear growth rates is done using 10^4 macroparticles per cell. Fig. 3.4 shows the evolution of the electrostatic energy in random-start PIC simulations. At $t = 0$, the electrostatic energy of PIC simulations is very small because at this time the negative and positive charges are distributed uniformly in the system, so that the system is in a quasi-neutral state. This characteristic is embedded in all PIC simulation codes used in this study,

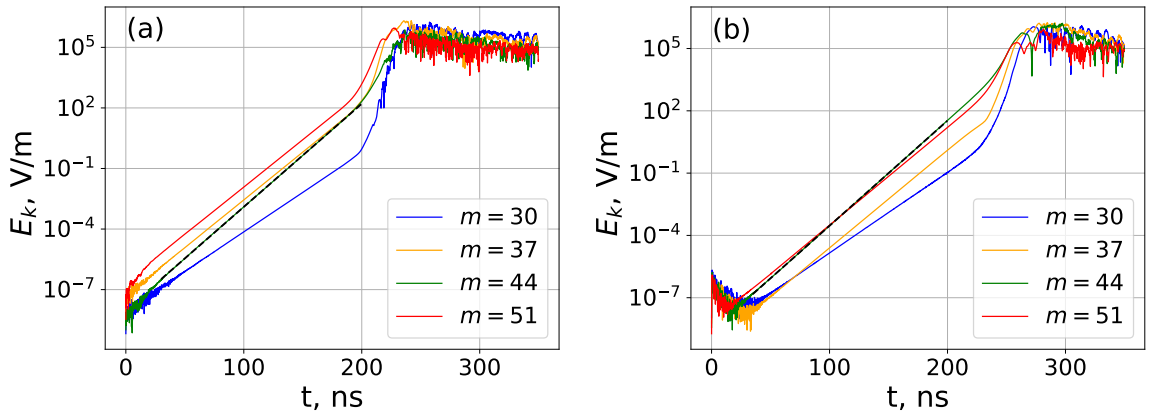

Figure 3.3: a) The evolution of individual modes of the electric field in the low-noise Vlasov simulations (VL1 and VL2). a) semi-Lagrangian (VL1) and b) BOUT++ (VL2). The dashed black line shows the fitted line for the $m = 44$ mode. 1 ns =17.84 ω_{pe}^{-1} [The data used for the production of (a) and (b) are produced by Arash Tavassoli and Oleksandr Chapurin, respectively].

m	γ (Theory) $\times 10^8$ s^{-1}	γ (VL1) $\times 10^8$ s^{-1}	SE (VL1) %	γ (VL2) $\times 10^8$ s^{-1}	SE (VL2) %
30	0.90	0.9	0.029	0.90	0.014
37	1.08	1.09	0.004	1.08	0.006
44	1.17	1.17	0.017	1.16	0.009
51	1.07	1.08	0.004	1.08	0.006
Average	1.06	1.06	0.014	1.06	0.009

Table 3.3: Comparison of the theoretical growth rates with the growth rates observed in the VL1 and VL2 simulations.

independently of their initialization method. However, after $t = 0$, the ES energy jumps to a finite value. This jump, which is absent in the Vlasov simulations, depends on the initial noise in the velocity space of PIC simulations. Therefore, the ES energy at the second collected time ($t = 500\Delta t$) can be seen as a measure of the initial noise in the simulations. Fig. 3.4 shows that, relative to the Vlasov simulations (Fig. 3.2), the ES energy is much larger. This indicates that the amount of initial noise in the PIC simulations is much larger than that of the Vlasov simulations. Fig. 3.5 shows the evolution of the chosen modes separately. The initial growth in these modes is essentially oscillatory instead of being linear, and therefore, the SE of the growth rate measurements is much larger than unity (Table 3.4). We can also define the 99% confidence interval of the measured growth rates as $\gamma(1 \pm 2.576\,\mathrm{SE})$. The theoretical growth rates can be seen to not lie in the 99% confidence interval of the fits, and thus the measured growth rates cannot be seen as equal to the theoretical growth rates to within the measurement error. We note that the applicability of the 99% confidence interval, for this purpose, is limited to the simulations with significant noise in their linear growth regime (i.e., using the confidence interval is not meaningful in simulations where $SE \to 0$ because in such cases the confidence interval nearly vanishes). The average SNR of the chosen modes in the growth region is -8.1 dB in PIC1, -13.75 dB in PIC2, and -15 dB in PIC3. Therefore, the EDIPIC code introduces the least noise power, and XES1 introduces the most noise power in the growth region of the three simulations. We will see that this trend of SNR also applies to the three codes in all other simulations of this study. The small SNR in all three simulations indicates the high noise power in the random-start PIC simulations. To investigate the convergence with respect to the spatial resolution, we repeated the PIC2 simulation with 1024 and 4096 spatial grid points, and the level of noise and the reported results remained close to the original PIC2 simulation. In order to study the effect of only changing the spatial resolution, we note that it is important to not change the number density of macroparticles. The PIC2 simulation was also repeated with a doubled time step size, and again, no significant change was observed in the results.

k	γ (Theory) $\times 10^8$ s^{-1}	γ (PIC1) $\times 10^8$ s^{-1}	SE (PIC1) %	γ (PIC2) $\times 10^8$ s^{-1}	SE (PIC2) %	γ (PIC3) $\times 10^8$ s^{-1}	SE (PIC3) %
30	0.90	2.79	5.80	2.96	1.83	3.37	1.72
37	1.08	3.68	5.30	2.37	3.46	2.02	4.70
44	1.17	3.00	6.00	3.54	1.46	3.44	1.98
51	1.07	4.03	3.00	2.76	4.14	2.38	2.61
Average	1.06	3.38	5.02	2.91	2.72	2.80	2.75

Table 3.4: Comparison of the theoretical growth rates with the growth rates observed in the PIC1, PIC2, and PIC3 simulations.

The inaccurate growth rates of the PIC simulations suggest that the noise level in these simulations is so high that it severely influences the linear growth. Therefore, to reduce the statistical noise level, we increase the number of macroparticles per cell to 10^5 and redo the PIC simulations (PIC4 and PIC5). The initial

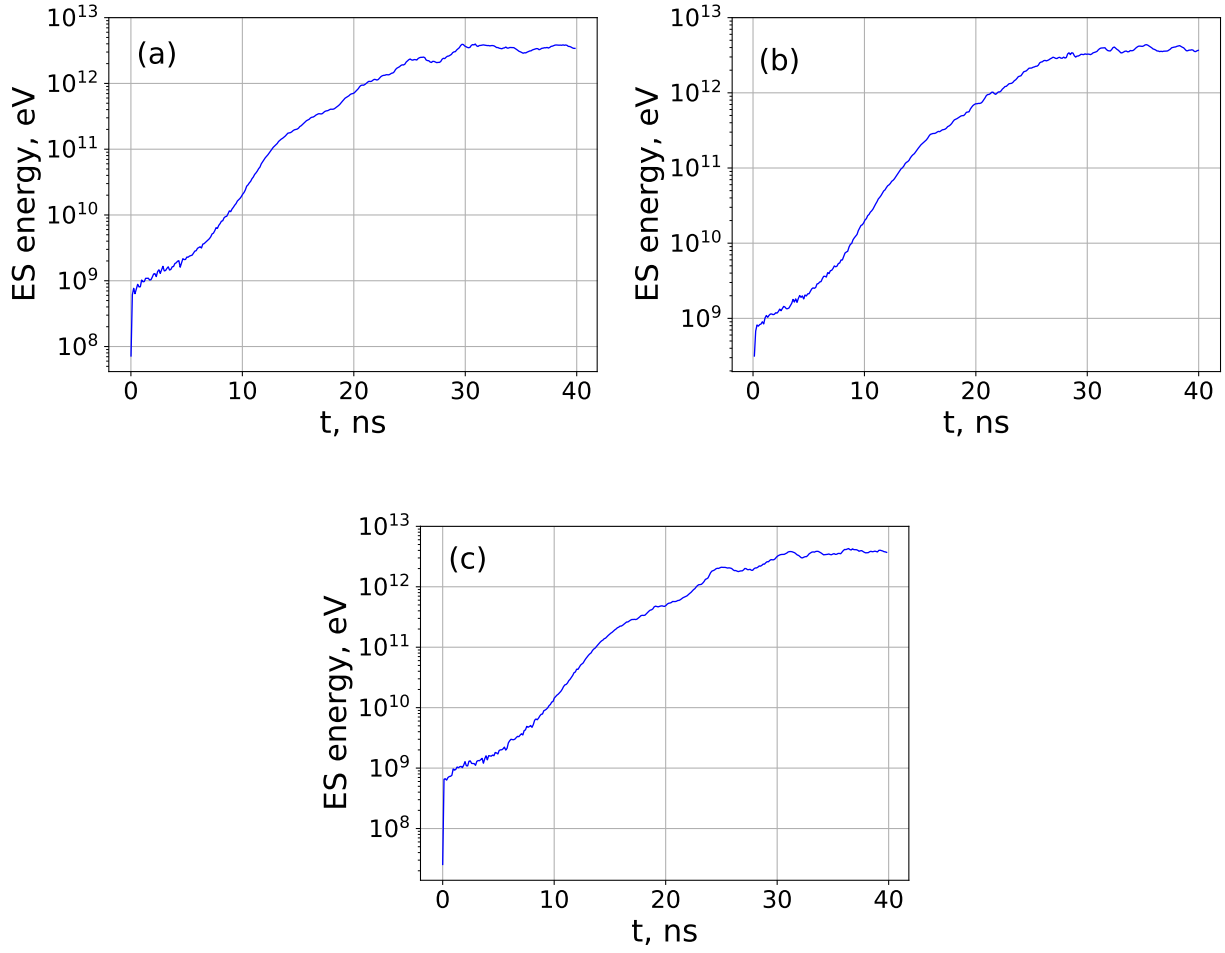

Figure 3.4: The evolution of the electrostatic energy in random-start PIC using 10^4 macroparticles per cell from a) EDIPIC (PIC1) b) VSim (PIC2) c) XES1 (PIC3) simulation . 1 ns =17.84 ω_{pe}^{-1} and ES energy/(6×10^{14})=ES energy per particle [The data used for the production of (a), (b), and (c) are produced by Trevor Zintel, Marilyn Jimenez and Mina Papahn Zadeh, respectively].

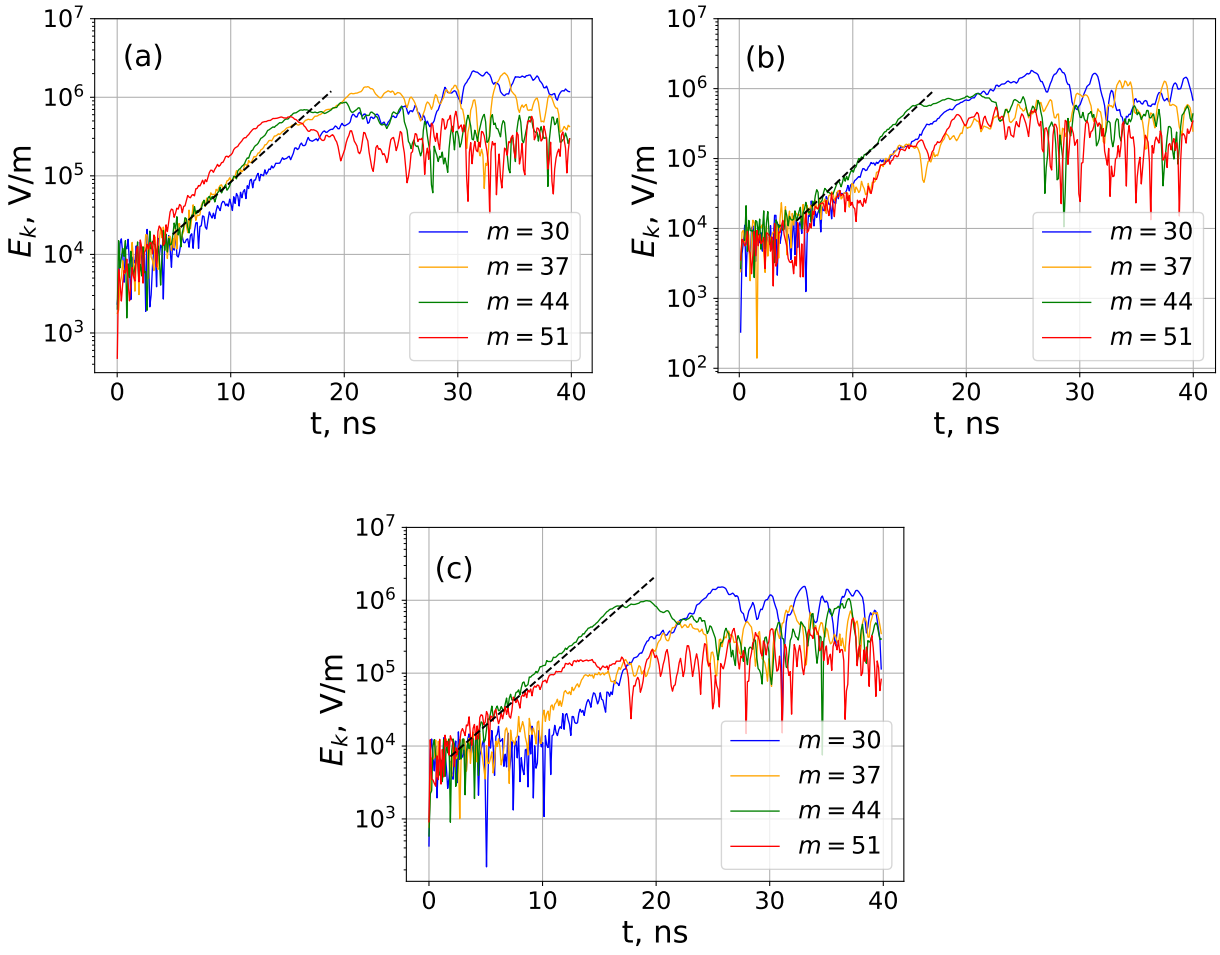

Figure 3.5: The evolution of individual modes of the electric field in random-start PIC simulations using 10^4 macroparticles per cell from a) EDIPIC (PIC1), b) VSim (PIC2), and c) XES1 (PIC3) simulation. The dashed black line shows the fitted line on the $m = 44$ mode. 1 ns =17.84 ω_{pe}^{-1} [The data used for the production of (a), (b), and (c) are produced by Trevor Zintel, Marilyn Jimenez and Mina Papahn Zadeh, respectively].

electrostatic energy in this case is reduced by an approximate factor of 1/10, whereas the initial amplitude of individual modes is reduced by an approximate factor of $1/\sqrt{10}$ (compare Fig. 3.6 and Fig. 3.7 with Fig. 3.4 and Fig. 3.5, respectively). This indicates that the initial noise is reduced approximately by a factor of $1/\sqrt{N_{ppc}}$, as expected. The measured growth rates for the random-start PIC simulations with 10^5 particle per cell are reported in Table 3.5. The growth rates of PIC4 simulation with 10^5 macroparticles per cell are smaller than their counterparts in PIC1 with 10^4 macroparticles per cell. Accordingly, they are closer to the theoretical growth rates. On the other hand, we see a reduction in spurious oscillation in the linear regime, so that the SEs of the PIC4 simulation are less than those of the PIC1 simulation. In Table 3.5, we can also see that the average growth rate in the PIC5 simulation is closer to the theory than its corresponding PIC2 simulation. However, in a few modes, such as $m = 51$, we see that the measured growth rate in PIC5 is farther from the theory than it is in PIC2. In both PIC4 and PIC5, the measured linear growth rates are still much larger than the theoretical growth rates. The average SNR of the chosen modes is −15.58 dB in PIC4 and −14.75 dB in PIC5.

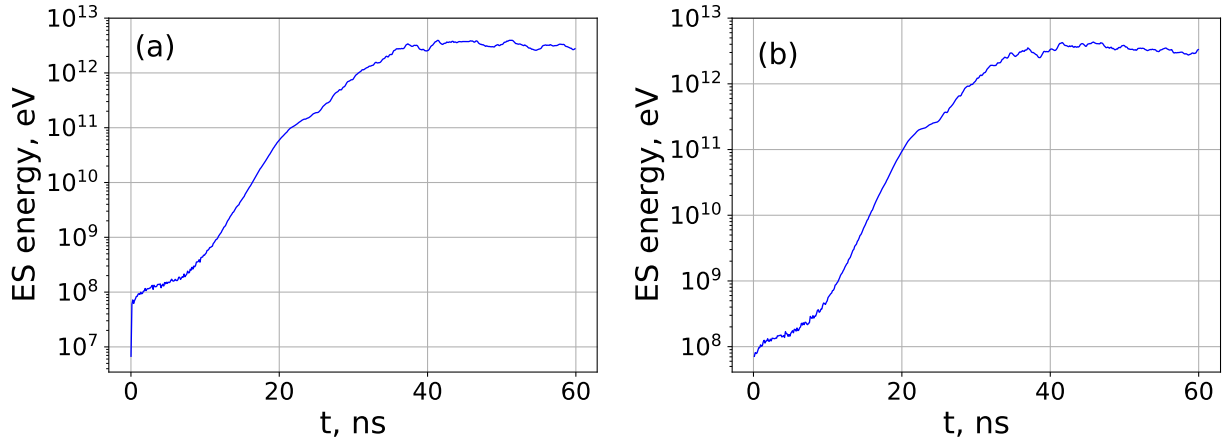

Figure 3.6: The evolution of the electrostatic energy in random-start PIC using 10^5 macroparticles per cell from a) EDIPIC (PIC4) b) VSim (PIC5) simulations . 1 ns =17.84 ω_{pe}^{-1} and ES energy/(6×10^{14})=ES energy per particle [The data used for the production of (a) and (b) are produced by Trevor Zintel and Marilyn Jimenez, respectively].

To investigate the problem of inaccurate growth rates in random-start PIC simulations, we introduce a test simulation with the semi-Lagrangian Vlasov code. In this simulation (VL3), we tabulate the initial condition of macroparticles in PIC2 simulation to find the corresponding distribution function and use it as the initial condition for the semi-Lagrangian Vlasov code. By doing this, we introduce the same initial noise as the PIC simulations into the Vlasov simulation. We then repeat the ES energy and mode growth rate analyses using the results of the VL3 simulation (Figs. 3.8a and 3.8b). As with the PIC simulations, we see that the growth of the chosen modes is oscillatory, and the resultant growth rates are much larger than those predicted from theory (Table 3.6). This strongly suggests that the influence of the initial noise in the PIC

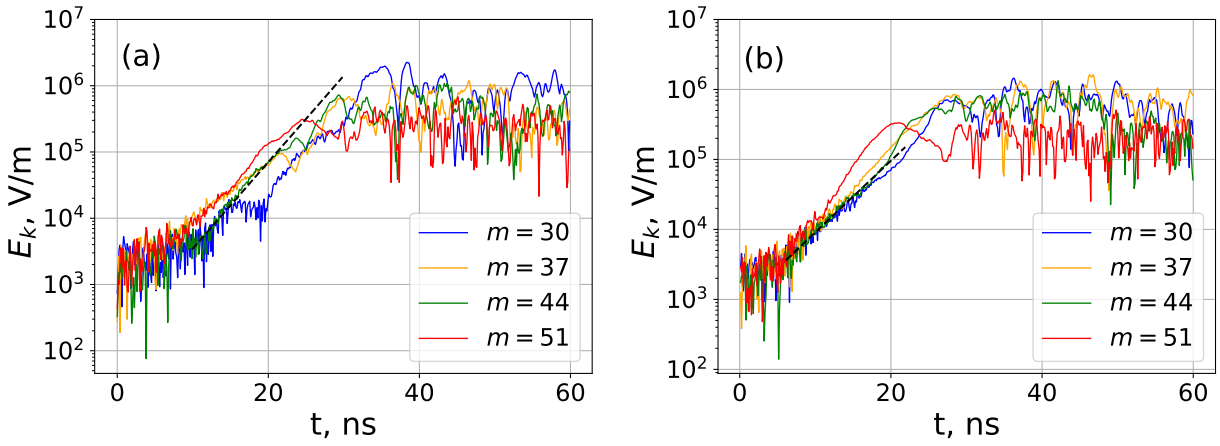

Figure 3.7: The evolution of individual modes of the electric field in random-start PIC simulations using 10^5 macroparticles per cell from a) EDIPIC (PIC4), b) VSim (PIC5) simulations. The dashed black line shows the fitted line on the $m = 44$ mode. 1 ns =17.84 ω_{pe}^{-1} [The data used for the production of (a) and (b) are produced by Trevor Zintel and Marilyn Jimenez, respectively].

m	γ (Theory) $\times 10^8 s^{-1}$	γ (PIC4) $\times 10^8 s^{-1}$	SE (PIC4) %	γ (PIC5) $\times 10^8 s^{-1}$	SE (PIC5) %
30	0.90	2.45	1.60	2.08	2.23
37	1.08	1.81	1.71	2.56	2.01
44	1.17	3.00	1.90	2.55	2.74
51	1.07	2.69	1.11	3.29	1.17
Average	1.06	2.49	1.58	2.62	2.04

Table 3.5: The comparison of the theoretical growth rates with the growth rates observed in the PIC4 and PIC5 simulations.

simulations is the cause of inaccurate growth rates.

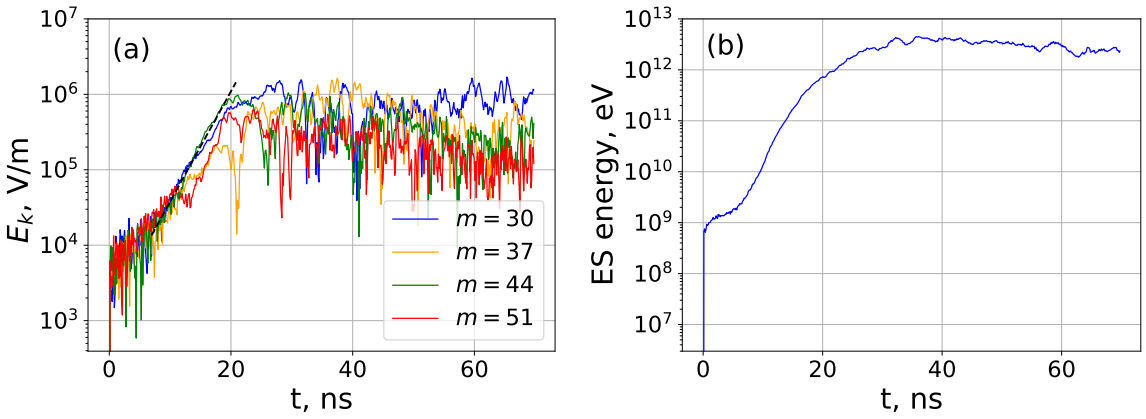

Figure 3.8: a) The evolution of individual modes of the electric field. The dashed black line shows the fitted line on the $m = 44$ mode. b) The evolution of the electrostatic energy. Both figures are from the semi-Lagrangian code (VL3) with the initial condition taken from PIC2 simulation. 1 ns =17.84 ω_{pe}^{-1} and ES energy/(6×10^{14})=ES energy per particle

m	γ (Theory) $\times 10^8$ s^{-1}	γ (VL3) $\times 10^8$ s^{-1}	SE (VL3) %
30	0.90	3.00	1.57
37	1.08	2.30	2.71
44	1.17	3.50	1.23
51	1.07	2.17	2.99
Average	1.06	2.74	2.13

Table 3.6: Comparison of the theoretical growth rates with the growth rates observed in the VL3 simulation.

3.7 The effect of a small flattening of electron distribution function on linear growth rates

In Fig. 3.9, the coherent structures (holes) in the electron velocity distribution function (VDF) are shown. These structures appear early in the PIC3 simulation (similar structures are observed in other PIC simulations with random-start and VL3) and are a result of the trapping of electrons and reflect a small flattening in their Maxwellian velocity distribution function (Fig. 3.10a). This flattening is in fact a depletion of the electrons in the positive velocity region of electron VDF that leads to an increase in electrons in the negative velocity region. To model the flattened velocity distribution function, we add and subtract two shifted Maxwellians

(beams) from the initial electron VDF of Eq. (3.3):

$$f_m(v) = \frac{n_0}{\sqrt{2\pi}v_{te}} \exp\left(-\frac{(v-v_0)^2}{2v_{te}^2}\right) + \frac{\alpha n_0}{\sqrt{2\pi}v'_{te}} \exp\left(-\frac{(v+v'_0)^2}{2v'^2_{te}}\right) - \frac{\alpha n_0}{\sqrt{2\pi}v'_{te}} \exp\left(-\frac{(v-v'_0)^2}{2v'^2_{te}}\right), \tag{3.5}$$

where v'_0 is the drift velocity of the added beams, v'_{te} is their thermal velocity, and α is their density fraction. To replicate the flattened electron VDF in the simulations, we take $\alpha = 0.002$, $v'_{te} = 0.1\, v_{te}$, and $v'_0 = 0.1\, v_0$. Fig. 3.10b shows this VDF and compares it with the Maxwellian VDF ($\alpha = 0$). Using this VDF, the linear desperation relation reads:

$$1 + \frac{1}{k^2\lambda_{Di}^2}\mathrm{Z}'\left(\frac{\omega}{\sqrt{2}kv_{ti}}\right) + \frac{1}{k^2\lambda_{De}^2}\mathrm{Z}'\left(\frac{\omega - kv_0}{\sqrt{2}kv_{te}}\right) + \alpha\frac{1}{k^2\lambda_{De}^2}\mathrm{Z}'\left(\frac{\omega + kv'_0}{\sqrt{2}kv'_{te}}\right) - \alpha\frac{1}{k^2\lambda_{De}^2}\mathrm{Z}'\left(\frac{\omega - kv'_0}{\sqrt{2}kv'_{te}}\right) = 0, \tag{3.6}$$

where $\lambda_{Di,De}$ are the ion and electron Debye lengths.

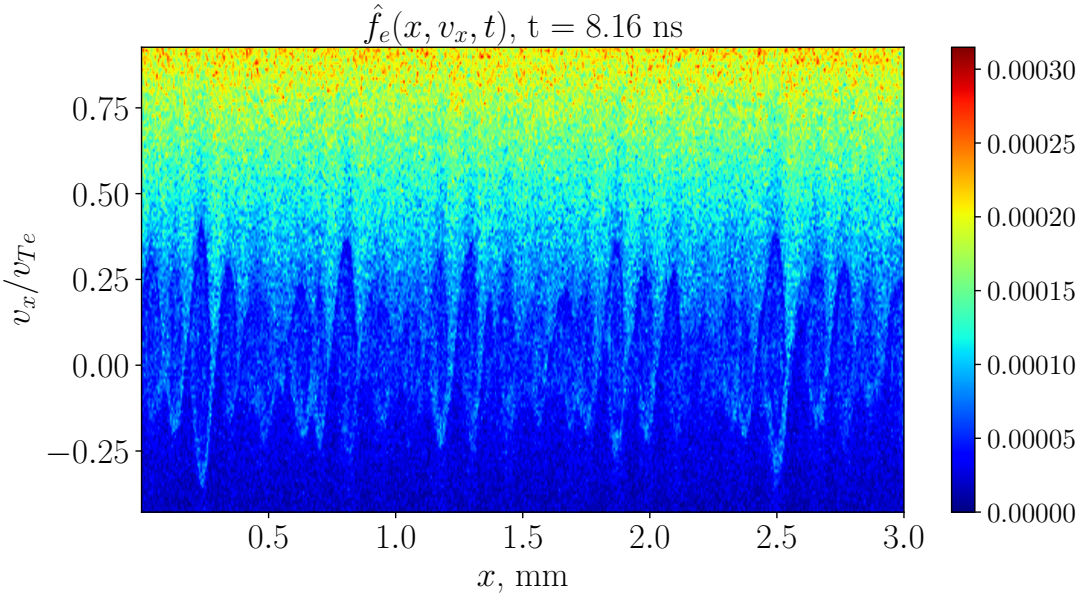

Figure 3.9: The holes in the electron distribution function at $t = 8.16$ ns of simulation PIC3. 1 mm= 95.1 λ_D [The data used for the production of this figure are produced by Oleksandr Chapurin].

Solving this dispersion relation, we find the growth rates as shown in Fig. 3.11. We see that the small flattening in the electron Maxwellian VDF leads to much larger growth rates.

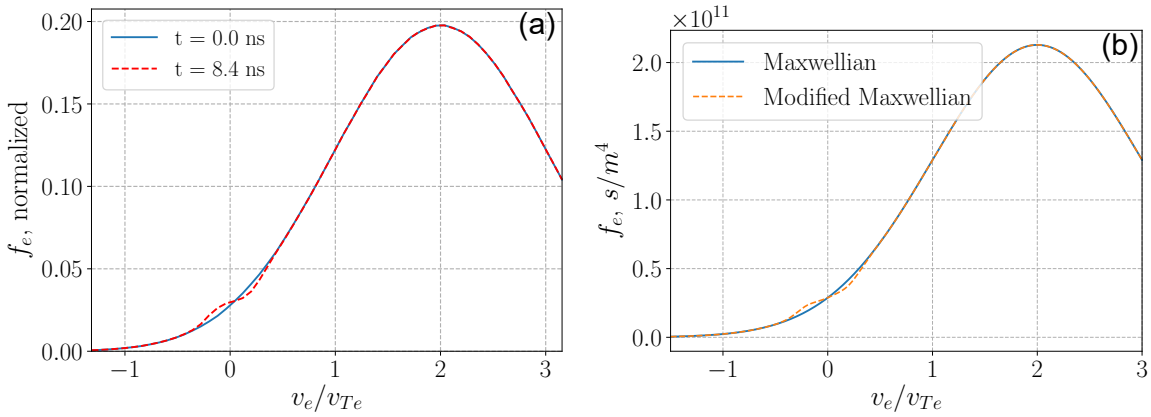

Figure 3.10: a) Electron VDF in PIC3 simulation at $x = L/2$. b) Electron VDF in Section 3.7 for $\alpha = 0.002$, $v'_{te} = 0.1v_{te}$, and $v'_0 = 0.1v_0$. For comparison, the Maxwellian VDF is also shown in blue, in each figure [The data used for the production of this figure are produced by Oleksandr Chapurin].

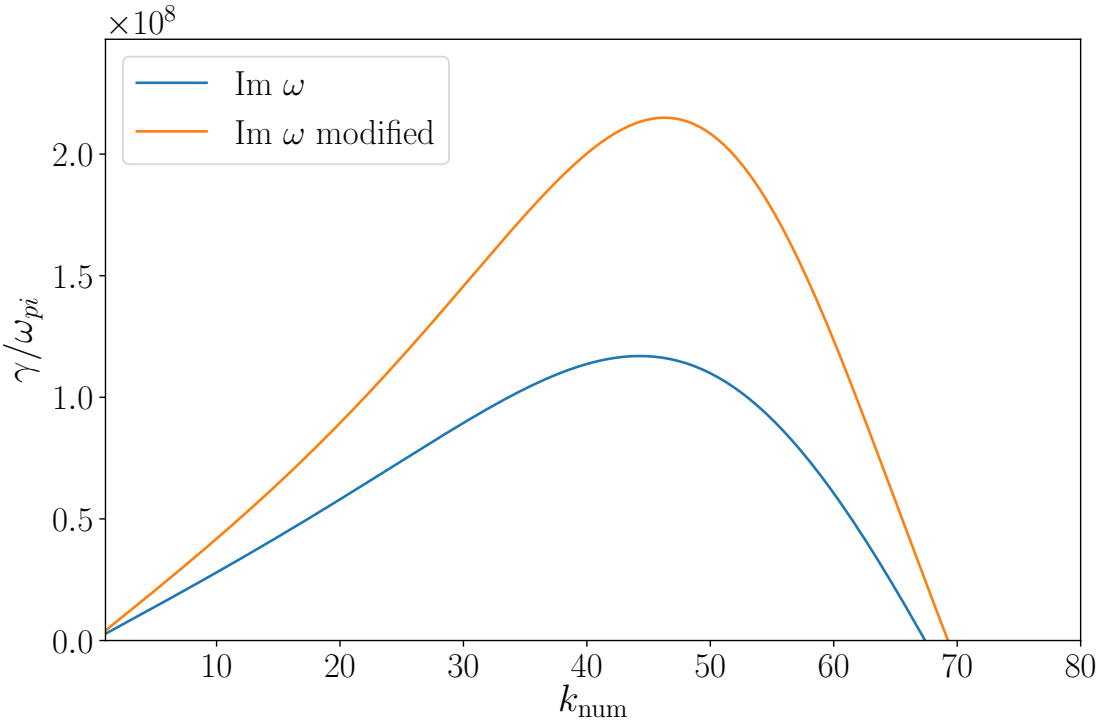

Figure 3.11: Growth rate from the modified dispersion equation (Eq. (3.6)), with $\alpha = 0.002$, $v'_{te} = 0.1v_{te}$, and $v'_0 = 0.1v_0$. For comparison, the growth rates of original dispersion relation are also shown [The data used for the production of this figure are produced by Oleksandr Chapurin].

3.8 Using quiet-start initialization to reduce the effect of noise in PIC simulations

In this section, we report on several PIC simulations (PIC6 to PIC12) that use the quiet-start initialization. The quiet-start initialization, proposed by J. A. Byers [82], employs a smooth loading of macroparticles in phase space to reduce the noise in PIC simulation. In this method, the initial placement of macroparticles in x-v space starts with desired space and velocity densities, $n_0(x)$ and $f_0(v)$, respectively. The method for generating the positions and velocities of each particle from density functions is based on the inversion of the "cumulative density",

$$R_s(\xi) = \frac{\int_a^{\xi} d(\xi')d\xi'}{\int_a^{b} d(\xi')d\xi'}, \tag{3.7}$$

where $d(\xi')$ is the density function and ξ can be either x or v. This cumulative density calculates the cumulative probability in each component x or v. R_s can be a uniform set of numbers or a numerical sequence that generates quasi-random numbers with low discrepancy. Several sequences have been proposed in the literature, including the bit-reversed (or Hammersley) sequence [96, 41, 97], Sobol sequence [98], and Fibonacci sequence [99]. The inversion of the R_s function, by either analytical or numerical means, produces the position or velocity of macroparticles. The R_s set for velocity and position should be uncorrelated to avoid unwanted bunching in phase space. The quiet-start used in our PIC simulations utilizes the bit-reversed set for assigning particle positions and a uniform set of numbers for R_s for particle velocity. This method of quiet-start has been described and implemented in Ref. [41]. In practice, a particular mode is perturbed with a finite amplitude initially.

Fig. 3.12 shows the growth of individual modes in simulations PIC6, PIC7, and PIC8 using the quiet-start initialization. In these simulations, we have only perturbed the maximum growth rate mode $m = 44$ initially. The growth rates measured by these simulations are reported in Table 3.7. An obvious improvement, in comparison with the corresponding random-start PIC simulations (PIC1, PIC2, and PIC3), is that here the growth rate of the perturbed mode $m = 44$ is close to its theoretical value in all three simulations. The average growth rates measured in PIC6 (EDIPIC) and PIC7 (VSim) are also the same as the theoretical growth rates within the 99% confidence interval. However, for the PIC8 simulation (XES1), the theoretical average growth rate is not in the 99% confidence interval of the measured growth rate, and therefore, the two growth rates cannot be considered to be equal by this measure. This discrepancy is due to the inaccuracy of the growth rates for $m = \{30, 37, 51\}$ produced in the PIC8 simulation. In particular, the individual mode $m = 30$ in all three PIC simulations is far from the theoretical value. The average SE in the PIC6 simulation is improved in comparison with its corresponding random-start simulation (PIC1). In contrast, the average SE of the modes is larger in PIC7 and PIC8 than in the corresponding random-start PIC simulations (PIC2 and PIC3, respectively). This indicates that, in general, the linearity of the growth has deteriorated in PIC7 and PIC8 simulations. The average SNR in the growth rate of chosen modes is -26.5 dB in PIC6, -27.5 dB

in PIC7, and −29.75 dB in PIC8. These values of SNR are much smaller than what is reported in section 3.6 for the corresponding random-start PIC simulations. This is likely because of the high-frequency oscillations observed in the growth region of the quiet-start simulations (Fig. 3.12) carry a large power of noise.

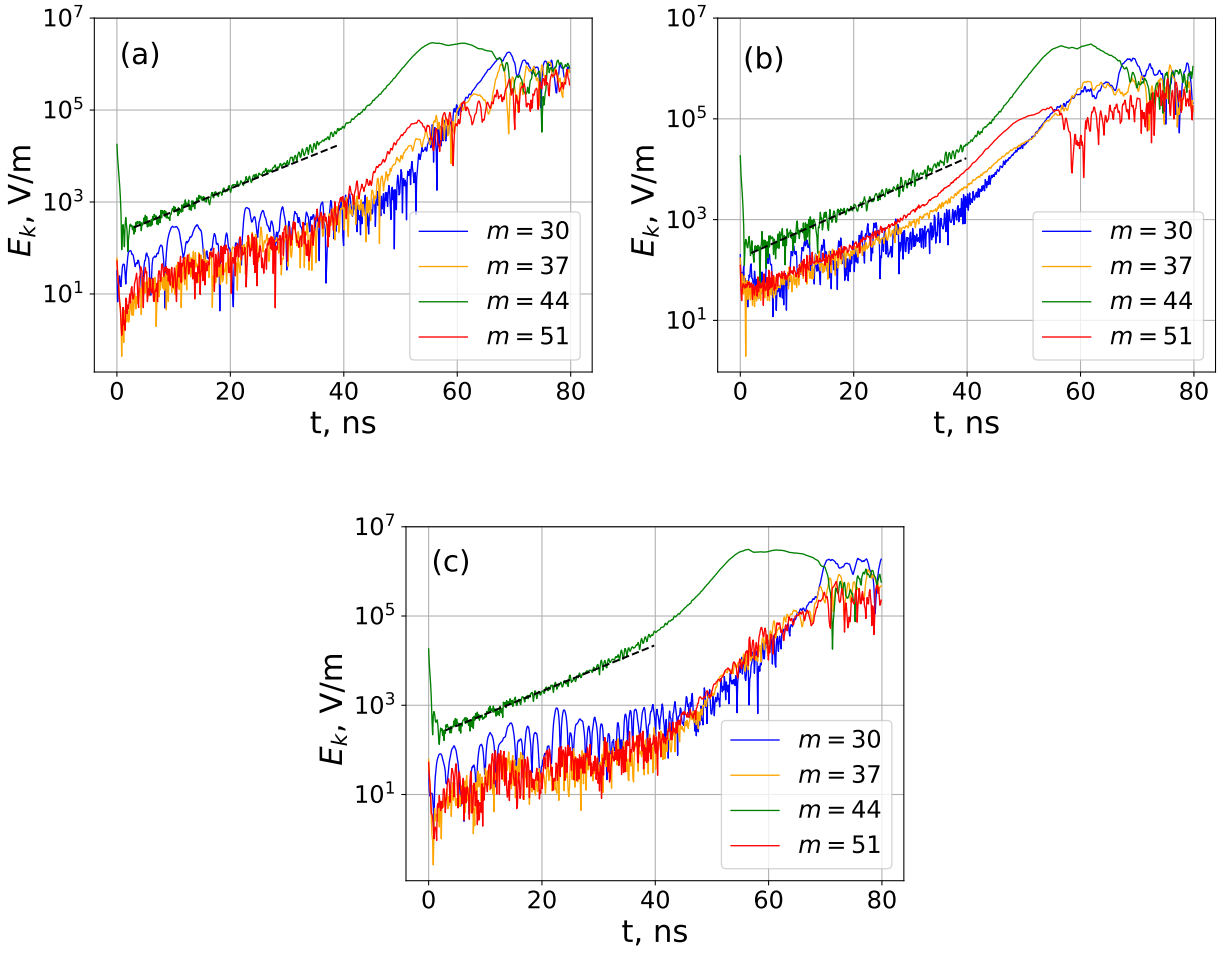

Figure 3.12: The evolution of individual modes of the electric field in quiet-start PIC simulations, using 10^4 macroparticles per cell, from a) EDIPIC (PIC6) b) VSim (PIC7) c) XES1 (PIC8) simulation. The dashed black line shows the fitted line on the $m = 44$ mode. 1 ns =17.84 ω_{pe}^{-1} [The data used for the production of (a), (b), and (c) are produced by Trevor Zintel, Mina Papahn Zadeh and Mina Papahn Zadeh, respectively].

In the PIC9 simulation, we have perturbed the group of the modes $m = \{30, 37, 44, 51\}$. Table 3.8 shows that this method of initialization leads to a much smaller average standard error and indicates an improvement in the linearity of the growth compared to the PIC6, PIC7, and PIC8 simulations (see also Fig. 3.13). This improved linearity, however, leads to a smaller 99% confidence interval, and accordingly, the theoretical average growth rate lies outside the 99% confidence interval of the measurement. Nevertheless, the measured growth rates of the PIC9 simulation are much closer to the theoretical values than those from the corresponding random-start simulation PIC2.

m	γ (Theory) $\times 10^8 s^{-1}$	γ (PIC6) $\times 10^8 s^{-1}$	SE (PIC6) %	γ (PIC7) $\times 10^8 s^{-1}$	SE (PIC7) %	γ (PIC8) $\times 10^8 s^{-1}$	SE (PIC8) %
30	0.90	0.61	5.61	0.77	8.36	0.66	7.28
37	1.08	1.05	2.52	1.14	2.18	0.61	5.91
44	1.17	1.15	2.70	1.17	2.21	1.18	1.15
51	1.07	1.12	2.62	1.23	1.43	0.62	6.21
Average	1.06	0.98	3.36	1.08	3.55	0.77	5.14

Table 3.7: The comparison of the theoretical growth rates with the growth rates observed in PIC6, PIC7, and PIC8 simulations.

m	γ (Theory) $\times 10^8 s^{-1}$	γ (PIC9) $\times 10^8 s^{-1}$	SE (PIC9) %
30	0.90	1.32	3.63
37	1.08	1.18	1.95
44	1.17	1.26	1.23
51	1.07	1.22	1.08
Average	1.06	1.25	1.97

Table 3.8: Comparison of the theoretical growth rates with the growth rates observed in the PIC9 simulation.

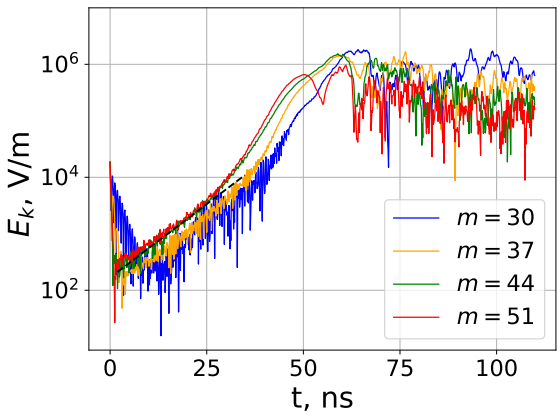

Figure 3.13: The evolution of individual modes of the electric field, from PIC9 simulation. The dashed black line shows the fitted line on the $m = 44$ mode. 1 ns =17.84 ω_{pe}^{-1} [The data used for the production of this figure are produced by Mina Papahn Zadeh].

To further investigate the role of the initial perturbation in the quiet-start simulations, we introduce three more PIC simulations (PIC10, PIC11, and PIC12). In these three simulations, the maximum growth rate $m = 44$ is not perturbed initially. In the PIC10 simulation, we initialize the simulation with quiet-start but without exciting any mode. In this case, we expect the inherent noise of the PIC simulation to excite the instability. In PIC11 and PIC12, the simulations are initialized with perturbations in the modes $m = 1$ and $m = 31$, respectively. Although the individual modes start growing from much lower amplitudes than the random-start PIC simulations, their growth is quite oscillatory at the beginning (see Fig. 3.14). Also, the measured growth rates are mostly far from the theoretical values. However, in contrast to the random-start PIC simulations, most of the growth rates are underestimated by these simulations (see Table 3.9). The average SNR of the growth rate is -34.1 dB in PIC10, -34.3 dB in PIC11, and -30 dB in PIC12. Therefore, the SNRs are lower than the quiet-start simulations PIC6, PIC7, and PIC8, where the maximum growth rate is perturbed initially.

m	γ (Theory) $\times 10^8$ s^{-1}	γ (PIC10) $\times 10^8$ s^{-1}	SE (PIC10) %	γ (PIC11) $\times 10^8$ s^{-1}	SE (PIC11) %	γ (PIC12) $\times 10^8$ s^{-1}	SE (PIC12) %
30	0.90	0.62	4.19	0.62	4.14	1.21	2.59
37	1.08	0.59	6.11	0.61	5.67	1.26	1.52
44	1.17	0.34	7.71	0.40	5.95	0.43	6.73
51	1.07	0.63	4.52	0.65	4.88	0.92	3.13
Average	1.06	0.55	5.63	0.57	5.16	0.96	3.49

Table 3.9: The comparison of the theoretical growth rates with the growth rates observed in PIC10, PIC11, and PIC12 simulations.

3.9 Conclusion

In this study, we investigated the linear regime of the Buneman instability with several PIC and Vlasov simulations. The different PIC codes show good consistency in their results, and two different implementations of Vlasov simulations are also consistent with each other; the results between the PIC and Vlasov simulations, however, differ significantly. We show that for a relatively small streaming velocity, $v_0 = 2v_{te}$, the random-start PIC simulations do not reproduce the theoretical linear growth rates, whereas the low-noise Vlasov simulations reproduce them quite accurately. We show that the reason for the discrepancy is the discrete particle noise inherent to PIC simulations. This is demonstrated by initializing Vlasov simulations with the initial conditions of the random-start PIC simulations, which, in the latter case, show a discrepancy similar to PIC results.

This discrepancy is further confirmed by the study of the growth-rate sensitivity to a small flattening in the electron VDF. In Section 3.7, we show that a small flattening significantly increases the linear growth

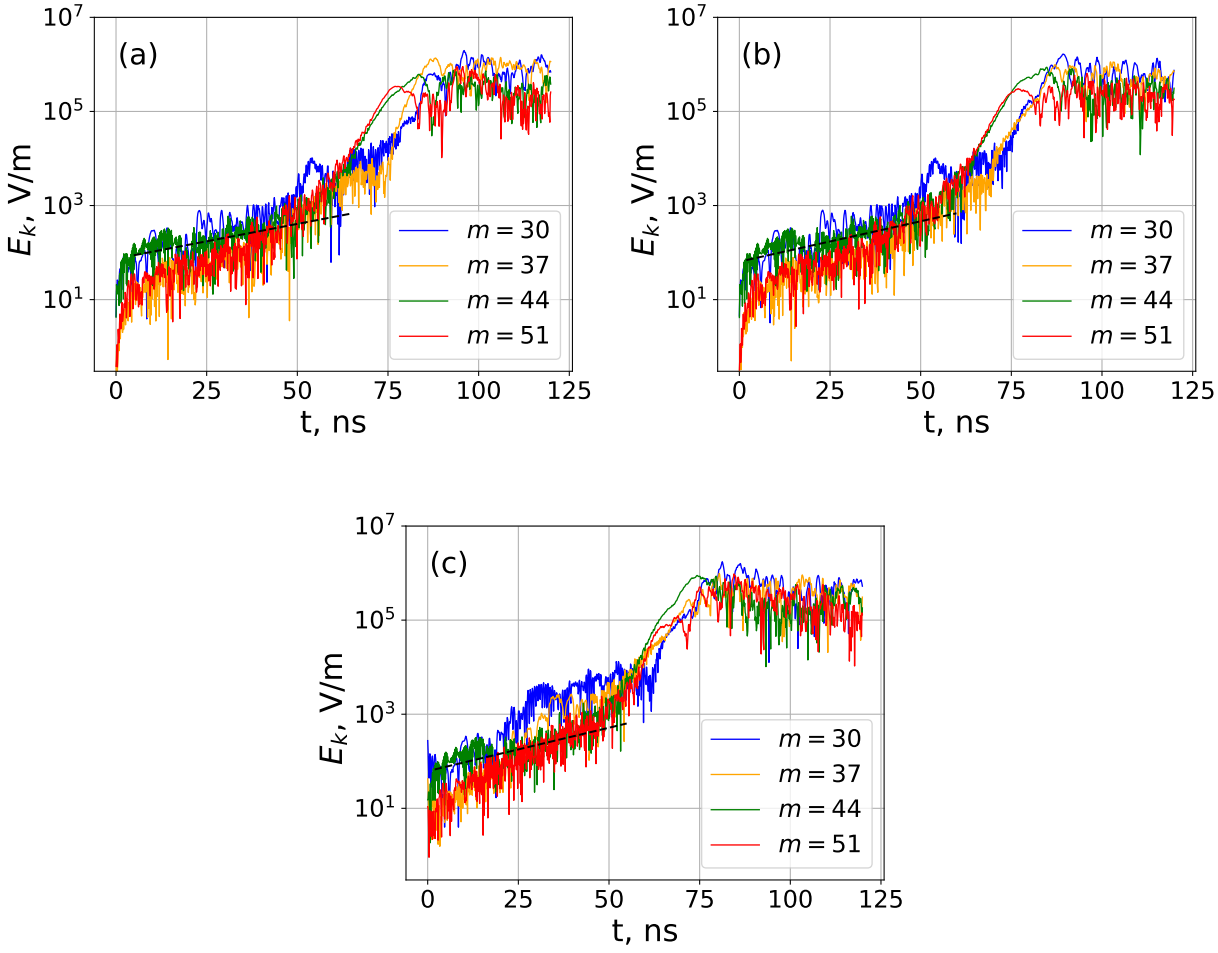

Figure 3.14: The evolution of individual modes of the electric field in quiet-start PIC simulations using 10^4 macroparticles per cell from a) PIC10 b) PIC11 c) PIC12 simulation. All figures are generated from the EDIPIC simulation code. The dashed black line shows the fitted line on the $m = 44$ mode. 1 ns =17.84 ω_{pe}^{-1} [The data used for the production of this figure are produced by Trevor Zintel].

rates. In random-start PIC simulations, the flattening of the electron distribution function occurs as a result of the early trapping of electrons in the noise-driven potential, as can be seen in Fig. 3.9. In Section 3.5, we show that for large streaming velocity, $v_0 = 6v_{te}$, the random-start PIC simulations can reproduce the linear growth rates with reasonable accuracy. This limit is close to the cold-plasma limit ($T_i \to 0$ and $T_e \to 0$), so that the effects of electron VDF are not important, and the linear growth rates are close to their maximum cold-plasma values.

The noise of the PIC simulations can be further reduced by increasing the number of macroparticles. We show that the results up to 10^5 macroparticles per cell (PIC4 and PIC5 simulations) will reduce the discrepancy, though the growth rates measured in PIC simulations remain far from the linear theory. Computational resource constraints made it impractical to increase the number of macroparticles per cell much beyond 10^5; in principle, such an increase would increase the accuracy. On the other hand, the Vlasov simulations were able to reproduce the linear growth rates accurately within these constraints.

The effect of the noise resulting from the random sampling of the phase space with a limited number of macroparticles can be partially mitigated by the quiet-start [81]. The accuracy of the growth rates from PIC simulations is greatly increased using the quiet-start initialization method but only if the maximum growth rate mode is perturbed initially. However, the noise is still significant in the linear growth of the quiet-start PIC simulations, and some of the growth rates remain inconsistent with their theoretical values. Therefore, the quiet-start method is not likely to completely remedy the problem of excessive noise in practice.

In the PIC simulations of this study, the quiet-start method uses a bit-reversed sequence in the spatial subspace and a uniform sequence in the velocity subspace [41]. These sequences are chosen because of their relative popularity and regularity, which greatly decreases the initial noise level. We also tried a bit-reversed sequence in velocity space, but the resulting growth rates were not as accurate as from the uniform sequence, and therefore, we did not report the results. In practice, other sequences may give different accuracy; however, a systematic comparison of the various proposed sequences is beyond the scope of this study.

The issue of increased noise in PIC simulations is also related to a more general discussion as to what degree the PIC method, which works in between the exact Klimontovich equation and the asymptotic Vlasov equation, describes reality. In the PIC approach, the finite-sized charged clouds may still experience some binary interactions absent in the Vlasov equation but to some degree resembling Coulomb particle collisions [100, 101, 71, 102, 81].

For the simulations reported in this study, we have calculated the standard error associated with the measurement of the growth rates. For our purpose, the SE also provides a measure of deviation from linear growth, i.e., the extent to which the observed growth is linear as theory suggests. In the random-start PIC simulations, we observe highly oscillatory growth, and therefore, the SE is the largest for these simulations. However, the inaccuracy of the growth rates is so large that they fall outside the 99% confidence interval of the theoretical growth rates. On the other hand, the growth of the low-noise Vlasov simulation is clearly linear, and therefore, the SE is much less than unity for them. Depending on the simulation code, the SE in

the quiet-start PIC simulations can be larger or smaller than the SE in the random-start PIC simulations. Another quantity that we calculate for our simulations is the signal-to-noise ratio (SNR) during the growth of unstable modes. The SNR is largest for the Vlasov simulations, indicating the relatively low power of the noise carried in these simulations. In contrast to the SE, we show that the SNR in the quiet-start PIC simulations is less than that using random-start.

Some modern methods of PIC simulation are proposed to reduce the noise level for a given number of macroparticles. Among these methods, the remapping and the delta-f methods have gained special attention recently. In the remapping method, the microparticles of the PIC simulation are frequently interpolated to a grid in phase space [103, 104]. In this way, the noise level is decreased, but the computational cost is increased. In the delta-f method, the known part of the distribution function is separated from its variation (i.e., $f = \bar{f} + \delta f$, where $\bar{f}$ is the known distribution function and δf is its variation) [105, 106, 107]. The existing macroparticles are only used to resolve the variation part instead of the distribution function, and therefore, the computational resources are allocated efficiently to reduce noise. However, to keep the noise level small, the condition $\delta f/\bar{f} \ll 1$ should be satisfied in the simulation. This condition is usually satisfied in the linear regime of instabilities (as in this study), but it may not quite be satisfied in the nonlinear regime if the distribution function significantly deviates from its initial shape. It is expected that the remapping or delta-f method may ameliorate the noise problem of PIC simulations reported in this study. However, confirming this expectation would require other experiments that are beyond the scope of this study.

Acknowledgments

This work was supported in part by the U.S. Air Force Office of Scientific Research FA9550-21-1-0031, NSERC Canada, and by computational facilities of Compute Canada. A.S. acknowledges illuminating discussions with S. Janhunen.

Author Declarations

Conflict of interest

The authors have no conflicts to disclose.

Data Availability Statement

The data that support the findings of this study are available from the corresponding author upon reasonable request.

4 Backward waves in the nonlinear regime of the Buneman instability

4.1 Preface

In the last chapter, we discussed the effect of the simulation method of the Buneman instability, on the linear regime of this instability. In this chapter, we mainly discuss the nonlinear regime of this instability. The backward waves are a class of counter–intuitive nonlinear waves that propagate against the direction of the initial drift of particles and are observed in our Vlasov simulations of the Buneman instability. Understanding the behavior of backward waves through simulations can help understand many nonlinear phenomena such as anomalous transport and heating. In the Hall thrusters and hollow cathode plasmas, this knowledge can help understand the parallel instabilities and their signature on the anomalous transport and cathode sputtering. The backward waves can also explain the anomalous resistivity in the space plasmas.

This chapter is based on an article published in the Physics of Plasma journal [88]. The author of this thesis (A. Tavassoli) is the first author of the published article and had the highest contribution among the co-authors of this article. This contribution is as follows.

- Leading the investigation, and formal analysis of the study.
- Managing comments, suggestions, and discussions of the co-authors and reflecting them in the text of the article.
- Organizing, writing, and preparing most of the text of the article throughout the preparation and submission processes.
- Having a dominant role in the development of the "semi-Lagrangian Vlasov" code used in the article.
- Running all the simulations in the article and producing the data for making the corresponding figures.
- Post-processing with Python and producing some figures of the article.
- Being the corresponding author of the article. All correspondence with the editorial office during the publication process was done through the corresponding author.
- Reflecting the comments of the reviewers in the text of the article and preparing the text of the reply to reviewers, after discussing them with the co-others.

For clarifying the contribution of co-authors in producing the figures, their names are printed in the caption of each figure.

4.2 Abstract

Observation of low- and high-frequency backward waves in the nonlinear regime of the Buneman instability is reported. Intense low-frequency backward waves propagating in the direction opposite to the electron drift (with respect to the ion population) of ions and electrons are found. The excitation of these waves is explained based on the linear theory for the stability of the electron velocity distribution function that is modified by nonlinear effects. In the nonlinear regime, the electron distribution exhibits a wide plateau formed by electron hole trapping and extends into the negative velocity region. It is shown that within the linear approach, the backward waves correspond to the weakly unstable or marginally stable modes generated by the large population of particles with negative velocities.

4.3 Introduction

The Buneman instability is a two-stream type instability driven by the relative drift v_0 of electrons with respect to ions in an unmagnetized cold plasma. It has been studied in numerous settings as a mechanism of turbulence and source of anomalous resistivity in space plasmas [26, 27, 28, 29, 30], as a generation mechanism for short wavelength radiation sources [31], in ion beam fusion applications [32], and many others. The linear regime of this instability has been well studied and understood for some time [108, 109]. In contrast, the nonlinear regime is complicated, and its various aspects are still subjects of interest. The nonlinear dynamics of trapping and the resultant holes [110, 111, 112, 113], the long-time behaviour of the nonlinear regime [114, 115, 116], and nonlinear Landau damping [117] are among such aspects of the problem. In this regard, numerical simulations play an important role complementing the analytical theories. Over the past decades, many numerical studies have been performed to reveal various nonlinear phenomena in the Buneman instability [87, 118, 85, 119, 86, 86, 120]. Despite these efforts, however, theoretical explanations for a variety of the observed nonlinear phenomena remain elusive.

Ref. [121] provides one of the first descriptions of the effects of nonlinear mode coupling. It predicts a decline in the linear growth rate accompanied by a nonlinear, oscillatory growth, but it fails to predict the saturation level of the instability. Following a similar approach, Refs. [122, 123] calculate the ion susceptibility, taking into account the nonlinear mode-coupling and thus expanding the quasi-linear dispersion relation into the nonlinear regime. In contrast with Ref. [121], this theory predicts the saturation, the initial depression of the relative drift velocity, and the initial heating of electrons. However, as soon as electron trapping becomes important, this theory fails in its predictions for various quantities such as drift velocity and ion susceptibility. Electron trapping is later incorporated into the model in a companion paper [124], and the effects on the ion dynamics are investigated. In another effort, Ref. [125] develops a weak turbulence theory for the nonlinear

regime of the Buneman instability. This theory is shown [126] to explain some characteristics of the nonlinear evolution seen in numerical simulations. However, the shape of the electron velocity distribution function (VDF) is taken as a shifted Maxwellian at all times, whereas various simulations show that in the nonlinear regime, the VDF deviates significantly from a shifted Maxwellian. The criteria for applicability of quasilinear theory are not satisfied in many situations [127]. It is our goal in this study to investigate the nonlinear stage of the strong Buneman instability when the whole electron population is streaming with respect to the ions, both components are warm, and they have the same initial temperatures. This regime is characterized by the excitation of large-amplitude fluctuations of the potential, the strong modification of the electron distribution function and heating due to the electron reflections and trapping, and as a consequence, the excitation of the waves in the direction opposite to the beam velocity.

In many situations, large deviation of the distribution function from the initial Maxwellian is a defining feature of the nonlinear evolution. This feature has led to an approach in which the nonlinearly modified VDF is used in the linear dispersion relation to interpret and explain the mode behavior. For example, the suppression of Landau damping in the nonlinear regime can be understood from the fact that the nonlinear VDF develops a plateau that stops the Landau damping [128] due to the commonly used local criterion $\partial f/\partial v > 0$ from the linear theory of Landau damping (Fig. 4.1). This criterion suggests that for $\partial f/\partial v > 0$, the modes with phase velocity close to the resonant condition $\omega = kv$ become unstable, whereas in the region of the negative slope of the VDF with $\partial f/\partial v < 0$, the modes are damped. It is important to note that for the waves with negative phase velocity and for which the velocity of resonant particles is also negative, $v = \omega/k < 0$, the situation is reversed, so that $\partial f/\partial v < 0$ is required for the instability, and for $\partial f/\partial v > 0$, resonant modes are damped. In both cases, a region of zero slope in the VDF (or a plateau) leads to the marginal stability of the modes with the phase velocity in the plateau region; see Fig. 4.1.

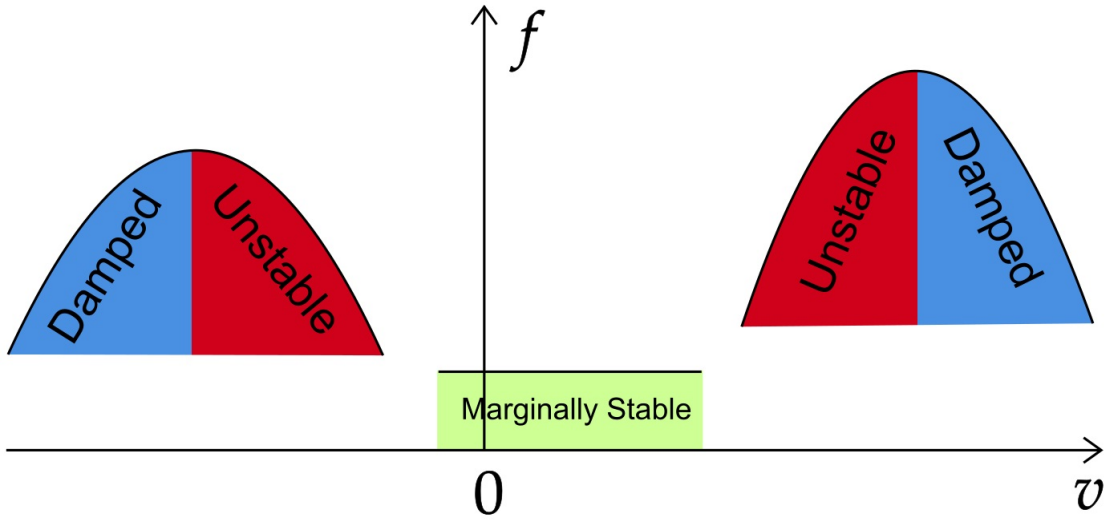

Figure 4.1: The regions of damped, unstable, and marginally stable modes according to the local criterion from the linear theory of Landau damping.

Although the local instability criterion is often useful and insightful, the whole profile of the distribution function is required in general to determine the full linear stability as embodied in various integral stability criteria, e.g., the Penrose criterion [129]. The linear analysis on the modified distribution function has explained new types of waves such as nonlinear electron-acoustic waves (EAWs) [130, 131, 132]. EAWs are a class of nonlinear waves with phase velocity close to the electron thermal velocity. According to the linear theory of Landau damping, these modes are expected to be damped, whereas simulations show that they are marginally stable. To explain this behavior, the theory developed in Refs. [131] and [133] used the standard Maxwellian VDF with an additional term that accounts for the small plateau seen in the simulations. Based on the linear dispersion relation, this plateau is found to be responsible for new modes termed "corner modes". The existence of a large-amplitude wave, propagating with the phase velocity near the zero-slope inflection point of the electron VDF, has also been demonstrated in Ref. [113]. Even though Ref. [134] argued that a purely nonlinear theory taking into account particle trapping is necessary to explain the new modes seen in Ref. [131], it seems unavoidable that the existence of these modes is in large part related to the suppression of Landau damping due to flattening of the distribution function, an effect that has clear interpretation in the linear theory.

The linear analysis using the dispersion relation based on the modified distribution function is also used in other nonlinear studies [26, 29, 135, 136]. In Refs. [26, 29, 135, 136], a two-Maxwellian VDF was fit to the nonlinear VDF found from the simulations. The resulting distribution function is then fed into the linear dispersion relation. The solution of this dispersion relation leads to the frequencies and growth rates of the modes observed in the simulations.

We employ a similar approach in this study, where using a low-noise, high-resolution, grid-based Vlasov solver, we observe the nonlinear excitation of strong waves that propagate in the direction opposite to that of the initial electron drift. These waves are referred to below as *backward waves*. Backward waves have been observed in some simulations of current-driven instabilities, and they are believed to have important effects on the nonlinear evolution of these instabilities [16, 28, 137, 136, 30]. However, the origin of these backward waves is still not well understood. Different scenarios such as secondary linear instability [136], three-wave decay [138], and induced scattering off ions [28, 138] are mentioned as possible mechanisms for the excitation of these waves. The backward waves are generated well into the nonlinear regime and are not generally expected based on the linear theory of the Buneman instability, in which the Maxwellian electron population is streaming with respect to the (also Maxwellian) ions. In this study, we report the observations of low-frequency (ion-sound-like) and high-frequency (Langmuir-like) backward waves. The intensity of the ion-sound-like waves is much higher than that of the high-frequency mode, the amplitude of which also decreases further into the nonlinear regime.

In the nonlinear stage, the electron VDF strongly deviates from Maxwellian. The electron VDF is modified by the trapping in the holes and forms a plateau that extends well into the negative velocity region. The plateau in the negative velocity region allows for the existence of weakly unstable and marginally stable

backward (and forward) waves that otherwise would suffer Landau damping. This situation is similar to the observations in Refs. [131, 139, 113, 140], where the trapping of electrons or ions forms a plateau in the VDF and allows for a new class of waves. Here, we show that the nonlinear VDF observed in simulations is susceptible to the excitation of backward waves observed in simulations.

We use the VDF from simulations averaged over time intervals of about 15 $\omega_{pi}^{-1} \sim 20\ \omega_{pi}^{-1}$, where ω_{pi} is the ion plasma frequency. These time intervals are long enough to get clear view of the low-frequency modes in the fast Fourier transform (FFT) of the electric field from nonlinear simulations. These spectra are compared with results of the linear stability analysis performed on the actual distribution function obtained by averaging for each interval.

The remainder of the paper is organized as follows. In section 4.4, we review the linear dispersion relation of the Buneman instability and its solution for the cases of this study. In particular, we show that the linear growth rates calculated our simulations are in agreement with the linear theory for the initial Maxwellian distribution. In section 4.5, the general setup of the nonlinear problem and simulations is reported. We have performed simulations with $v_0 = 4v_{te}$ and $v_0 = 10v_{te}$. In section 4.6, the linear analysis based on the modified VDF is applied to the simulation results, and its predictions with regard to backward and forward waves are discussed. In section 4.7, two other simulations with $v_0 = 1.5v_{te}$ and $v_0 = 1.75v_{te}$ are compared, and accordingly, we show that a threshold for excitation of backward waves lies between these two values. We also show that for values of v_0 less than this threshold, the formed plateau in electron VDF is not wide enough to extend into the negative velocity region, and therefore, backward waves do not appear. In section 4.8, we conclude our study with a discussion of the results.

4.4 Linear regime of the Buneman instability

The Buneman instability is the electrostatic instability driven by the relative drift of plasma species. In the limit that both electron and ion temperatures vanish, the dispersion relation of the Buneman instability is

$$1 - \frac{\omega_{pe}^2}{(\omega - kv_0)^2} - \frac{\omega_{pi}^2}{\omega^2} = 0. \tag{4.1}$$

Here, ω is the eigenmode frequency, k is the wave vector, v_0 is the initial drift velocity of the electrons, ω_{pi} is the ion plasma frequency, and ω_{pe} is the electron plasma frequency. The instability occurs for $kv_0 < \omega_{pe}(1 + (m_e/m_i)^{1/3})^{3/2}$, with the maximum mode growth rate $\gamma = \frac{\sqrt{3}}{2}(\frac{m_e}{2m_i})^{1/3}\omega_{pe}$ at $k \approx \omega_{pe}/v_0$, and real part of the frequency $\omega = \frac{1}{2}(\frac{m_e}{2m_i})^{1/3}\omega_{pe}$.

Considering ions and electrons with finite temperatures, the dispersion relation reads

$$1 - \frac{\omega_{pi}^2}{2k^2v_{ti}^2}Z'\left(\frac{\omega}{\sqrt{2}|k|v_{ti}}\right) - \frac{\omega_{pe}^2}{2k^2v_{te}^2}Z'\left(\frac{\omega - kv_0}{\sqrt{2}|k|v_{te}}\right) = 0, \tag{4.2}$$

where $v_{ti} = \sqrt{T_{i0}/m_i}$ and $v_{te} = \sqrt{T_{e0}/m_e}$ are the ion and electron initial thermal velocities and T_{i0} and T_{e0} are the initial temperature of ions and electrons. In this study, we take $T_0 = 0.2$ eV as the initial temperature

for both ions and electrons. The equal ion and electron temperature regime is of particular interest for the study of solar plasmas [27]. We note that therefore, the ion sound velocity c_s is equal to the v_{ti}. Also, we take $n_0 = 10^{17}\mathrm{m}^{-3}$ as the plasma density.

Using these parameters, Figs. 4.2a and 4.2b show the solution of Eq. (4.2), for the two drift velocities cases $v_0 = 4v_{te}$ and $v_0 = 10v_{te}$ (note the different axis ranges). These two drift velocities are also considered in the nonlinear simulations of this study. With periodic boundary conditions, as used here, only the modes satisfying the condition $kL/2\pi = m$ for integer m are allowed. In the case of $v_0 = 4v_{te}$, the most unstable mode corresponds the wave number $m = 26$. The case $v_0 = 10v_{te}$ is closer to the cold plasma limit $v_0/v_{te} \gg 1$. In this case, the positive growth rate region is shorter, and the most unstable mode corresponds to the wave number $m = 9$. The growth rate diagram is also sharper, and the maximum growth rate has increased. Backward waves cannot be observed in the solution of linear dispersion of the Buneman instability, and therefore, we have omitted the negative k region from Figs. 4.2a and 4.2b. In Figs. 4.2a and 4.2b, we have also reported the growth rate of some chosen electric field modes as measured from the simulations. The evolution of the amplitude of these chosen modes is shown in Figs. 4.3b and 4.4b. As we see, after some initial oscillations, the amplitude of each mode shows linear growth. The slope of this linear growth is used to measure the growth rate of each mode.

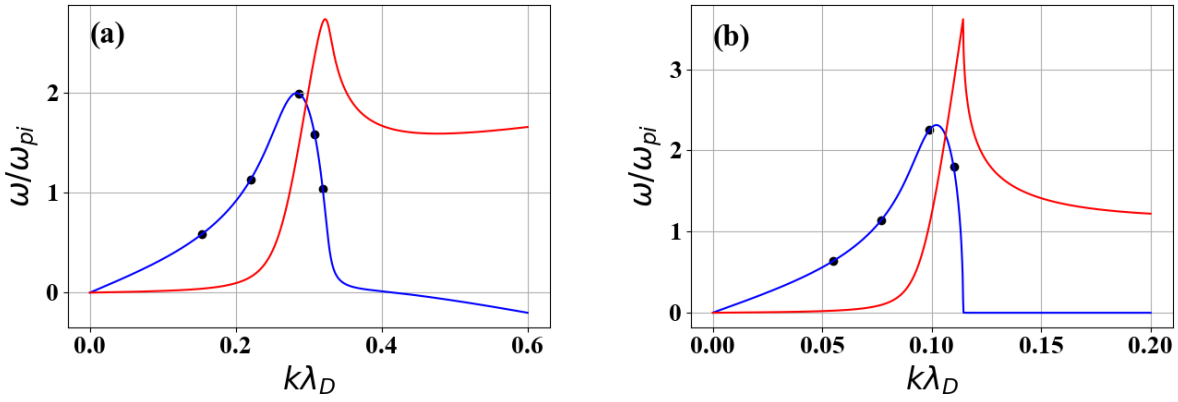

Figure 4.2: (a) The linear growth rate (blue) and frequency (red) for the case of $v_0 = 4v_{te}$. (b) The linear growth rate (blue) and frequency (red) for the case of $v_0 = 10v_{te}$. The black circles show the growth rates measured from the simulation [The data used for the production of this figure are produced by Mina Papahn Zadeh]. (Note the different axis ranges.)

4.5 Nonlinear Vlasov simulations

In our simulations, we solve the Vlasov–Poisson equations

$$\frac{\partial f_s}{\partial t} + v_x \frac{\partial f_s}{\partial x} + \frac{qE_x}{m_s}\frac{\partial f_s}{\partial v_x} = 0,$$
$$\frac{\partial E_x}{\partial x} = e(n_i - n_e), \tag{4.3}$$

where f_s is the distribution function for species s, $s = i, e$ for ions and electrons, respectively, E_x is the electric field, $n_s = \int f_s \, \mathrm{d}v_x$ is the density of species s, q is the charge, which is $+e$ for the ions and $-e$ for the electrons, and m_s is the mass of species s. The ions are taken to be Hydrogen with mass $m_i = 1$ amu.

The numerical method used is the well-known and tested semi-Lagrangian splitting scheme [90, 48]. In this method, the Vlasov equation is split into a convection equation and a force equation. Each of these equations is then solved by the method of characteristics and cubic spline interpolation. The boundary condition is periodic in space and open in the velocity direction. The Poisson equation is solved by a spectral method, the FFT. The initial conditions are

$$f_e(x, v, 0) = \frac{n_0(1 + \epsilon k_0 \cos(k_0 x))}{\sqrt{2\pi} v_{te}} \exp\left(-\frac{(v - v_0)^2}{2v_{te}^2}\right), \tag{4.4}$$

$$f_i(x, v, 0) = \frac{n_0}{\sqrt{2\pi} v_{ti}} \exp\left(-\frac{v^2}{2v_{ti}^2}\right). \tag{4.5}$$

The quantities $\epsilon = 10^{-8}\lambda_D$, where $\lambda_D \equiv \sqrt{\epsilon_0 T_0 / n_0 e^2}$ is the Debye length, and $k_0 = \frac{2\pi}{L}$ parameterize an initial small perturbation. These parameters are required to excite the instability because the method for solving the Vlasov formulation inherently introduces little numerical noise. For this study, we also tried the perturbation with the most unstable mode and also several perturbed modes, and we confirmed that the results are not sensitive to the choice of initial perturbation. The system length is taken $L = 6$ mm, which is approximately 570 Debye lengths, and a spatial grid of 4096 points is used. This length is large enough to contain many unstable modes, including the mode with maximum linear growth rate (see Figs. 4.2a and 4.2b). The velocity grids for ions and electrons consist of 1921 and 4033 points, respectively. The time-step used in the simulations is $2 \times 10^{-3}\ \omega_{pi}^{-1}$, which is about $0.086\ \omega_{pe}^{-1}$. Therefore, the time step is small enough to resolve fast variations of the plasma. We note that $\omega_{pi}^{-1} = 2.39$ ns in this setup.

After a few nanoseconds of simulation, the electric field energy starts to grow linearly and continues until it reaches a peak. This peak is followed by a slow decay due to the energy transfer from the waves to the plasma and particle heating (Figs. 4.3a and 4.4a). The nonlinear regime is characterized by the appearance of trapping holes in the ion and electron distribution functions. The ion holes correspond to negative electrostatic potential, whereas the electron holes correspond to positive electrostatic potential [110]. The electron holes appear early in the nonlinear regime and in the bulk region of the distribution function (Fig. 4.5a, left). As we see in the left figure in Fig. 4.5a, the number of these holes in the early nonlinear regime is close to the mode number of the most unstable mode (26, in the case of $v_0 = 4v_{te}$). The left figure in Fig. 4.5b

shows the potential profile at the same time as the left figure in Fig. 4.5a. The large-amplitude (rogue) waves about 1.5 V to 2 V can be seen in this figure. This amplitude is of the same order of magnitude as the initial drift energy of electrons ($1/2m_e v_0^2 \approx 1.6$ eV). Early electron holes then merge together and form larger holes (Fig. 4.5a, right) in a process discussed by a number of previous works [114]. This process of merging leads to the appearance of higher wavelengths in the potential profile (Fig. 4.5b, right). In addition, the ion holes appear in the tail of the distribution function later in the nonlinear regime (Fig. 4.5c, right). Backward-propagating waves appear in the early nonlinear regime after the wave amplitude is large enough to significantly reflect the electrons backward and extend the plateau to the negative regions of electron VDF. Backward and forward waves can be seen clearly in Figs. 4.7 and 4.8.

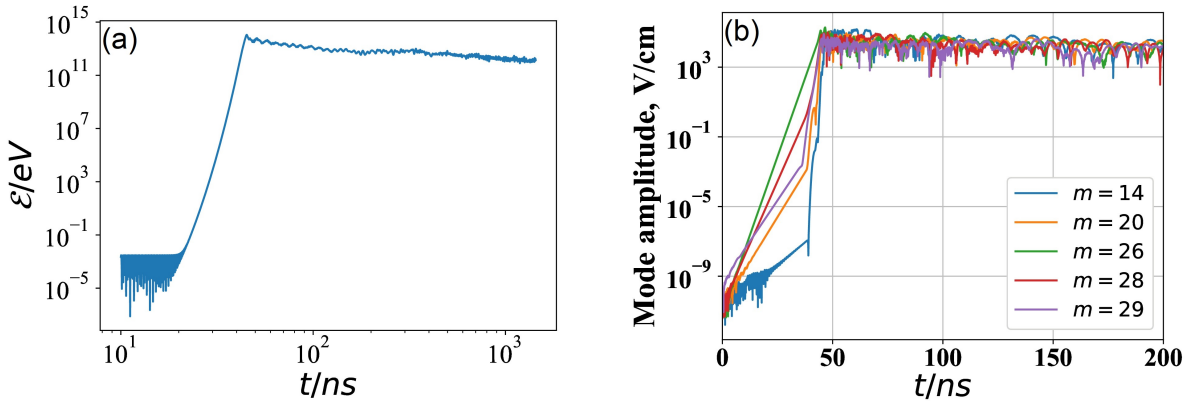

Figure 4.3: a) The electric field energy ($\mathcal{E}$) versus time. b) The evolution of the amplitude of the individual electric field modes. The case of $v_0 = 4v_{te}$.

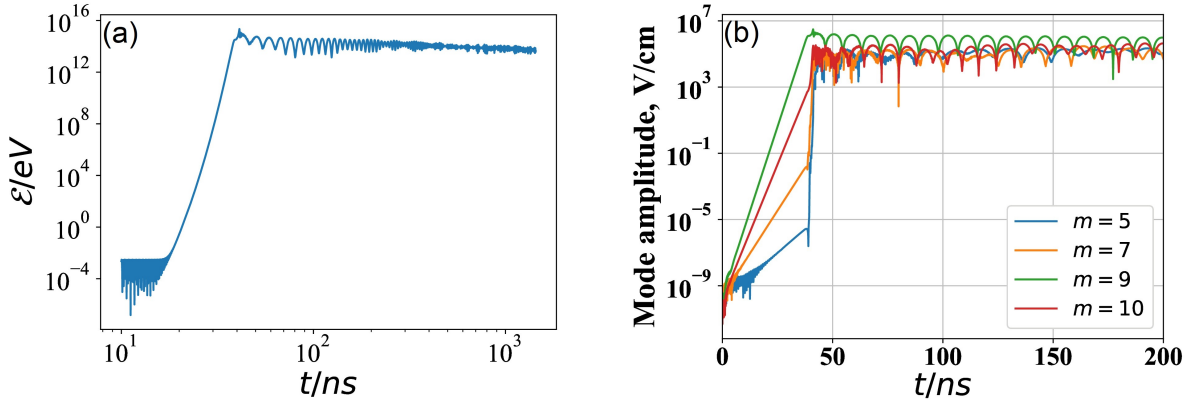

Figure 4.4: a) The electric field energy ($\mathcal{E}$) versus time. b) The evolution of the amplitude of the individual electric field modes. The case of $v_0 = 10v_{te}$.

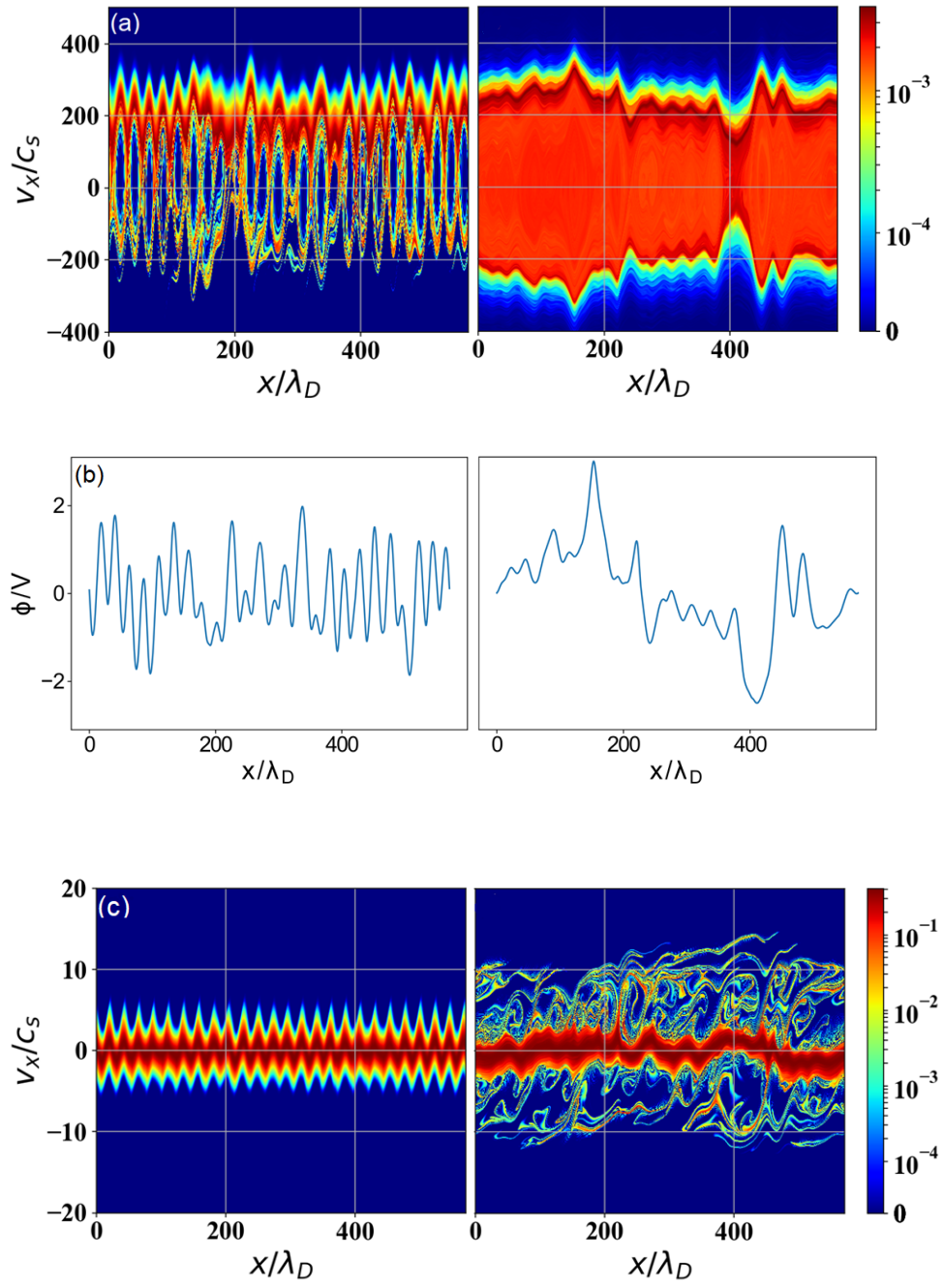

Figure 4.5: (a) The electron distribution function in n_0/c_s, (b) Electrostatic potential, (c) The ion distribution function in n_0/c_s. In each row, the figure on the left-hand side is at $t = 47.39$ ns ($19.8\ \omega_{pi}^{-1}$), and the figure on the right-hand side is at $t = 163.22$ ns ($68.2\ \omega_{pi}^{-1}$). These figures correspond to the case of $v_0 = 4v_{te}$.

The electron scattering from large-amplitude fluctuations of the potential results in a dramatic increase of the electron temperature. Fig. 4.6 shows the evolution of the (spatially averaged) temperature

$$T_e = \frac{1}{n_0 L} \int m_e (v_x - V_{xe})^2 f_e(x, v_x, t)\, \mathrm{d}x\, \mathrm{d}v_x. \tag{4.6}$$

The fluid velocity V_{xe} is the first moment of distribution function; i.e., $V_{xe} = \int v_x f_e \, \mathrm{d}v_x / \int f_e \, \mathrm{d}v_x$. The electron energy starts to increase in early nonlinear stage (after about 47 ns), at the same time when the rogue waves appear in the potential and the backward waves are generated. The electron temperature then saturates to about 2.4 eV. We note that this value is of the same order of magnitude as the amplitudes of the sharp peaks in Fig. 4.5b.

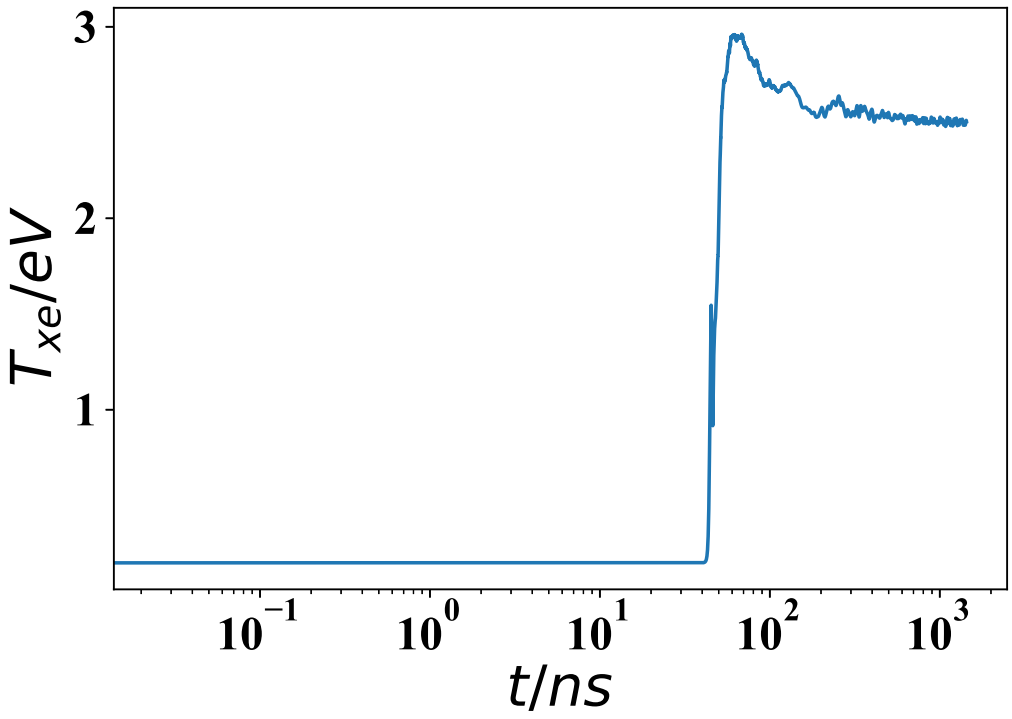

Figure 4.6: The evolution of electron temperature for the case $v_0 = 4v_{te}$

The rest of the paper is dedicated to the characteristics of the spectra (backward and forward waves) in the nonlinear stage obtained in simulations and from analytical calculations. Before that, however, it is interesting to note another nonlinear phenomenon that can be seen in our results. In all of our simulations, we see a significant group of electrons that have been accelerated ahead of the initial drift velocity, as seen in the electron VDF (see for example the small bump and energetic tail in the right-hand side of VDF, in Figs. 4.9 and 4.13). This acceleration is likely due to the electron trapping and de-trapping in the large-amplitude (forward) waves. Similar self-acceleration of the beam in the two-stream instabilities has been studied earlier in Ref. [120, 141].

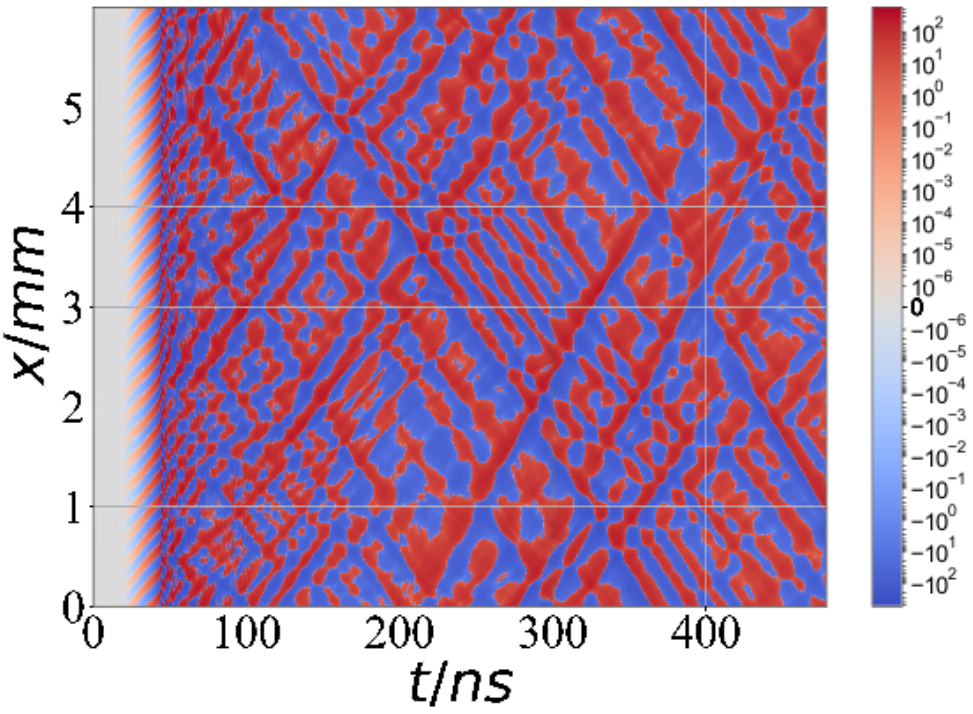

Figure 4.7: The electric field (V/cm) as a function of time and position for the case of $v_0 = 4v_{te}$. After the backward-propagating waves appear at around $t = 45$ ns, the coexistence of backward and forward waves forms a grid pattern in the electric field profile.

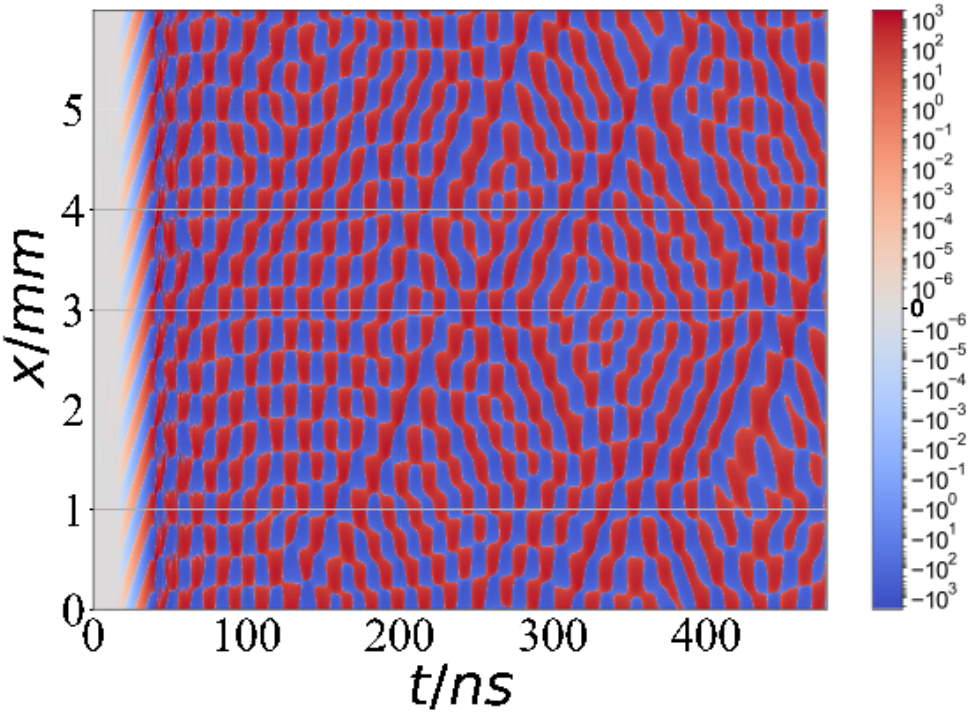

Figure 4.8: The electric field (V/cm) as a function of time and position for the case $v_0 = 10\,v_{te}$. After the backward-propagating waves appear at around $t = 30$ ns, the coexistence of backward and forward waves forms a grid pattern in the electric field profile.

4.6 Backward waves as marginally stable eigenmodes of the non-linearly modified velocity distribution function

As discussed above, the electron distribution in the nonlinear stage is strongly modified. To study the stability of such distributions, we represent the electron VDF obtained from the simulation by ten electron beams, each with a beam density of δ_j, in the form

$$f_e(v_x) = \sum_{j=1}^{10} \frac{n_0 \delta_j}{\sqrt{2\pi} v_{ej}} \exp\left(-\frac{(v_x - v_{0j})^2}{2 v_{ej}^2} \right). \tag{4.7}$$

The δ_j are normalized by the condition $\sum_{j=1}^{10} \delta_j = 1$. Fig. 4.9 shows the evolution of the spatially averaged electron VDF in the case $v_0 = 4v_{te}$. It can be seen that in each time interval, the VDFs of Eq. (4.7) can be closely fit to the simulated VDFs. The fit is done using the SciPy *curve_fit* function, which uses the least-squares method to non-linearly fit the ten-Maxwellian VDF Eq. (4.7) to the simulated VDF. The positivity of the beam densities (δ_j) and beam thermal velocities (v_{ej}) was enforced in the fit. We note that some of the beam velocities v_{0j} in the fit have a negative value, which is important for the fit to be well extended to the negative velocities. In general, the more Maxwellian functions we use for the fit, the more accurate it is. However, using more than ten Maxwellians does not significantly change the value of the standard error as returned by the fitness function. We have also checked that that lower error does not have much impact on the theoretical spectrum of the eigenmodes. Each fit results in a set of 29 independent parameters δ_j, v_{0j}, v_{ej}. Using these parameters, we solve the corresponding dispersion equation

$$1 - \frac{\omega_{pi}^2}{2k^2 v_i^2} Z'\left(\frac{\omega}{\sqrt{2}|k| v_i} \right) - \sum_{j=1}^{10} \frac{\delta_j \omega_{pe}^2}{2k^2 v_{ej}^2} Z'\left(\frac{\omega - k v_{0j}}{\sqrt{2}|k| v_{ej}} \right) = 0 \tag{4.8}$$

for the theoretical spectrum and growth rates of the waves. For the case $v_0 = 4v_{te}$, the ion distribution function does not change much, so we use the initial value of the ion temperature (v_{ti}) for v_i. For $v_0 = 10v_{te}$, we observe a slight modification of the ion distribution; it is described below.

4.6.1 Linear eigenmode spectra for $v_0 = 4v_{te}$

Figs. 4.10a to 4.10d show the spectrum of nonlinear waves in four subsequent stages of nonlinear simulations. In each figure, we also show the eigenmodes obtained from the solution of Eq. (4.8). In general, the modes in two different regions can be seen in these figures: the arc-shaped high-frequency modes with $\omega \sim O(\omega_{pe})$ (Langmuir-like modes) and the low-frequency modes with $\omega \sim O(\omega_{pi})$ (ion-sound-like). We note that, for the FFT in time, we have used the Hanning window to reduce the amount of spectral leakage [142]. Despite this, some faint modes can be seen in between. The time intervals were taken long enough so that the FFT has a relatively high resolution and can clearly show the low-frequency modes. As we see, the amplitudes of the low-frequency modes are several orders of magnitude larger than those of the high-frequency modes, and

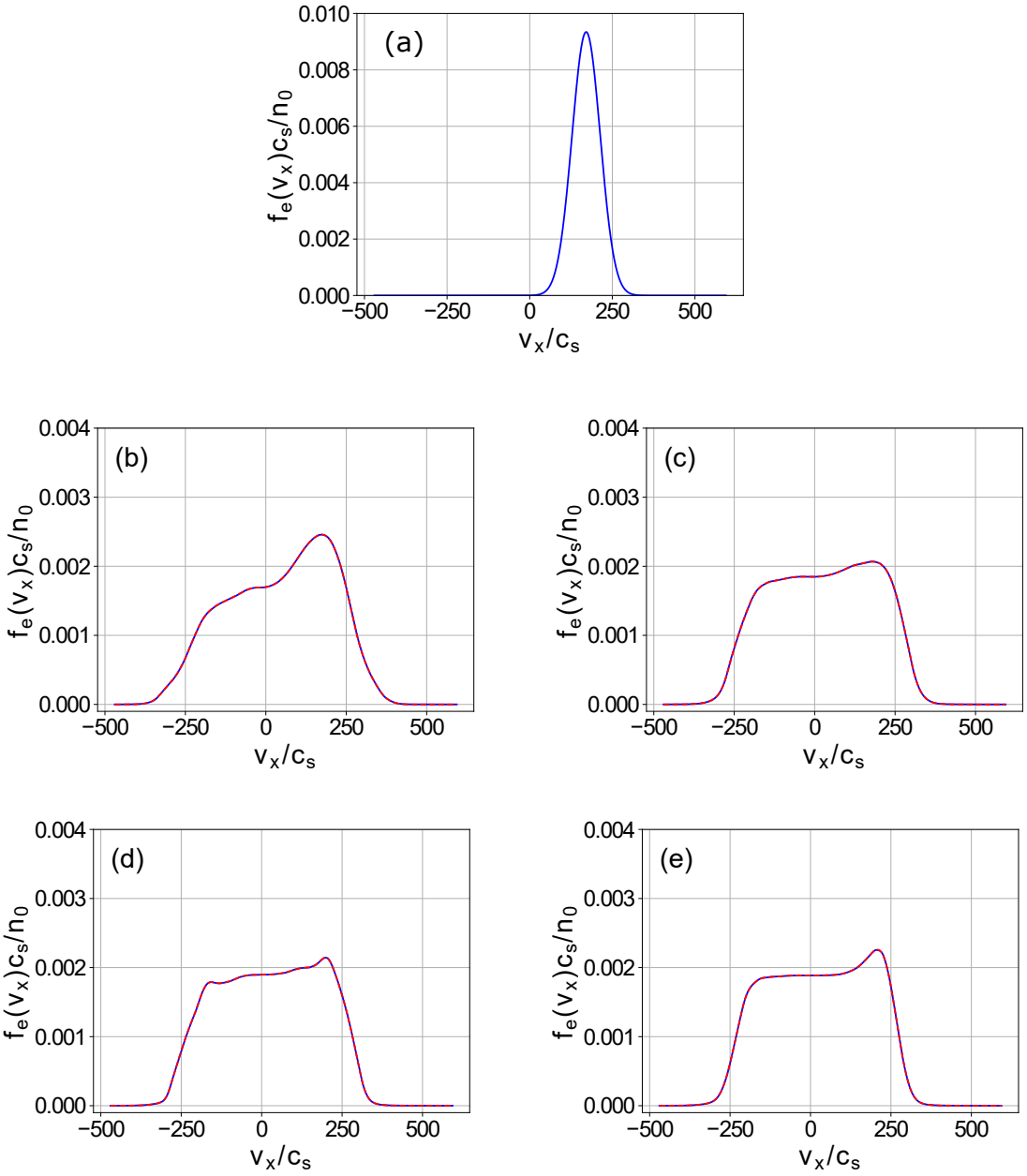

Figure 4.9: Evolution of the electron VDF for $v_0 = 4\,v_{te}$. (a) the initial VDF at $t = 0$ (b) VDF from nonlinear simulations (blue line) averaged over $19.8\,\omega_{pi}^{-1}$ to $34.8\,\omega_{pi}^{-1}$ (c) $34.8\,\omega_{pi}^{-1}$ to $51.4\,\omega_{pi}^{-1}$ (d) $51.4\,\omega_{pi}^{-1}$ to $68.2\,\omega_{pi}^{-1}$ (e) $68.2\,\omega_{pi}^{-1}$ to $100\,\omega_{pi}^{-1}$. The fit from Eq. (4.7) is shown in red in (b),(c),(d), and (e).

therefore, they are dominant in the nonlinear regime. The phase velocity of the low-frequency modes is close to the velocity of the ion holes in the ion distribution function (Fig. 4.5c, right).

Fig. 4.11a to Fig. 4.11d show the theoretical mode frequencies ω and corresponding growth rates γ for the distribution function from the corresponding time intervals of Fig. 9. In these figures, we have omitted growth rates less than $-0.1\omega_{pi}$. We can see small positive or near-zero growth rates in the range of $|k\lambda_D| \lesssim 0.4$, whereas the modes outside of this range are strongly damped due to the ion Landau damping, which is significant for phase velocities around $O(v_{ti})$. These spectra of the weakly unstable or marginally stable eigenmodes in the range $|k\lambda_D| \lesssim 0.4$ show close resemblance to the eigenmode spectra obtained in the nonlinear simulations (Fig. 4.10a to Fig. 4.10d).

In Fig. 4.11, we observe the asymmetry between positive and negative k for the Langmuir-like (high-frequency) modes. This asymmetry is a result of asymmetric damping of the positive and negative k modes, and it can also be seen in the simulation results (Fig. 4.10). Our theoretical analysis of the eigenmode spectra of the modified distribution function also shows these high-frequency modes with near-zero or negative growth rates as seen in Fig. 4.11a to Fig. 4.11d. Similarly, in our simulations, these modes fade away further as seen in the last time window (Fig. 4.10d).

4.6.2 Linear eigenmode spectra in the cold plasma limit of the Buneman instability ($v_0 = 10v_{te}$)

Increasing the initial electron drift to $v_0 = 10v_{te}$ leads to a stronger instability, which saturates to a much higher value of electric field energy (Fig. 4.4a) and increases the electron and ion heating. In order to explain the nonlinear modes in this case, we need to consider the ion heating in the nonlinear regime. We therefore fit a Maxwellian function to the ion VDF in one of the time windows, and find $v_{ti} = 2.4\, c_s$ for use in Eq. (4.8) (Fig. 4.12). We note that it is important to have the most accurate fit in the region of the phase velocity of propagating waves. Therefore, in calculating the fit residual, we have given a special weight to the points around that region ($v_x \approx \pm 10\ c_s$ in Fig. 4.12). The electron VDF is also fit in two time windows (Figs. 4.13b and 4.13c). Like before, the parameters found by these fits are substituted in Eq. (4.8), and this equation is solved to find the theoretical spectrum of the eigenmodes.

In the spectrum of the nonlinear waves, we see that the frequencies of the dominant modes (and therefore their phase velocities) are generally higher than the case of $v_0 = 4\, v_{te}$ (compare Fig. 4.10 with Fig. 4.14). This feature is well captured by the theoretical model (compare Fig. 4.11 with Fig. 4.15). Another difference between this case and that of $v_0 = 4v_{te}$ is the shorter range of the spectrum in the k values. In the current case, we see that the modes with $|k| \gtrsim 0.2$ (as in contrast to $|k| \gtrsim 0.4$) are faint. This is consistent with the linear theory, which also shows a shorter unstable spectrum for the case of $v_0 = 10v_{te}$ (Figs. 4.2a and 4.2b). Like before, we see that the high-frequency modes fade away from the spectrum as time passes (see Fig. 4.14b); this observation can be explained by the theoretical growth rates being negative in each time window (Fig. 4.15a, Fig. 4.15b).

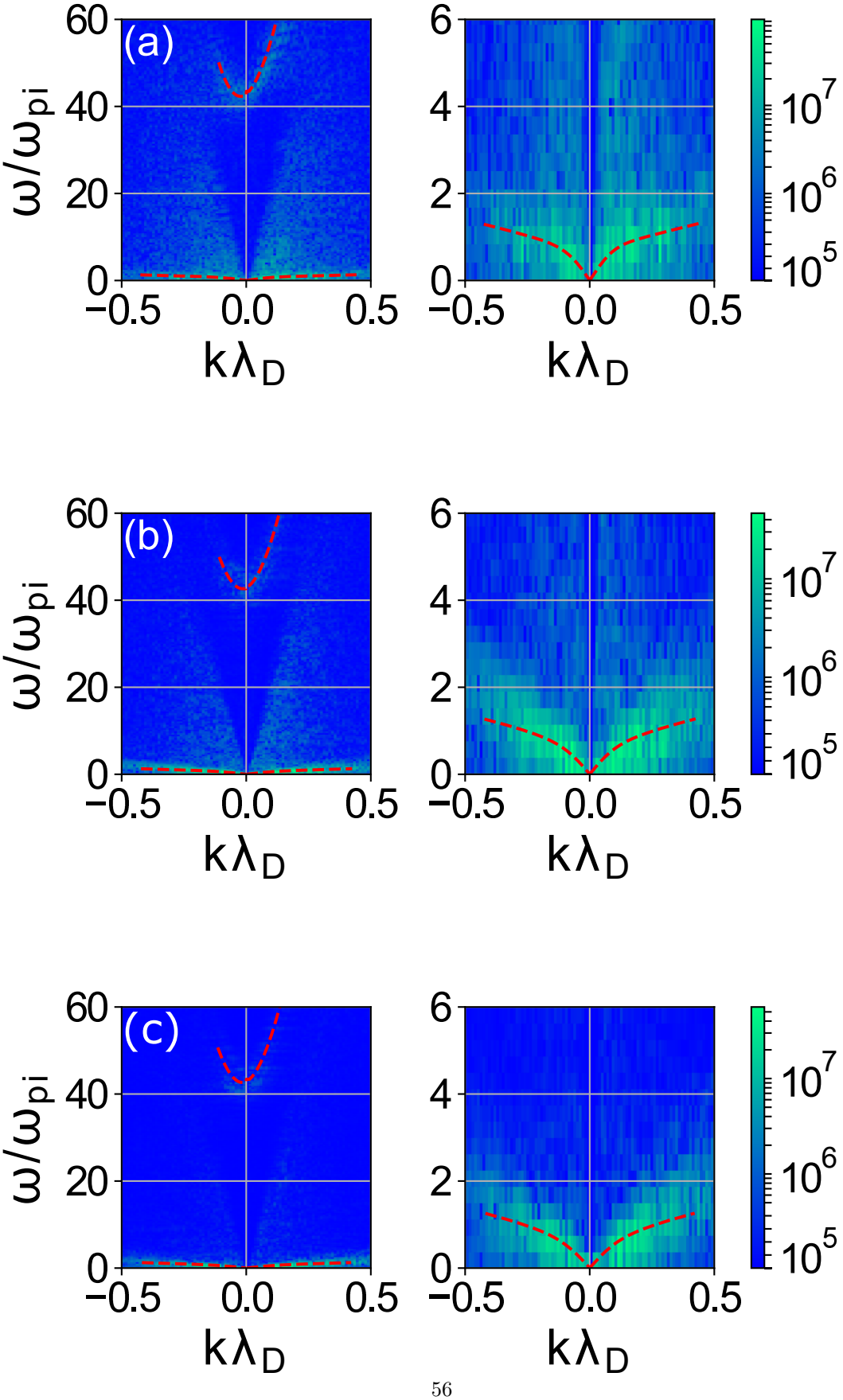
(a)
(b)
(c)
ω/ω_pi
kλ_D
60
40
20
0
6
4
2
−0.5
0.0
0.5
10^7
10^6
10^5

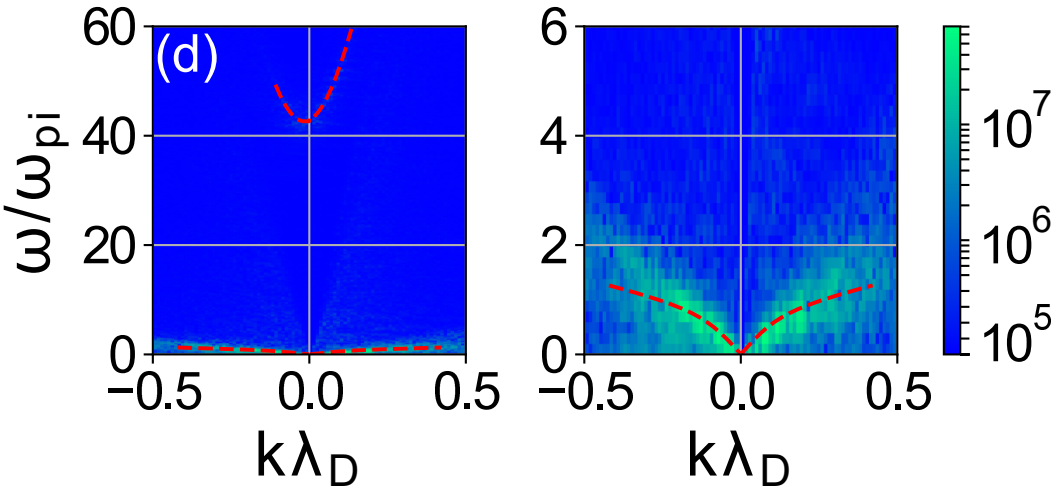

Figure 4.10: The spectrum of nonlinear waves in the case of $v_0 = 4v_{te}$, for (a) $19.8\,\omega_{pi}^{-1}$ to $34.8\,\omega_{pi}^{-1}$, (b) $34.8\,\omega_{pi}^{-1}$ to $51.4\,\omega_{pi}^{-1}$, (c) $51.4\,\omega_{pi}^{-1}$ to $68.2\,\omega_{pi}^{-1}$, (d) $68.2\,\omega_{pi}^{-1}$ to $100\,\omega_{pi}^{-1}$. In each case, a zoom into the low-frequency region is shown on the right of the full spectrum. The red lines show the modes found by solving Eq. (4.8) [The data used for the production of the red lines are produced by Mina Papahn Zadeh].

4.7 Drift velocity threshold for the appearance of backward waves

The backward waves do not appear if the drift velocity is below of some finite threshold v_{tr}. In order to narrow the down the threshold value, we compare two simulations with $v_0 = 1.5v_{te}$ and $v_0 = 1.75v_{te}$. In both cases, all other parameters are unchanged. We show that the backward waves are not present in the former case, whereas they are present in the latter. Therefore, v_{tr} is somewhere between these two values. Figs. 4.16a and 4.16b show the electric field energy for the cases of $v_0 = 1.5v_{te}$ and $v_0 = 1.75v_{te}$. By comparing these figures with Fig. 4.3a and Fig. 4.4a, we see that by increasing v_0 from $1.5v_{te}$ to $10v_{te}$, the saturation energy increases [87, 16]. However, because the linear growth rate also increases with v_0, the nonlinear regime is reached sooner.

Fig. 4.17a shows the electric field evolution in the case of $v_0 = 1.5v_{te}$. We see that, in this case, no backward waves appear, even deep in the nonlinear regime. However, in the case of $v_0 = 1.75v_{te}$ (Fig. 4.17b) after about 600 ns, lines of negative slope appear, indicating the presence of backward waves. The explanation can again be given according to the linear theory of Landau damping using the nonlinear electron VDF. The electron VDF for the case $v_0 = 1.5v_{te}$ after equilibrium, (Fig. 4.18a), shows a plateau in the positive velocity region up to about $v_x = 20\ c_s$. However, in the negative velocities, despite some nonlinear modifications, the gradient remains mainly positive. In fact, the trapping in this case is not strong enough to extend the plateau

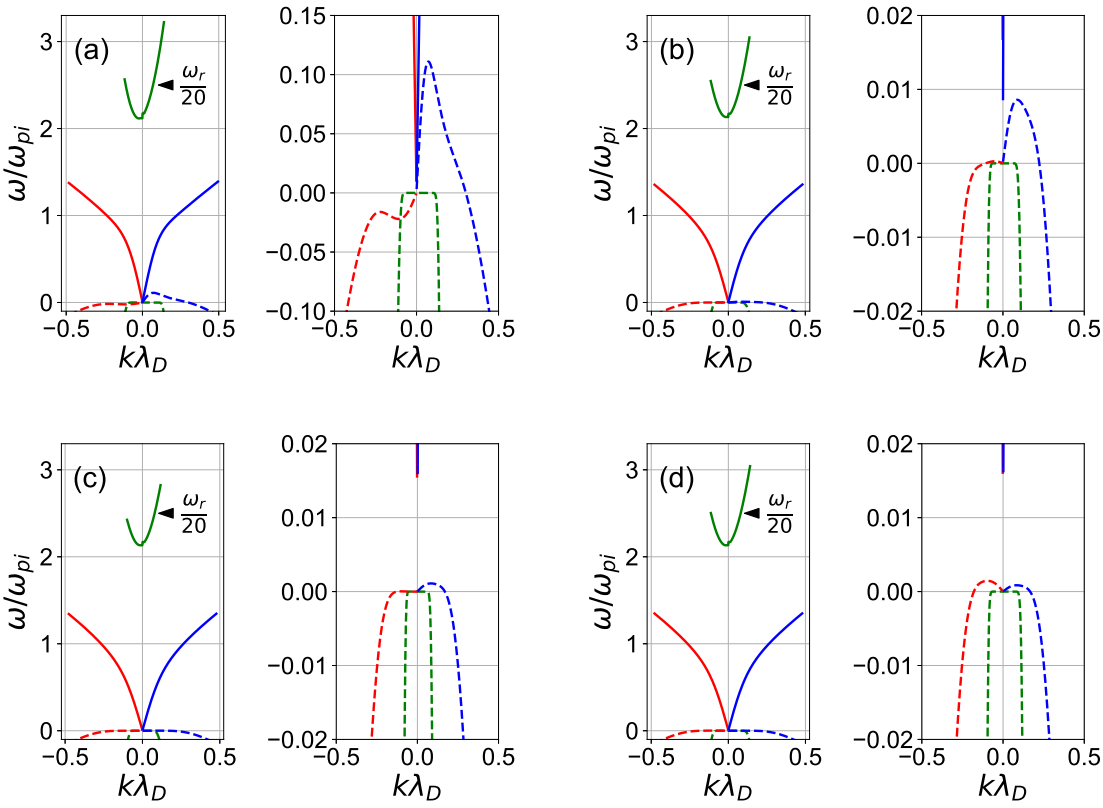

Figure 4.11: The theoretical frequencies (solid lines) and the growth rates (dashed lines) for the case of $v_0 = 4v_{te}$ shown in four stages. (a) $19.8\,\omega_{pi}^{-1}$ to $34.8\,\omega_{pi}^{-1}$, (b) $34.8\,\omega_{pi}^{-1}$ to $51.4\,\omega_{pi}^{-1}$, (c) $51.4\,\omega_{pi}^{-1}$ to $68.2\,\omega_{pi}^{-1}$, and (d) $68.2\,\omega_{pi}^{-1}$ to $100\,\omega_{pi}^{-1}$. These results are found by solving Eq. (4.8). The modes with growth rates less than $-0.1\omega_{pi}$ are omitted. The real and imaginary parts of a complex root are shown with the same color [The data used for the production of this figure are produced by Mina Papahn Zadeh].

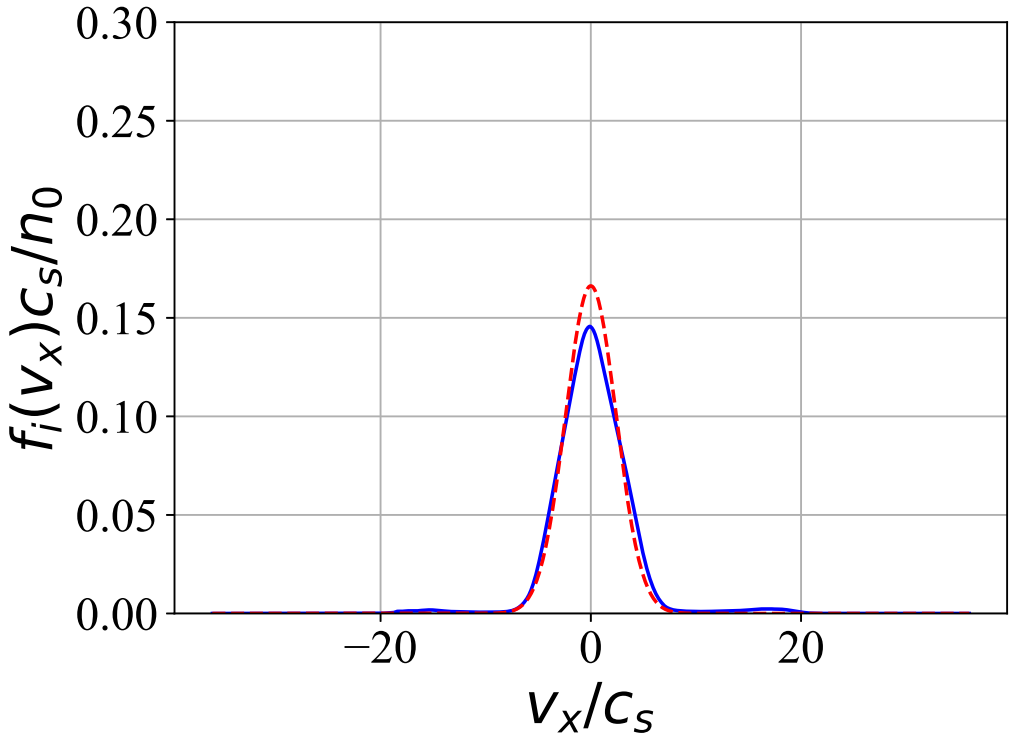

Figure 4.12: Ion distribution function for the case $v_0 = 10\, v_{te}$, averaged in $31.4\, \omega_{pi}^{-1}$ to $46\, \omega_{pi}^{-1}$ (solid blue line) shown together with the fitted Maxwellian (dashed red line).

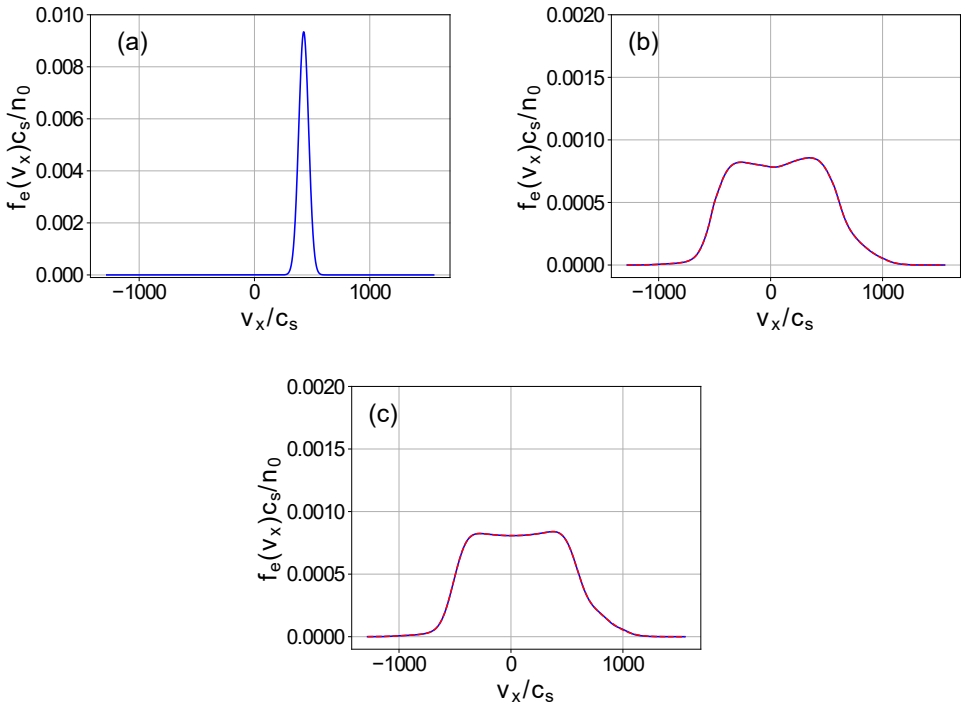

Figure 4.13: Evolution of the electron VDF for $v_0 = 10\,v_{te}$. (a) the initial VDF at $t = 0$ (b) VDF from nonlinear simulations (blue line) averaged over $t = 16.8\,\omega_{pi}^{-1}$ to $31.4\,\omega_{pi}^{-1}$ (c) $t = 31.4\,\omega_{pi}^{-1}$ to $46\,\omega_{pi}^{-1}$. The fit from Eq. (4.7) is shown in red in (b) and (c).

to the negative velocity region. Therefore, the absence of the plateau leads to the lack of the backward waves in this case. In contrast, the plateau of the case $v_0 = 1.75v_{te}$ (Fig. 4.18b) is extended well into the region of negative velocities, and therefore, the marginally stable backward waves appear in this case. The absence of backward waves in the case of $v_0 = 1.5v_{te}$ and their excitation in the case of $v_0 = 1.75v_{te}$ can also be seen in the Fourier spectrum (Figs. 4.19a and 4.19b). We note that the time intervals of these spectra correspond to the end of the simulation, and therefore, the high-frequency modes have already disappeared, as in the previous cases.

The minimum required drift velocity for the excitation of backward waves found in our simulations with hydrogen $v_0 \sim 1.5v_{te} - 1.75v_{te}$ is above the linear instability criteria $v_0 > 1.3v_{te}$ for $T_i = T_e$ [109]. In Ref. [16], the threshold $v_0 = 1.3v_{te}$ for the excitation of backward waves in plasmas with $T_e \gg T_i$ and heavier ions was reported. We note, however, that the linear instability threshold is a function of the mass and the temperature ratios, and it is greatly reduced for lower values of m_e/m_i and $T_i \gg T_e$ [109, 143, 144] For $T_e \gg T_i$, the linear instability becomes the ion-sound like one and has a much lower threshold $v_0 > \mathcal{O}(c_s)$ [144]. We have confirmed in additional simulations (not reported here) that the threshold for the generation of backward waves also decreases with an increase in ion mass and a decrease in ion temperature with respect to the electrons.

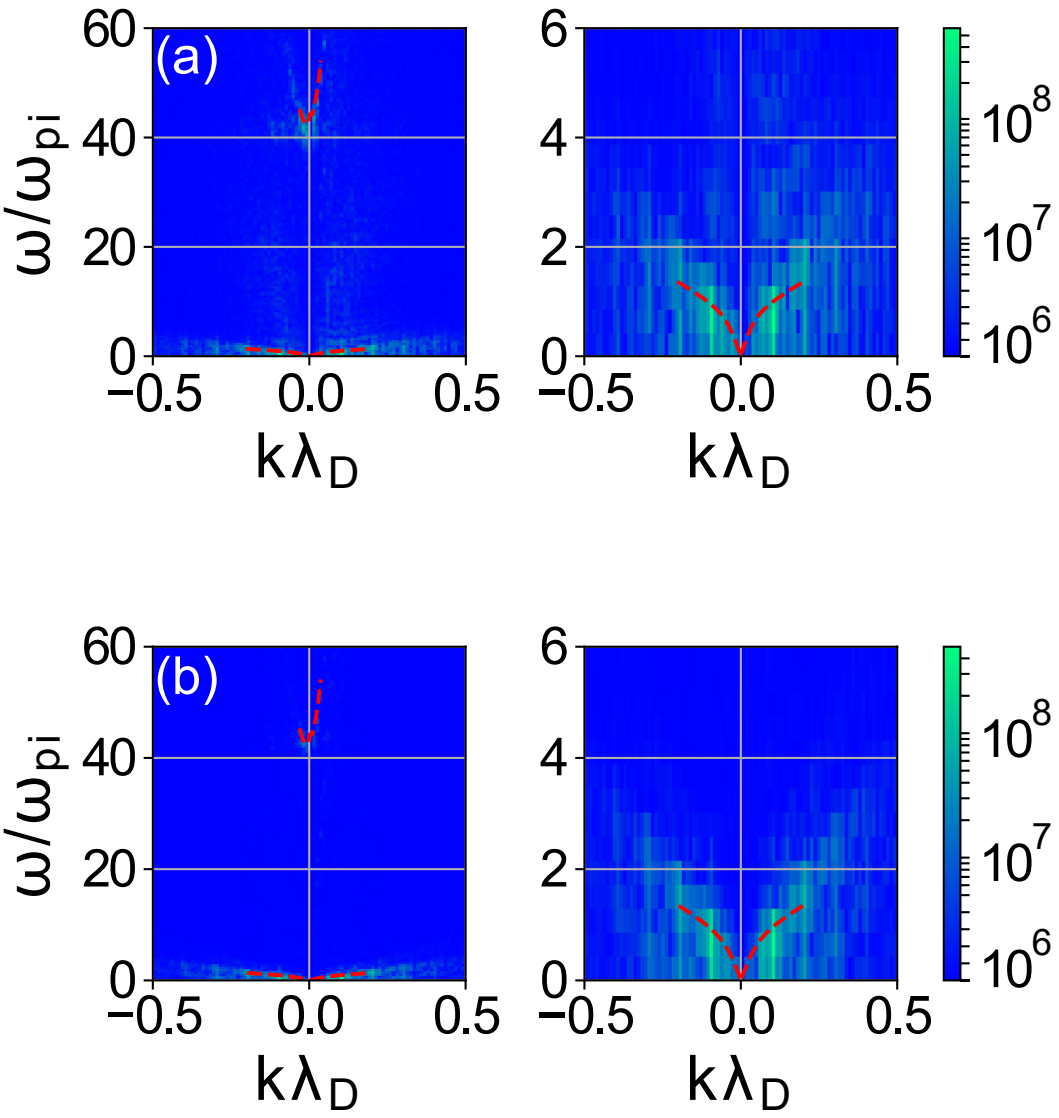

Figure 4.14: The spectrum of nonlinear waves the case $v_0 = 10\, v_{te}$, for (a) $16.8\,\omega_{pi}^{-1}$ to $31.4\,\omega_{pi}^{-1}$ and (b) $31.4\,\omega_{pi}^{-1}$ to $46\,\omega_{pi}^{-1}$. The red lines show the modes found by solving Eq. (4.8). In each case, a zoom into the low-frequency region is shown on the right of the full spectrum [The data used for the production of the red lines are produced by Mina Papahn Zadeh].

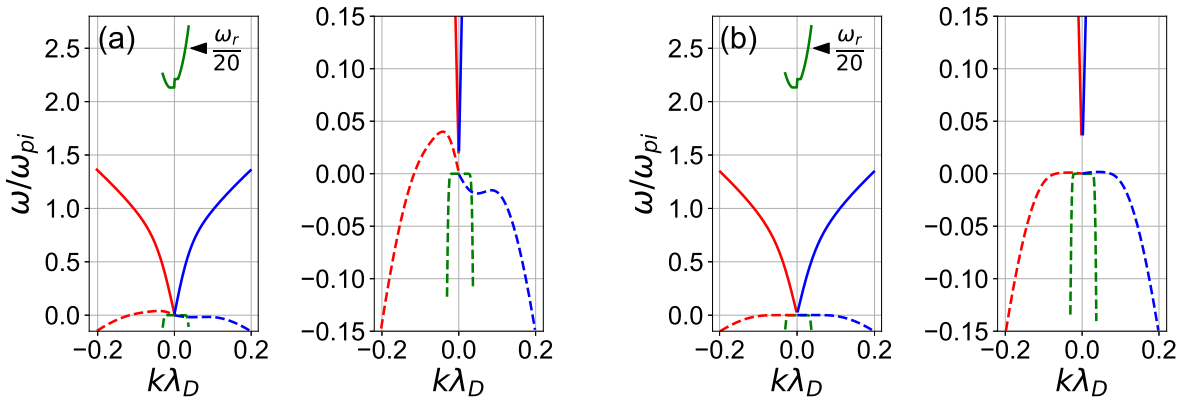

Figure 4.15: The theoretical frequencies (solid lines) and the growth rates (dashed lines) in two stages for the case $v_0 = 10\, v_{te}$. (a) $16.8\,\omega_{pi}^{-1}$ to $31.4\,\omega_{pi}^{-1}$ and (b) $31.4\,\omega_{pi}^{-1}$ to $46\,\omega_{pi}^{-1}$. These results are found by solving Eq. (4.8). The modes with growth rates less than $-0.15\omega_{pi}$ are omitted. The real and imaginary parts corresponding to a given complex root are shown with the same color [The data used for the production of this figure are produced by Mina Papahn Zadeh].

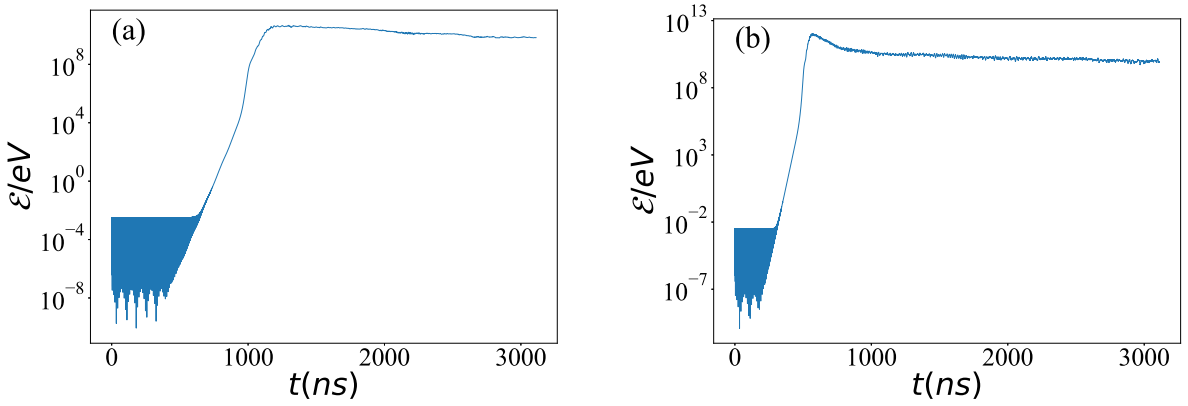

Figure 4.16: The electric field energy in two cases (a) $v_0 = 1.5 v_{te}$ and (b) $v_0 = 1.75 v_{te}$.

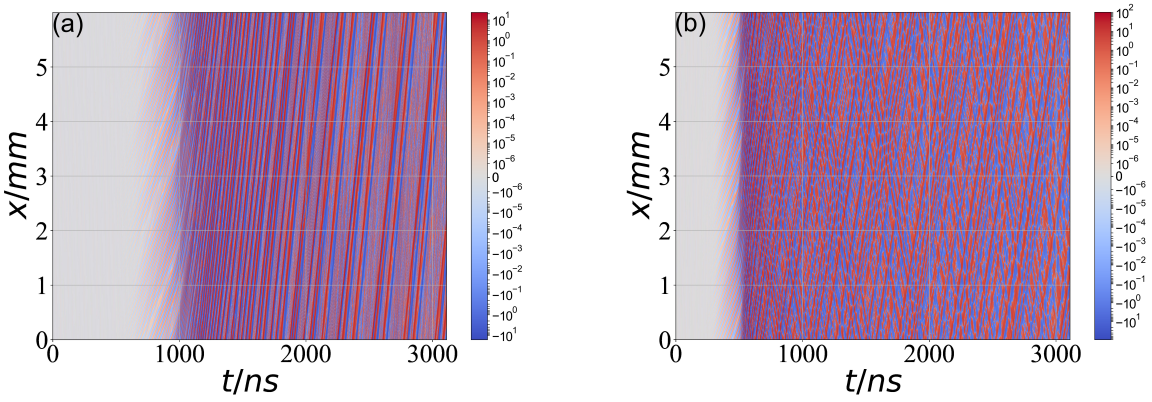

Figure 4.17: The electric field as a function of time and position in the cases of (a) $v_0 = 1.5v_{te}$ and (b) $v_0 = 1.75v_{te}$.

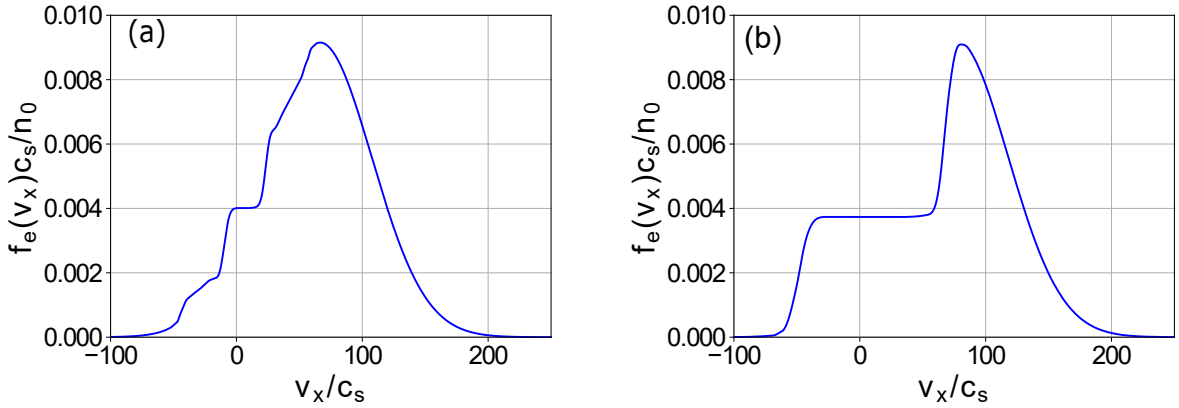

Figure 4.18: The electron VDF at time 2872 ns in the cases of (a) $v_0 = 1.5v_{te}$ and (b) $v_0 = 1.75v_{te}$.

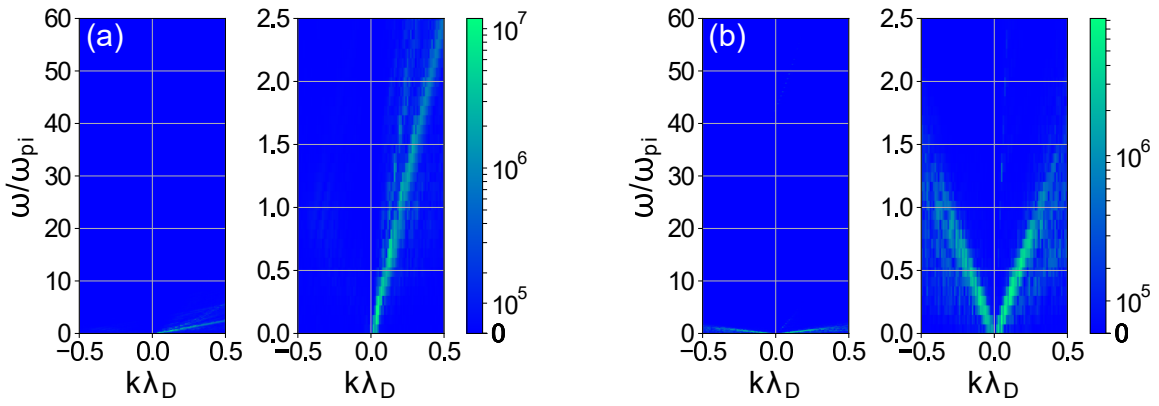

Figure 4.19: The Fourier modes between 2800 ns to 3000 ns in the cases of (a) $v_0 = 1.5v_{te}$ and (b) $v_0 = 1.75v_{te}$. In each case, a zoom into the low-frequency region is shown on the right of the full spectrum.

4.8 Summary and Discussion

In this work, we investigated the backward waves that are excited in the nonlinear regime of the Buneman instability. We have shown that the backward waves are excited if the value of the initial drift velocity exceeds a certain threshold, which was found in our simulations to be in the range between $v_0 = 1.5v_{te}$ to $v_0 = 1.75v_{te}$. Using the dispersion stability analysis, we have shown that characteristics of the backward and forward waves observed in nonlinear simulations can be explained, both in high-frequency and low-frequency regions, as marginally stable configurations of the nonlinear electron distribution function. We have found that an extended plateau in the region of the phase velocity of backward waves (in the region of the negative electron velocities) is necessary for the formation of the backward waves. This is further confirmed by the simulations with $v_0 = 1.5v_{te}$, where the absence of the plateau in the negative velocity region of electron VDF prevents the excitation of backward waves.

In a similar approach, the formation of a plateau in the ion VDF (in Ref. [139]) and the electron VDF (in Refs. [113, 130, 131]) has been found responsible for the new class of waves not expected from the linear theory due to finite Landau damping. In those studies, however, the modes were generally of smaller amplitude, and the contribution of the trapped particles was limited to a short range of velocities inside a narrow plateau in the VDF. In our simulations, the backward waves are generated simultaneously with formation of the electron beams in the negative direction due to electron reflections from large-amplitude potential structures as illustrated in Fig. 4.5b of the spatial potential profile. This process, starting with the electron trapping into the electron holes, proceeds via the growth of the potential fluctuations and further electron scattering (due to trapping and de-trapping). As a result of such scattering, the electrons are heated with the formation of the electron VDF with an extended plateau in the region of the negative velocities. The resulting potential

structures have large amplitudes, and the plateau in the electron VDF covers a significant region of the velocity range (i.e., many of the electrons are trapped). Our theoretical analysis shows that the nonlinearly modified distribution functions represent the marginally stable configuration from the perspective of linear stability.

In Ref. [16], the ion kinetic effects associated with ion heating and backward waves generated in the nonlinear regime of current-driven instabilities were studied, in particular, as relevant to the hollow-cathode discharges and cathode surface sputtering. We note that in our study, the ions are not heated for $v_0 = 4v_{te}$ and only weakly heated for $v_0 = 10v_{te}$. Backward waves have also been reported in the particle-in-cell simulation of the Buneman instability in Ref. [137]. Excitation of the backward waves was observed to co-exist with an enhanced anomalous resistivity in Ref. [30]. Similarly, backward waves were also suggested as the reason for an increase in the effective collision frequency seen in the simulation of Ref. [28]. In that work, it was conjectured that the underlying mechanism for the generation of the backward waves is the induced scattering off the ions. The resonant condition for the induced scattering from ions has the form $\omega(k_1) - \omega(k_2) \sim (k_1 - k_2)v_{ti}$. The low-frequency modes in our simulations show a symmetry between the forward and backward spectra (i.e., $\omega(k_1) \approx \omega(k_2)$ for these modes) and $k = k_1 = -k_2$. Moreover, for these low-frequency modes, one has $\omega(k_1) \approx \omega(k_2) \sim |kv_{ti}|$. This resonant condition is difficult to satisfy for the symmetric modes when $\omega(k_1) - \omega(k_2) \ll 2|kv_{ti}|$. Therefore, it is unlikely that in our case the induced scattering off the ions is responsible for the excitation of the symmetric spectra of low-frequency backward and forward waves. Based on nonlinear weak turbulence theory for the bump-on-tail instability, Ref. [138] attributes the high-frequency backward waves to the combined effect of three-wave decay and scattering off the ions and the low-frequency backward waves to merely the three-wave-decay process. However, the low-frequency modes in Ref. [138] are transient and decay to the level of noise later in the nonlinear regime. In Ref. [138], the formation of the plateau of the electron distribution function in the high-velocity region (of order v_{te}) is consistent with the observed high-frequency backward waves. As we have shown above in our simulations, the wide plateau extending into the negative region (and thus covering the low-velocity region) is responsible for the sustainment of the low-frequency ion-sound-like modes. The backward waves have been investigated in Vlasov simulations [136] for the case of $v_0 = 4v_{te}$. That study suggests the origin of the backward waves can be a secondary linear instability driven by bulks of counter-streaming electrons. However, the analysis was focused on the high-frequency modes, and the FFT in time was not long enough to clearly show the dominant low-frequency modes. The Buneman-type instability, excited by electron beams from solar nanoflares, was proposed as an underlying mechanism for the generation of turbulence in solar wind, plasma heating, and anomalous resistivity [27, 84, 28]. We show here that electron (plasma) heating and backward waves are closely related. It is also expected that anomalous resistivity is also affected. The effective heating of electrons observed in the regime $v_0 \geq v_{te}$ may be of interest for industrial applications of plasma-beam discharges. It has been suggested [16] that backward waves may be related to the hollow cathode erosion in Hall thruster due to the subsequent acceleration of the ions. This process was not considered in our study

but potentially may occur at a later stage and with a non-periodic setup when there is a constant energy input to the system. Intriguing experimental observations of the waves propagating against the direction of the electron beam were reported in Ref. [145]. No theoretical explanation has been proposed so far. It is possible that such waves are excited via the mechanism considered in our study.

Two-dimensional effects can be important and can modify the nonlinear dynamics of trapping and heating [110]. It is however expected that in applications to magnetized plasma, the transverse plasma motion is constrained by the magnetic field, whereas the dynamics along the magnetic field is expected to be well approximated by the one-dimensional model, as used in this study and other previous works [26, 29]. Our results show that the backward waves are related to particle trapping and are accompanied by the formation of the electron holes, which extend the plateau in the electron VDF to the negative velocity region. The dynamics and conditions of electron holes in multi-dimensional plasma is a multifaceted topic, where many questions remain open [110]. Some computational studies show that the stable electron holes do not appear in isotropic multi-dimensional plasmas [146, 147, 148, 110]. The reason is that the fraction of trapped particles is proportional to $\phi_0^{D/2}$, where ϕ_0 is the amplitude of potential and D is the number of spatial dimensions. Therefore for $D = 2$ or $D = 3$, the population of trapped particles may be too small to furnish stable electron holes [149]. However, strong magnetic fields can make the dynamics quasi-one-dimensional along the magnetic field, and stable electron holes can appear [146, 148]. In such a situation, the parallel electron VDF may form a plateau extending to the negative velocity region and leading to the onset of the backward waves as discussed above. The situation may become more complex when narrowly localized electron beams with a width of the order of the electron skin-depth across the magnetic field are involved, and two-dimensional effects may become essential, e.g., leading to the transverse ion heating Ref. [150]. Nevertheless, it is interesting to note, that even in this case, the two-dimensional simulations Ref. [150] demonstrate the electron heating and show the electron VDF extending to the negative velocity region, similar to the case considered here. The existence of backward waves in multi-dimensional situations requires additional analysis that is beyond the scope of this study. The electron trapping and hole formation may also be prevented by collisions when the collision frequency exceeds the characteristic bounce frequency for trapped electrons.

Acknowledgment

This work is partially supported in part by US Air Force Office of Scientific Research FA9550-15-1-0226, the Natural Sciences and Engineering Council of Canada (NSERC), and Compute Canada computational resources.

Data Availability Statement

The data that support the findings of this study are available from the corresponding author upon reasonable request.

5 The electron cyclotron drift instability: a comparison of particle-in-cell and continuum Vlasov simulations

5.1 Preface

Electron-cyclotron instability (ECDI) is a leading theory for explaining the anomalous mobility in the $E \times B$ plasmas. The broad implication of ECDI in plasma propulsion and space science has led to a great deal of interest in it, in recent years. The linear regime of this instability can be studied through the linear dispersion relation. For studying the nonlinear regime, numerical simulations are broadly used. This instability is characterized by its multi-dimensional nature in the phase space, very fast heating, and a complicated dispersion relation. These characteristics make an accurate simulation of this instability challenging. Most of the simulations of the ECDI are done by the PIC method. Here we present one of the first continuum Vlasov simulations of ECDI and compare it with the PIC results.

This chapter is based on a manuscript submitted to the Physics of Plasma journal. The author of this thesis (A. Tavassoli) is the first author of the submitted article and had the highest contribution among the co-authors of this article. This contribution is as follows.

- Leading the conceptualization, investigation, and formal analysis of the study.
- Managing comments, suggestions, and discussions of the co-authors and reflecting them in the text of the article.
- Organizing, writing, and preparing most of the text of the article throughout the preparation and submission processes.
- Having a dominant role in the development of the "semi-Lagrangian Vlasov" code used in this article.
- Running all the simulations that are referred to as "Vlasov simulation" in the article and producing the data for making the corresponding figures.
- Post-processing with Python and producing some figures of the article.
- Being the corresponding author of the article. All correspondence with the editorial office during the publication process was done through the corresponding author.

For clarifying the contribution of co-authors in producing figures, their names are printed in the caption of the figures.

5.2 Abstract

The linear and nonlinear characteristics of the electron cyclotron drift instability (ECDI) have been studied through the particle-in-cell (PIC) and continuum Vlasov simulation methods in connection with the effects of the azimuthal length (in the $E \times B$ direction) on the simulations. Simulation results for a long azimuthal length (17.82 cm = 627 v_d/ω_{ce}, where ω_{ce} is the electron cyclotron frequency and v_d is the $E \times B$ drift of the electrons) are reported, for which a high resolution is achieved in Fourier space. For simulations with a long azimuthal length, the linear growth rates of the PIC simulations show a considerable discrepancy with the theory, whereas the linear growth rate of the Vlasov simulations remains close to the theory. In the nonlinear regime, the inverse cascade is shown in both PIC and Vlasov simulations with a sufficiently large azimuthal length. In simulations with a short azimuthal length, however, the inverse cascade is barely observed. Instead, the PIC simulations with a short azimuthal length (0.5625 cm = 19.8 v_d/ω_{ce}) show an essentially continuous nonlinear dispersion, similar to what is predicted by the ion-sound turbulence theory. It is shown that, in the PIC and Vlasov simulations, the inverse cascade coincides with the formation and merging of electron structures in phase space. This process, however, terminates differently in the PIC simulations compared with the Vlasov simulations. Larger amplitudes of ECDI fluctuations are observed in the PIC simulations compared with the Vlasov simulations, leading to an intensified electron heating and anomalous current. This suggests that the statistical noise of PIC simulations might contribute to the extreme electron heating that has been observed in previous studies.

5.3 Introduction

In recent years, theoretical and experimental studies of the electron cyclotron drift instability (ECDI) have received considerable attention [151, 152, 153, 154, 155, 156, 11, 12, 157]. The ECDI is a leading candidate to explain fluctuations that increase the electron conductivity across the magnetic field, well above the predictions of the collisional transport theory, in particular, for Hall thrusters, where the electron anomalous current strongly affects the discharge and thrust characteristics [6]. A similar instability occurs in space plasma conditions [24, 25]. Therefore, understanding the mechanism of the instability and the related anomalous current due to ECDI is important for the operation of Hall thrusters and space physics.

The linear regime of the ECDI is well studied from the dispersion equation [38]. The linear spectrum of unstable ECDI modes for purely perpendicular propagation is characterized by discrete and sharp bands of the growth rate that result from the interaction of the ion mode with the Doppler-shifted electron cyclotron resonances [21]. When the wave vector along the magnetic field is finite, the linear spectrum of the ECDI becomes smoother and approaches the spectrum of unmagnetized ion-sound instability [39, 12]. It has been argued [8, 13] that even for propagation purely perpendicular to the magnetic field, the ECDI can be described as the ion-sound instability. It has been suggested [20, 21] that the nonlinear transition to the ion-sound

regime for perpendicular propagation may occur similarly to the transition from discrete Bernstein modes with a finite magnetic field to the Landau damped modes in the limit of the vanishing magnetic field, $B \to 0$, Bernstein–Landau paradox [158]. Such a transition has been debated, however, in other studies, where the effects of the magnetic field have been emphasized [23, 11, 12, 157].

Numerical simulations have been making major contributions to the understanding of the ECDI in the nonlinear regimes. The nonlinear anomalous current as a result of the ECDI has been demonstrated in many numerical simulations [10, 11, 12, 157, 8, 9, 13, 80, 79, 159, 160]. In the simulations, the anomalous current is often accompanied by fast electron heating [11, 8]. The origin of this heating is not well understood, but Refs. [10, 14, 161] suggest it is the result of stochastization of electron trajectories [162, 163, 164]. Nevertheless, the heating rates in the PIC simulations of Refs. [11, 12, 8] exceed experimentally observed values[161]. Another characteristic of the ECDI demonstrated by simulations is the flow of energy from the short-wavelength modes to the long-wavelength modes in the nonlinear regime (the inverse cascade) [11, 157], which is believed to have an important role in the generation of the anomalous current.

Despite many insights provided by numerical simulations, there are still many challenges to be addressed. Most simulations of the ECDI are done using the particle-in-cell (PIC) method, which is known to suffer from statistical noise. This noise is a result of the limited number of markers (macroparticles) that are used to sample the phase space, and it only decreases as $1/\sqrt{N_{ppc}}$, where N_{ppc} is the number of macroparticles per cell. It is well known that the noise of PIC simulations can undermine the accuracy of physical results such as the linear growth rates [60], heating and transport rates [69, 70], and the threshold of instabilities [71]. The noise can also lead to a "numerical relaxation" towards Maxwellian distributions in PIC simulations [41, 72]. This effect can potentially introduce numerical transport in the simulations, thus distorting the physics. The effect of the N_{ppc} on the ion density, electric field, and anomalous current has been investigated in the 2D ECDI simulations of Refs. [80, 79]. In both studies, it is concluded that numerical convergence happens at $N_{ppc} \approx 100 - 250$. In the 1D PIC simulations of Ref. [8], however, it is found that neither increasing N_{ppc} nor using the "quiet start" initialization have a significant effect on the anomalous mobility in ECDI.

Another challenge for the simulation of ECDI is related to the effects of the simulation box length on the physics of the linear and nonlinear regimes. The limited length in the direction of the $E \times B$ drift (the azimuthal length) results in the discrete spectrum of the modes that can be excited; i.e., only the modes with an azimuthal wave vector $k_x = 2\pi m/L$ (where L is the azimuthal length and $m = 1, 2, \ldots$) are permitted in the simulation. In this work, we refer to these modes as "box resonant modes" or simply "resonant modes".

Because of the computational costs, many studies use a relatively short azimuthal length of about 0.5 cm to 2 cm [79, 80, 165, 13, 166, 12]. By increasing L, the number of box resonant modes, and therefore the resolution of the simulation in Fourier space, increases. In the linear regime of ECDI simulations, resolving the steep variation of the growth rates in Fourier space demands a particularly high resolution in this space (see e.g., Fig. 5.1a). Also in the nonlinear regime, the generation of the long-wavelength waves due to inverse cascade can be affected by a limited azimuthal length. Previous studies of the ECDI have mainly relied on

convergence tests and benchmarking against other PIC codes for validating the results of the PIC simulations. Despite their merits, such an approach would not reveal any systematic problem that might be present in the PIC approach itself. Therefore, benchmarking against alternative kinetic simulation methods seems prudent. The continuum Vlasov is an alternative simulation method to the PIC method. The continuum Vlasov method is known to be free of statistical noise, and for this reason, benchmarking PIC results against Vlasov results is a potentially useful experiment for investigating the effect of noise in PIC simulations.

In Ref. [157], we presented one of the first Vlasov simulations of the ECDI. The results of these simulations demonstrated some of the characteristics of the ECDI such as nonlinear transitions in the fluctuation profiles, inverse cascade, nonlinear heating, and anomalous transport. It was also shown that the transition to ion-sound theory is not likely to exist in the nonlinear regime of the simulation. Some of the similarities and discrepancies between the PIC simulations with the Vlasov simulations were also discussed.

In this work, we present a detailed comparison between the PIC and Vlasov simulations of the ECDI, with special emphasis on the effect of azimuthal length. In the linear regime, we have measured the linear growth rates from simulations and compared them with the theoretical growth rates from the dispersion relation. It is shown that, for an intermediate length ($L = 156.8/k_0$, where $k_0 \equiv v_d/\omega_{ce}$, ω_{ce} is the electron cyclotron frequency and v_d is the $E \times B$ drift of the electrons) and as long as the N_{ppc} is sufficiently large, the linear growth rates in both the PIC and Vlasov simulations are fairly consistent with theory. This conclusion, however, does not hold for the simulations with a long azimuthal length ($L = 627/k_0$). For this length, many new resonant modes are resolved, some of which (especially the low-growth-rate modes) show a much better consistency with theory in the Vlasov simulation than the PIC simulation even with N_{ppc} as large as $N_{ppc} = 10^4$. In the nonlinear regime, the inverse cascade is shown in both PIC and Vlasov simulations for a sufficiently large L. For small L ($L = 19.8/k_0$), the inverse cascade is not clearly observed, and the spectrum of PIC simulation becomes mostly similar to the ion-sound turbulence theory of Ref. [21]. This similarity is not seen in the Vlasov simulation, likely because of the lack of the additional effect of the statistical noise. We also show that the inverse cascade coincides with the formation of some structures in the particular positions of the electron phase space. The subsequent merging of these structures is likely to explain the inverse cascade. Although this merging is observed in both PIC and Vlasov simulations, it terminates differently in them. The intensity of the nonlinear fluctuations in the PIC and Vlasov simulations is also compared. It is shown that the electrostatic energy, the electron temperature, and the anomalous current are generally larger in the PIC simulations than in the Vlasov simulations. The effect of the L on these quantities is also studied. It is shown that all these quantities increase with a significant increase in L. Moreover, a small variation of L can lead to a significant change in these quantities in the nonlinear regime, especially in the PIC simulations.

The remainder of the paper is organized as follows. In section 5.4, the physical and numerical setups of the ECDI problem are illustrated. In section 5.5, the linear regime of the ECDI is discussed, and the growth rates of the PIC and Vlasov simulations are compared. In section 5.6, the eigenspectra of the simulations are compared, and the inverse cascade is discussed. In section 5.7, the formation of the electron structures

and its possible relation to the inverse cascade are discussed. In section 5.8, the electrostatic energy and the electron temperature in the PIC and Vlasov simulations are compared. The effect of the azimuthal length on these results is also discussed. In section 5.9, the analysis is repeated for the anomalous current. Finally, in section 5.10, the results are discussed, and conclusions are given.

5.4 Problem setup and numerical methods

In our setup, a constant magnetic field (B_0) and a constant electric field (E_0) are applied in the direction of $\hat{y}$ and $\hat{z}$, respectively. Therefore, the $E \times B$ drift velocity of the electrons is $v_d = -\frac{E_0}{B_0}\hat{x}$. The ions are taken to be unmagnetized and unaffected by E_0, a common assumption in ECDI studies. Table 5.1 shows the parameters used in the simulations. We note that the values of the physical parameters are chosen as in Refs. [11, 12, 157]. These values are close to the typical operation regime of an SPT100 Hall thruster [6]. With these parameters, the Debye length is $\lambda_D \equiv \sqrt{\epsilon_0 T_{e0}/n_0 e^2} = 7.43 \times 10^{-3}$ cm, the electron thermal velocity is $v_{te} \equiv \sqrt{T_{e0}/m_e} = 1.329 \times 10^6$ m/s, the electron cyclotron frequency is $\omega_{ce} \equiv eB_0/m_e = 3.5$ rad/ns, and the electron Larmor radius is $\rho_e \equiv v_{te}/\omega_{ce} = 0.377$ mm. The initial condition for all simulations is a Maxwellian distribution, constructed using a random number generator in the PIC simulations. Due to the low level of noise in the Vlasov simulations, a perturbation is commonly used to excite the instability. In the Vlasov simulations, the initial density of electrons and ions is perturbed as $n_i = n_e = n_0(1 + \epsilon \sin \frac{2\pi}{L}x)$, where $\epsilon = 1.38 \times 10^{-4}$. We also tried a case where ϵ was 100 times larger ($\epsilon = 1.38 \times 10^{-2}$), and no significant change was observed in the results.

In all simulations, we have used a periodic boundary condition in the spatial subspace. The reason for this choice is to avoid any difficulty with regard to sheath formation at the boundaries and also to be consistent with the cylindrical geometry of the Hall thruster.[6]. In the Vlasov simulations, the boundary condition in the velocity subspace is open. We have used four lengths of the domain in the azimuthal direction: $L = 627/k_0 = 17.824$ cm, $L = 158.4/k_0 = 4.502$ cm, $L = 39.6/k_0 = 1.125$ cm, and $L = 19.8/k_0 = 0.5625$ cm. We note that azimuthal lengths $L = 39.6/k_0$ and $L = 19.8/k_0$ are not sufficient to properly capture the physics of the problem; however, we have confirmed that even for the smallest length L ($L = 19.8/k_0$), five cyclotron peaks are "resolved" (see Fig. 5.1a). Therefore, these two cases are shown as cases that might be tempting to use to reduce the computational cost of simulations while resolving the sharp cyclotron peaks of the ECDI but are in fact not well designed for investigating this problem.

The numerical method used for the Vlasov simulation is the semi-Lagrangian scheme [167]. In this method, the Vlasov equation is split into three sub-equations, which are then integrated using the method of characteristics with cubic spline interpolation [48, 49]. The three sub-equations are the advection equations in the x, v_x, and v_z directions, respectively. Because the ions are unmagnetized and unaffected by E_0, their advection equation in the v_z direction is trivial. In the Vlasov simulations, the Gauss law is solved, self-consistently, using the Fast Fourier transform (FFT). The PIC code used is "EDIPIC", which is also used in

Refs. [60, 11, 168]. The direct-implicit method is used for advancing the particles, and the finite difference method is used for solving the Poisson equation [94]. The numerical parameters used in the simulations are listed in Table 5.1. In the PIC simulations, we observed that if we use a time step the same as what is listed in table 5.1 for Vlasov simulations, the energy conservation is greatly violated. Therefore, the time step that is used for the PIC simulations is much smaller than the one used for the Vlasov simulations. On one hand, the requirement of a small time step for the PIC simulations might not be surprising. In the PIC simulations, it is generally recommended that the time step be small enough that a few particles are displaced more than a cell in one time step. On the other hand, in our PIC simulations, the extensive electron heating makes satisfying this criterion difficult (see e.g. Fig. 5.8b). This criterion does not however apply to the semi-Lagrangian Vlasov simulations. In all simulations, the energy was generally conserved to within 1 percent. In the Vlasov simulation with $L = 156.8/k_0$, time steps in the range of 5.6 ps to 11.2 ps were tried, and no significant change was observed in the results. For $L = 156.8/k_0$, the Vlasov simulation took about 10 days, and the PIC simulations with $N_{ppc} = 10^4$ took about 6 days, both on 32 processors. These times scale linearly with L. The convergence of the Vlasov simulations with respect to the resolution of the velocity grid is discussed in Appendix A.

Parameter	Value (s)	Related parameter
Magnetic field (B_0)	200 G	$\omega_{ce} = 3.52$ rad/ns
Electric field (E_0)	200 V/cm	$v_d = 10^6$ m/s
Ion mass (m_i)	131.293 u	
Electron temperature (T_{e0})	10 eV	$v_{te} = 1.33 \times 10^6$ m/s
Ion temperature (T_{i0})	0.2 eV	
Density (n_0)	10^{17} m^{-3}	$\lambda_D = 0.0743$ mm
PIC time step	0.56 ps $=0.01\ \omega_{pe}^{-1}$	$\omega_{pe} = 17.84$ rad/ns
Vlasov time step	5.6–11.2 ps $=0.1$–$0.2\ \omega_{pe}^{-1}$	
Spatial cell size	0.02 mm $=0.28\ \lambda_D$	
Electron velocity cell size (Vlasov)	7.14×10^4 m/s $=0.054\ v_{te}$	
Ion velocity cell size (Vlasov)	133 m/s$=10^{-4}\ v_{te}$	

Table 5.1: The parameters used in the simulations of ECDI.

5.5 Linear regime of ECDI and effect of azimuthal length on the linear growth rates of PIC and Vlasov simulations

The linear dispersion relation of the ECDI is $1 + \chi_i + \chi_e = 0$, where χ_i and χ_e are the ion and electron susceptibilities, respectively. The cold ion susceptibility is $\chi_i = -\frac{\omega_{pi}^2}{\omega^2}$, where $\omega_{pi} \equiv \sqrt{n_0 e^2/m_i \epsilon_0}$, n_0 is the plasma density, e is the electron charge, and m_i is the ion mass. The two-dimensional electron susceptibility is

$$\chi_e = \frac{1}{\lambda_D^2 k^2}\left[1 + \frac{(\omega - k_x v_d)e^{-\lambda}}{\sqrt{2}|k_y| v_{te}} \sum_{\ell=-\infty}^{\infty} I_\ell(\lambda) Z(\xi_\ell)\right], \tag{5.1}$$

where $k \equiv \sqrt{k_x^2 + k_y^2}$ is the magnitude of wave vector, I_ℓ is the Bessel function of the second kind of order ℓ, Z is the plasma dispersion function, $\lambda \equiv (k_x v_{te}/\omega_{ce})^2$, and $\xi_l \equiv (\omega - k_x v_d + l\omega_{ce})/\sqrt{2}|k_y| v_{te}$. In the ECDI, the overlapping resonances of Bernstein and ion-sound modes lead to a resonance condition

$$\omega - n\omega_{ce} - k_x v_d = 0, \tag{5.2}$$

where k_x is the wave vector in the direction of $E \times B$ drift, and n is an integer. When $\omega \approx 0$, the resonances occur at $k_x \approx nk_0$. In this study, we refer to these modes as "cyclotron peaks". For strictly perpendicular propagation ($k_y = 0$), the unstable growth rates form a set of discrete narrow-band modes near these peaks (see, e.g., Fig. 5.1a).

In this study, we solve the dispersion relation with a method described in Ref. [39]. As a test of the simulation results, we also measure the linear growth rates through simulations and compare them with the solution of the dispersion relation (the theoretical growth rates). For all azimuthal lengths, we ensured that at least five cyclotron peaks are resolved in the simulation. This point is made clear for $L = 19.8/k_0$ and $L = 156.8/k_0$ in Fig. 5.1a, where the resonant modes and their theoretical growth rates are shown. Figs. 5.1b and 5.1c shows the comparison of the theoretical growth rates and the growth rates measured with different simulation methods when the azimuthal length is $L = 156.8/k_0$. We can see that, for the PIC simulation with $N_{ppc} = 10^3$ or $N_{ppc} = 10^4$, and the Vlasov simulation, the measured growth rates decently agree with the theoretical values, despite a few outliers that exist in the three simulations. For the PIC simulation with $N_{ppc} = 10^2$, however, the growth rates can significantly deviate from the theory. This deviation increases with k and is particularly clear for higher cyclotron peaks such as $k \approx 4k_0$ and $k \approx 5k_0$. For these peaks, we basically see no growth rate in the PIC simulation with $N_{ppc} = 10^2$. The linear growth rates are measured from the data by fitting a line in the linear growth region, as for example can be seen clearly in Fig. 5.3b. However, in all of our PIC simulations, the linear growth is subject to numerical noise that causes spurious oscillations (see Fig. 5.3a). Therefore, the measurement of growth rates in PIC simulations is inevitably subject to errors that are much higher than those of the Vlasov simulations. The total electrostatic energy in the PIC and Vlasov simulations is also shown in Fig. 5.3c.

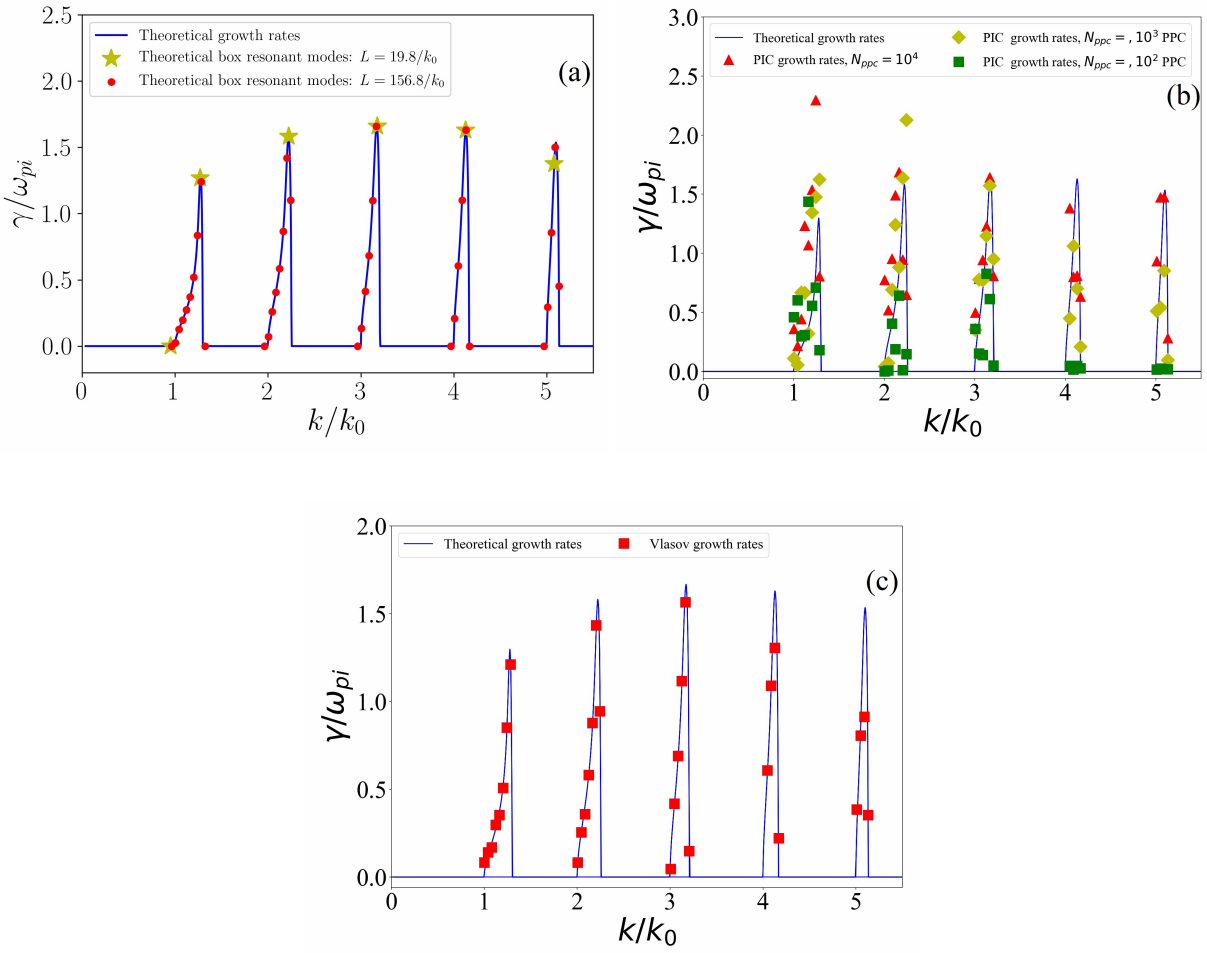

Figure 5.1: a) The box resonant modes for two different azimuthal lengths. b) The comparison of the measured and theoretical growth rates for PIC simulations; $L = 156.8/k_0$. c) The comparison of the measured and theoretical growth rates for the Vlasov simulation; $L = 156.8/k_0$ [The data used for the production of the PIC results are produced by Mina Papahn Zadeh].

Fig. 5.2b shows the theoretical and measured growth rates in a Vlasov simulation with azimuthal length $L = 627/k_0$. We see that, in comparison with the case of $L = 156.8/k_0$, many new resonant modes exist in the simulation. In the simulation with $L = 627/k_0$, the growth rates of the resonant modes of the $L = 156.8/k_0$ also show a better agreement with the theory. This effect is likely due to the reduced aliasing effects in the simulation with a longer azimuthal length. The results of the PIC simulation with $L = 627/k_0$ are also presented in Fig. 5.2a. Similar to the results of the Vlasov simulation, we see that many new resonant modes are captured by the simulation. However, the growth rates of some of the new resonant modes show a significant discrepancy with the theoretical results. This discrepancy is more noticeable for the low-growth-rate resonant modes, where the measured growth rates are much larger than the theory. These large growth rates are likely an effect of the PIC noise, as also shown in the study of the linear regime of the Buneman instability [60].

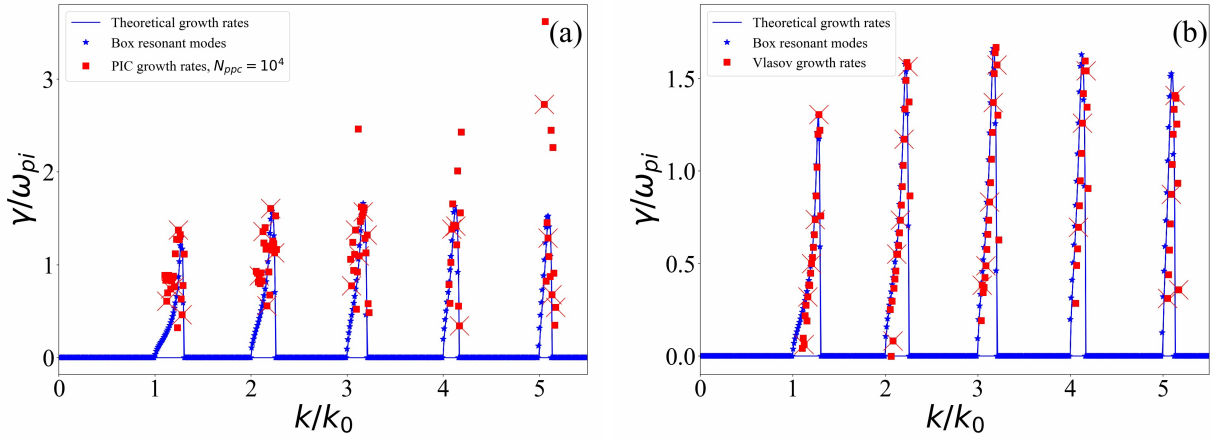

Figure 5.2: The growth-rates for a) PIC ($N_{ppc} = 10^4$) and b) Vlasov, both with $L = 627/k_0$. The $\times$ sign marks the box resonant modes of this simulation that also existed in the case of $L = 156.8/k_0$ cm [The data used for the production of the PIC results are produced by Mina Papahn Zadeh].

5.6 Nonlinear spectra, backward waves, and the role of the azimuthal length.

Fig. 5.4 shows the nonlinear spectrum of the electric field in the PIC and Vlasov simulations for different azimuthal lengths. In all cases, the amplitude of the high-intensity modes is much lower in the Vlasov simulations than in the PIC simulations. In the simulations with $L = 627/k_0$ and $L = 156.8/k_0$, we see that although the modes with $k \lesssim k_0$ do not grow significantly in the linear regime, they gradually grow in the nonlinear regime until a wavelength of about the size of the system appears. In this study, we refer to this process as the inverse cascade. This process happens along with the growth of other cyclotron peaks, especially between k_0 to $5k_0$. The inverse cascade is, however, less clear in the simulations with $L = 39.6/k_0$

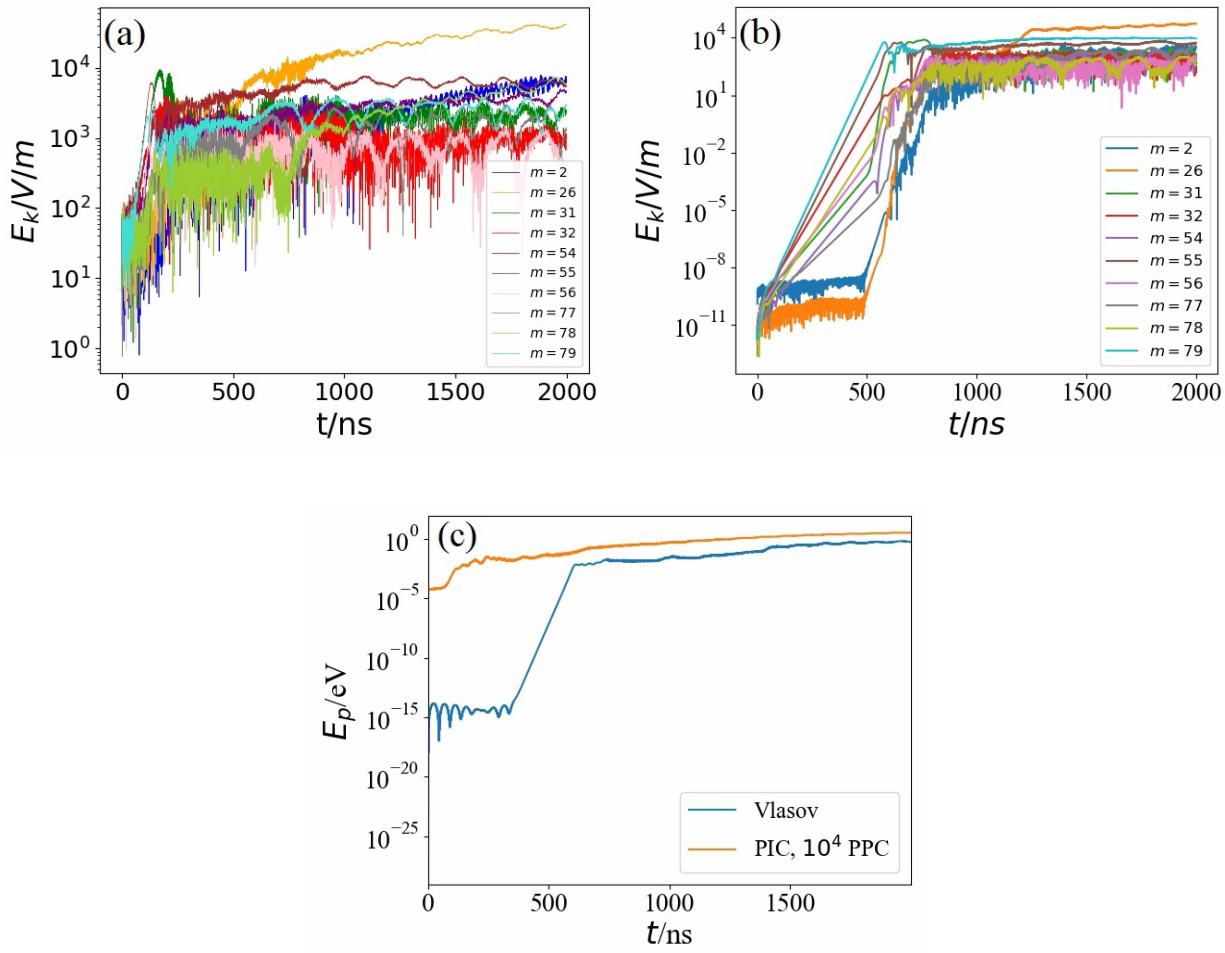

Figure 5.3: The growth of individual resonant modes of the electric field, using $L = 156.8/k_0$. a) PIC simulation ($N_{ppc} = 10^4$) and b) Vlasov simulation. The total electrostatic energies are shown in (c) [The data used for the production of the PIC results are produced by Mina Papahn Zadeh].

and is barely seen in the simulations with $L = 19.8/k_0$. In Figs. 5.4a to 5.4d, we can see that for $L = 156.8/k_0$ cm and $L = 627/k_0$, a mode with $k \approx k_0$ is eventually dominant in the late nonlinear regime. However, Figs. 5.4e and 5.4f show that this is not true when the azimuthal length decreases to $L = 39.6/k_0$ cm. In this case, a mode with $k \approx 2k_0$ in the PIC simulation and two modes with $k \approx 2k_0$ and $k \approx 0.5k_0$ in the Vlasov simulation have the highest amplitude at about $t = 2000$ ns. It is also seen that, although the discrete cyclotron peaks are still visible, there are also many finite-amplitude modes that fill the spaces between them. This suggests that decreasing the azimuthal length can make the Fourier spectrum smoother, similar to what is suggested in the theory of transition to ion-sound turbulence[20, 21]. The process of smoothing is even more clear in Figs. 5.4g and 5.4h, where the azimuthal length is reduced to $L = 19.8/k_0$ cm.

Fig. 5.5 shows the nonlinear frequency spectrum of the PIC and Vlasov simulations for different azimuthal lengths using the two-dimensional FFT. In all cases, the dominant frequency is around $\omega \approx \omega_{pi}$, which is consistent with the observations of Ref. [11]. Similar to Fig. 5.4, the dominant wave vector is around $k \approx k_0$ for $L = 627/k_0$ and $L = 156.8/k_0$, whereas it is around $k = 2k_0$ for $L = 39.6/k_0$. For all azimuthal lengths, the amplitude of the dominant mode is much higher in the PIC simulation than in the Vlasov simulation. An important difference between the frequency spectra of the PIC and Vlasov simulations is that the backward waves are clearly seen in the spectra of Vlasov simulations for all lengths. The backward waves propagate in the direction opposite to the initial electron drift and usually result from the strong flattening of the electron velocity distribution function [88]. Experimental observations also confirm the existence of these waves in the Hall thruster plasma [169, 170]. These waves are, however, barely noticeable in the spectra of the PIC simulations. The reason for this may be the low amplitude of backward waves makes them more susceptible to being lost in the noise of the PIC simulations. In Fig. 5.5, the ion-sound dispersion is also shown in all sub-figures. We can see that, in contrast to the ion-sound dispersion, in all simulations with $L \geq 39.6/k_0$, the frequency spectrum remains discrete. Nevertheless, in simulations with $L = 39.6/k_0$, some smoothing of the cyclotron peaks is observed. In Figs. 5.5g and 5.5h, the azimuthal length is further reduced to $L = 19.8/k_0$. In Fig. 5.5h, the mode $k \approx k_0$ has essentially disappeared, and mode $k \approx 2k_0$ is dominant. We note that the first three cyclotron peaks are still visible in Fig. 5.5h. Although the frequency spectrum of the Vlasov simulation remains quite discrete, the spectrum of the PIC simulation in Fig. 5.5g shows a significant smoothing and similarity with the ion-sound dispersion. Moreover, the dominant mode in this simulation has a $k \approx 1/(\sqrt{2}\lambda_D) \approx 2.7k_0$, which belongs to the maximum-growth-rate mode of the ion-sound instability. Therefore, it is likely that the combination of a small azimuthal length with the noise of the PIC simulations can induce the transition to ion-sound turbulence.

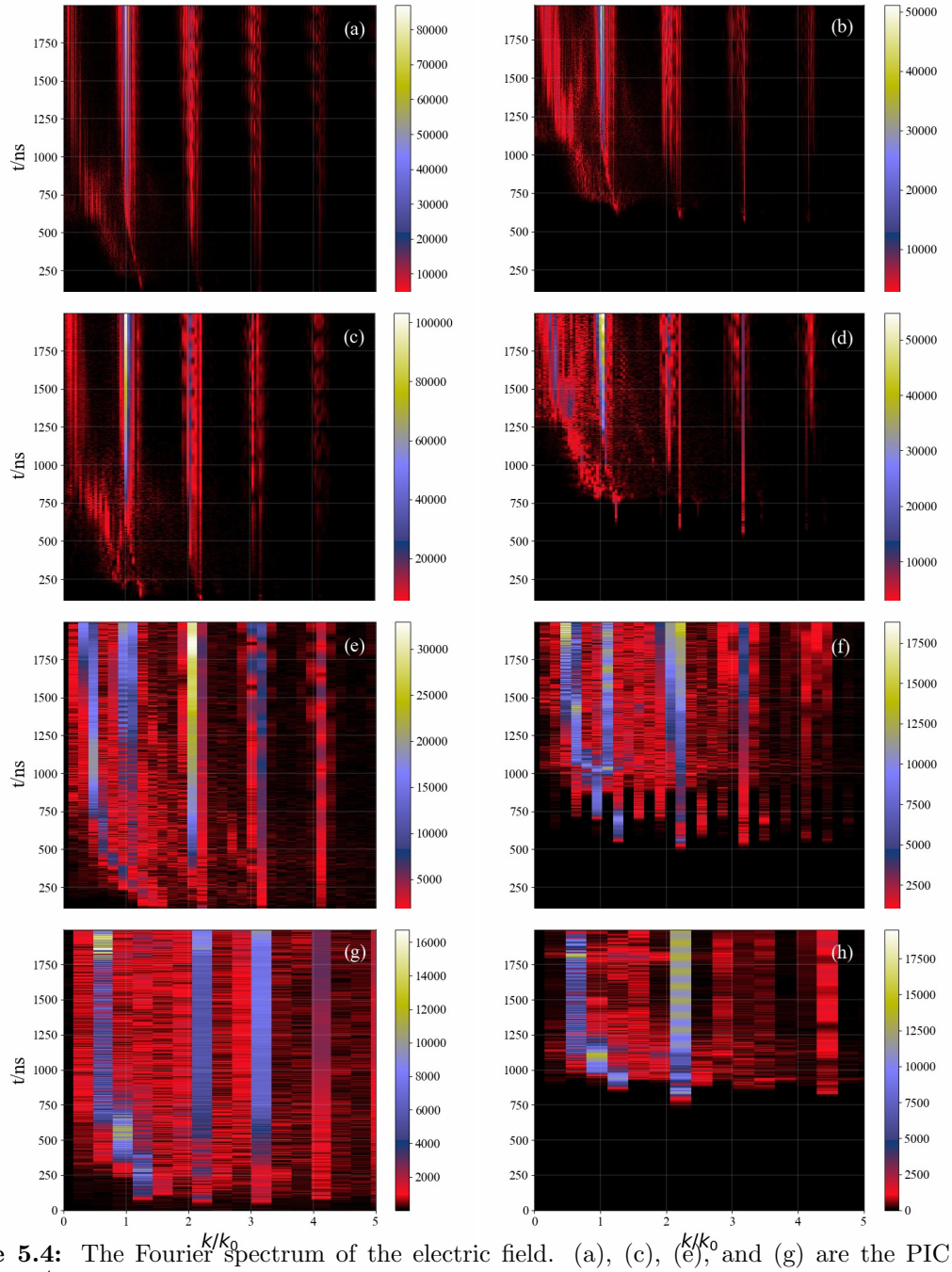

Figure 5.4: The Fourier spectrum of the electric field. (a), (c), (e), and (g) are the PIC results ($N_{ppc} = 10^4$). (b), (d), (f), and (h) are the Vlasov results. $L = 627/k_0$, $156.8/k_0$, $39.6/k_0$, and $19.8/k_0$ in the first, second, third, and fourth rows respectively [The data used for the production of the PIC results are produced by Mina Papahn Zadeh].

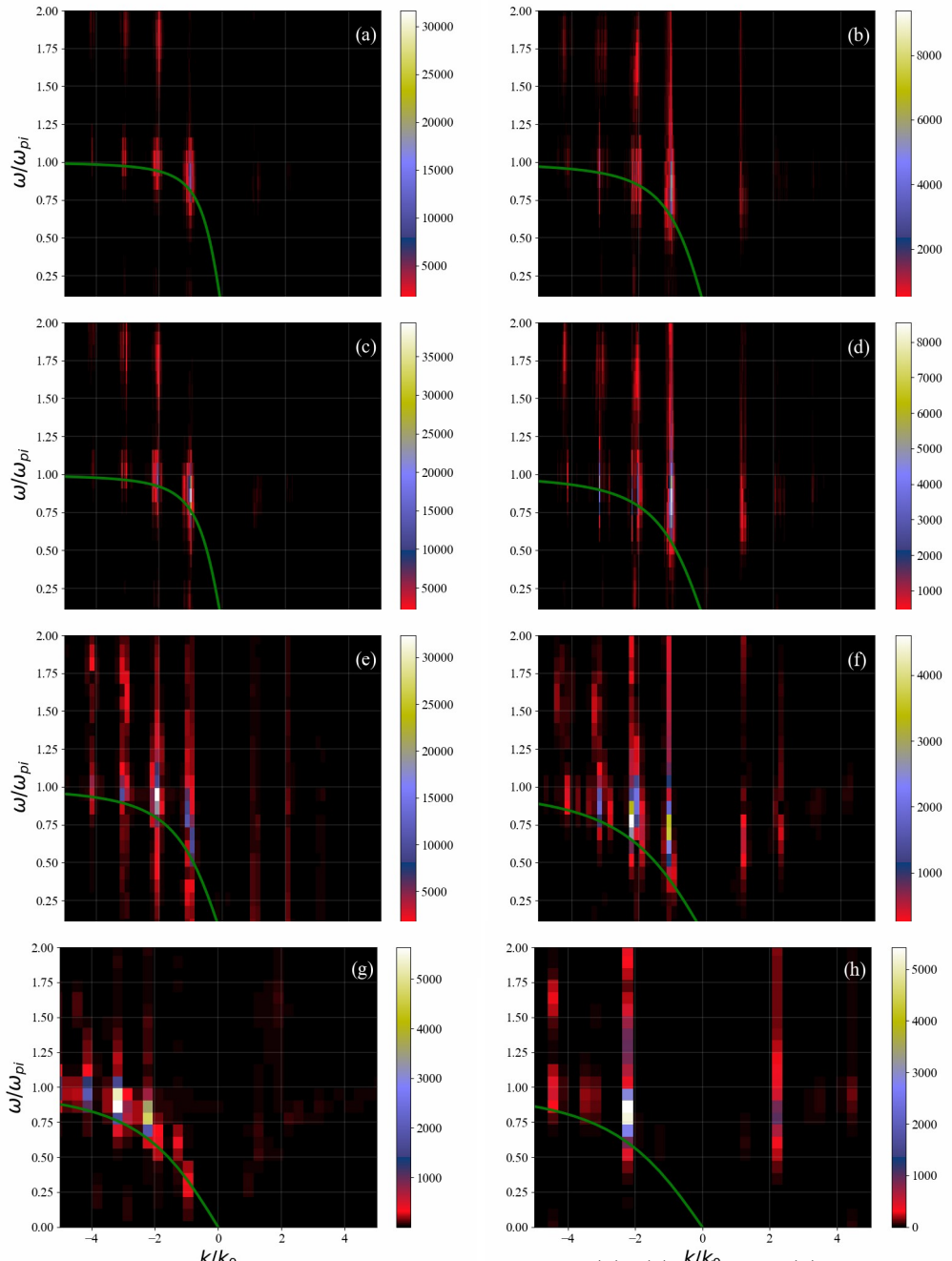

Figure 5.5: The frequency spectrum of the electric field. (a), (c), (e), and (g) are the PIC results ($N_{ppc} = 10^4$). (b), (d), (f), and (h) are the Vlasov results. $L = 627/k_0$, $156.8/k_0$, $39.6/k_0$, and $19.8/k_0$ in the first, second, third, and fourth rows respectively. Green lines show the ion-sound dispersion, calculated with the mean temperature of each simulation [The data used for the production of the PIC results are produced by Mina Papahn Zadeh].

5.7 The inverse cascade and phase space structures in the PIC and Vlasov simulations

Concentration of electrons in particular regions of the phase space form structures (bunches) that are seen in both PIC and Vlasov simulations. In the nonlinear regime of the ECDI, the electron bunches are likely the result of cnoidal waves that are formed in the nonlinear regime (see Refs. [11, 12, 157]). In contrast to electron holes, which are associated with local maxima of the electrostatic potential, bunches are associated with local minima. Fig. 5.6 shows the dynamics of electron bunches in the phase space of the PIC simulation. In Fig. 5.6a, we see that several electron bunches co-exist, and the electrostatic potential has a cnoidal wave shape at $t = 238$ ns. At time around $t = 797$ ns, some of these bunches merge, and larger bunches appear in the phase space (e.g., around $x \approx 10$ mm). The formation of larger bunches from the smaller ones coincides with the inverse cascade seen in Fig. 5.4c and therefore might explain this phenomenon. At $t = 1325$ ns (Fig. 5.6c), the process of merging has finished, and a "solitary" bunch is formed around $x = 5$ mm. Around this location, a clear global minimum in the shape of a soliton can be seen in the spectrum of electrostatic potential. The length of this soliton is about 8 mm, and after $t = 1325$ ns, it moves with an average velocity of about 26 $c_s \approx 7\ \omega_{pi}/k_0 \approx 0.06\ v_{te}$.

Similar to the PIC simulations, electron bunching is observed in the Vlasov simulations during the time that the inverse cascade in happening in Fig. 5.4d. Fig. 5.7a shows the electron phase space at $t = 768$ ns. At this time, many electron bunches are observed, some of which merge by $t = 1196$ ns (Fig. 5.7c). Fig. 5.7c shows that the process of bunching continues up to the last stage of the simulation. However, in contrast to the PIC simulation, no clear soliton is formed, and the wave has its cnoidal shape with several bunches until the last stage of the simulation. This discrepancy between the PIC and Vlasov simulations can be also explained based on the spectra in Fig. 5.4. In the k-spectrum of the PIC simulation in Fig. 5.4c, we can see a gap between $k \approx 0.2k_0$ to $k \approx 0.9k_0$ after $t \approx 1000$ ns. With no significant amplitudes in this gap, the small-k modes of the PIC spectrum become similar to the spectrum of solitary waves. In contrast, this gap is not observed in the spectrum of the corresponding Vlasov simulation (Fig. 5.4d).

5.8 The electrostatic energy and heating in PIC and Vlasov simulations

In our simulations, the electrostatic energy is calculated as $E_p = \frac{\epsilon_0}{2n_0 L}\int_0^L E_x^2 \mathrm{d}x$, and the (spatially averaged) temperature in the x-direction is calculated as $T_{xe} = \frac{m_e}{n_e L}\int_0^L \int (v_x - V_x)^2 f_e(x, v_x, v_z)\mathrm{d}v_x\mathrm{d}v_z\mathrm{d}x$. In all simulations, we observed that the temperatures in the x- and z-directions are basically the same, and therefore, we only report T_{xe}. Figs. 5.8a and 5.8b show the electrostatic energy and the temperature, respectively. In these figures, we do not use the logarithmic scale as in Figs. 5.3a to 5.3c in order to clearly show the differences

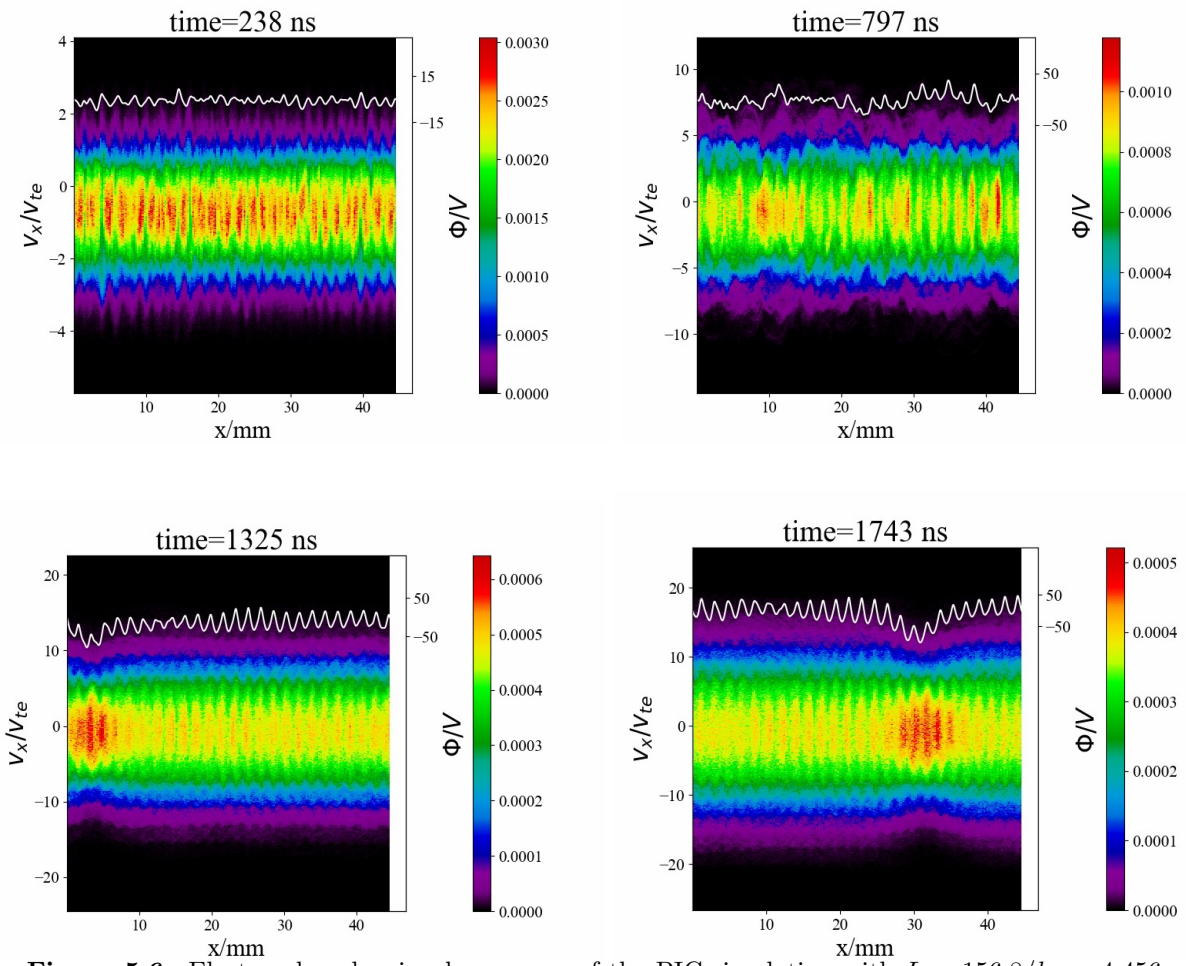

Figure 5.6: Electron bunches in phase space of the PIC simulation with $L = 156.8/k_0 = 4.456$ cm and $N_{ppc} = 10^4$. The white line shows the electrostatic potential (ϕ) [The data used for the production of the PIC results are produced by Mina Papahn Zadeh].

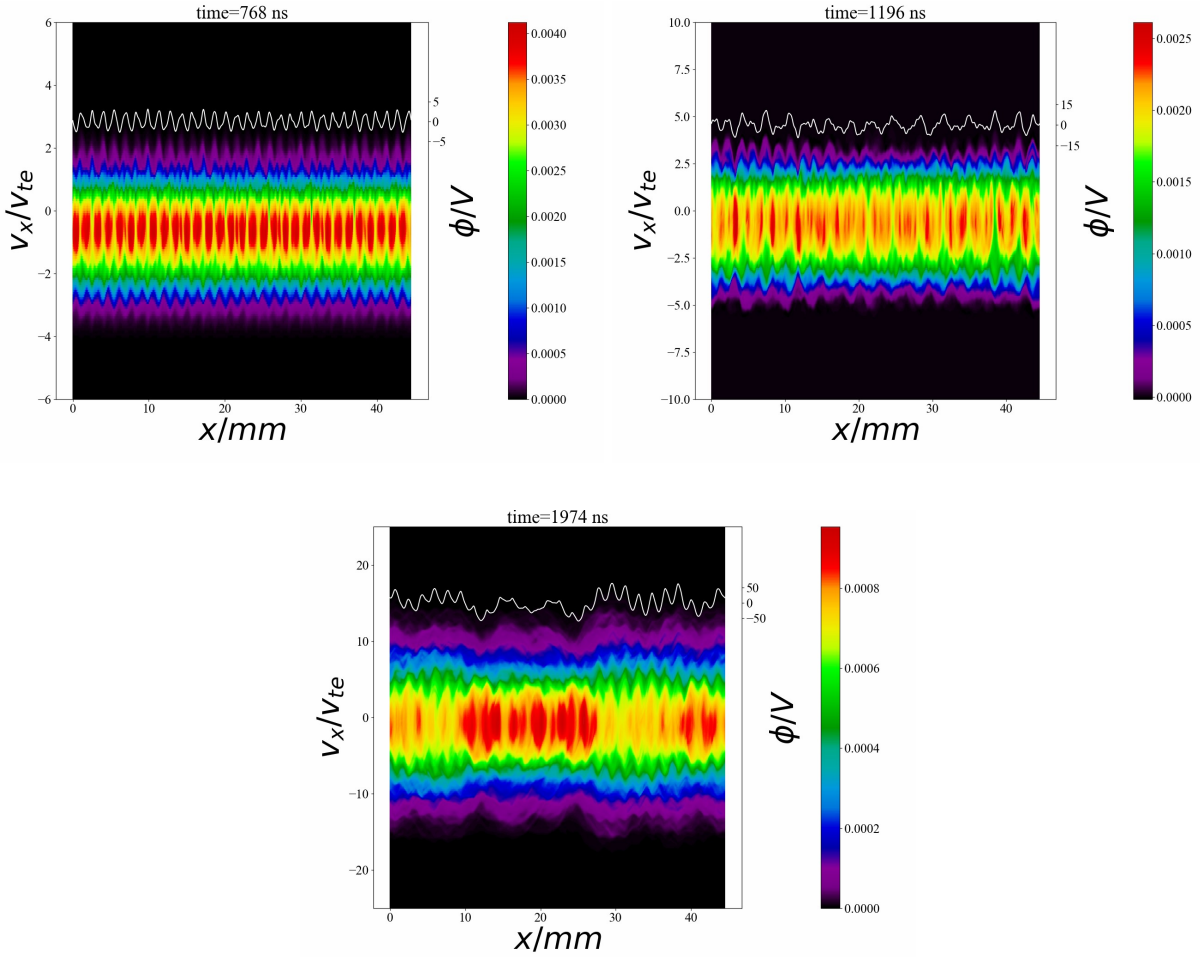

Figure 5.7: Electron bunches in phase space of the Vlasov simulation with $L = 156.8/k_0 = 4.456$ cm. The white line shows the electrostatic potential (ϕ).

in the nonlinear regime. In each figure, the results of the PIC simulations with different N_{ppc} are plotted along with the results of the Vlasov simulation. Figs. 5.8a and 5.8b show that in the linear regime and early nonlinear regime (up to $t \approx 600$ ns), the PIC and Vlasov results remain in good agreement. After this time, however, the electrostatic energy and the temperature in the Vlasov simulation are much smaller than in the PIC simulations even when $N_{ppc} = 10^4$. Because the Vlasov simulation starts from a much lower initial fluctuation amplitude, it does not go as far into the nonlinear regime as the PIC simulations. Therefore, to reduce confounds in the comparisons, we also plotted a "shifted Vlasov" in Figs. 5.8a and 5.8b. The shifted Vlasov is the same Vlasov simulation but with the time axis shifted by $t = 546.259$ ns. The size of this shift is the smallest required to make the initial electrostatic energy of the Vlasov the same as the PIC with $N_{ppc} = 10^4$. Therefore, the PIC and the shifted Vlasov start from the same level of fluctuation. Although this shift slightly raises the electrostatic energy and the temperature, they remain much less that in the PIC simulations for most of the nonlinear regime. We also tried the same shift on the PIC simulations with the higher N_{ppc} to make their initial amplitude similar to the ones with lower N_{ppc}; however, no significant change was observed in the results and hence are omitted.

In Figs. 5.8a and 5.8b, we also see that when N_{ppc} in the PIC simulation increases from 10^2 to 10^3, both electrostatic energy and electron temperature significantly decrease. When N_{ppc} increases further to 10^4, however, these quantities converge to approximately the same values. Another observation in Figs. 5.8a and 5.8b is that the rate of increase in the electron temperature closely tracks the electrostatic energy. This observation is at odds with the predictions of the ion-sound turbulence theory in Refs. [20, 21].

The effect of the azimuthal length on the electrostatic energy and temperature is shown in Fig. 5.9. We can see that both quantities increase with increasing azimuthal length in both PIC and Vlasov simulations. This can be partly due to the increase in the number of the unstable resonant modes in the simulations with longer azimuthal length (increased resolution in the Fourier space), as shown in Section 5.5, that leads to an increase in the total electrostatic energy. Another reason for this increase can be the further extension of the spectrum to long wavelengths that is made possible by increasing L. An important observation in Fig. 5.9 is the sensitivity of the heating and electrostatic energy to the azimuthal length. Figs. 5.9a and 5.9c show that, in the PIC simulation, a small variation of azimuthal length from $L = 156.8/k_0$ to $L = 158.4/k_0$ leads to a significant increase in electrostatic energy and electron temperature in the deep nonlinear regime. This sensitivity is, however, much less in the Vlasov simulations, as seen in Figs. 5.9b and 5.9d. In Fig. 5.9, we can also see that for all azimuthal lengths used, the electrostatic energy and electron heating in the PIC simulations are much greater than in the Vlasov simulations.

In Figs. 5.8 and 5.9, we see that neither the electrostatic energy nor the temperature completely saturate in the nonlinear regime. This observation is consistent with other PIC simulations of ECDI [11, 12, 8]. In Ref. [8], complete saturation is achieved due to the ion trapping only when the "virtual axial length model" is used. In this model, particles are replaced when they are displaced beyond a given length in the axial direction. In the absence of the virtual axial length model, the constant axial electric field provides an energy

reservoir for unlimited growth of the electrostatic energy and the temperature. The energy provided by this reservoir between the time 0 and t is

$$E_w = E_0 \int_0^t \int_0^L J_{ze}(x,t)\mathrm{d}x\mathrm{d}t, \tag{5.3}$$

where $J_{ze} = -e\int v_z f_e(x, v_x, v_z)\mathrm{d}v_x\mathrm{d}v_z$ is the axial electron current (the anomalous current). E_w is essentially wasted in the Hall thrusters because it does not contribute to the produced thrust. E_w is shown in Fig. 5.8c for the PIC and Vlasov simulations. We see that in all simulations the E_w remains relatively close to the electron temperature. This is in fact expected from the conservation of energy because, in the deep nonlinear regime, the electron heating is the dominant energy output of the system and E_w is the only energy input.

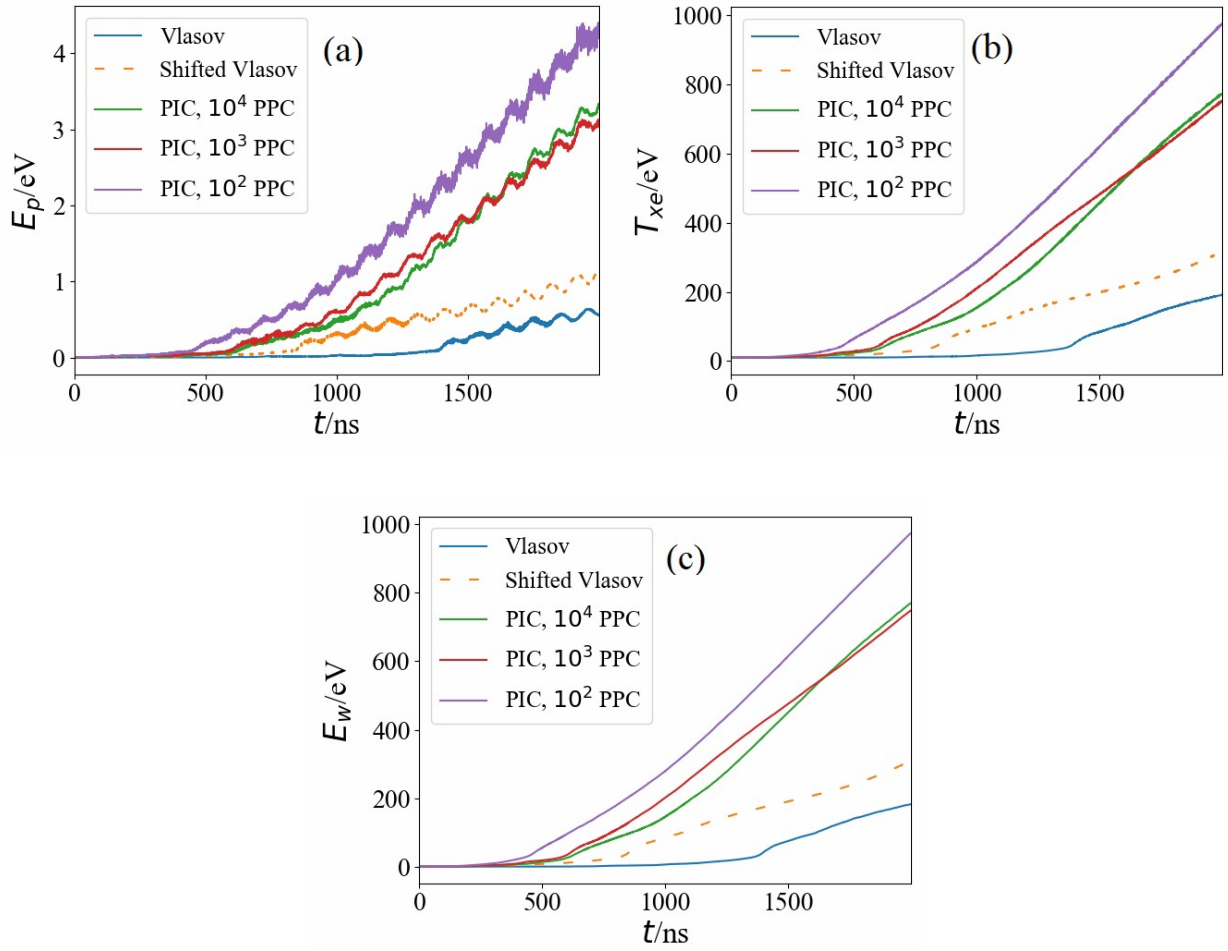

Figure 5.8: a) The electrostatic energy b) The electron temperature c) E_w as defined by Eq. (5.3) in PIC and Vlasov simulations, using $L = 158.4/k_0$ [The data used for the production of the PIC results are produced by Mina Papahn Zadeh].

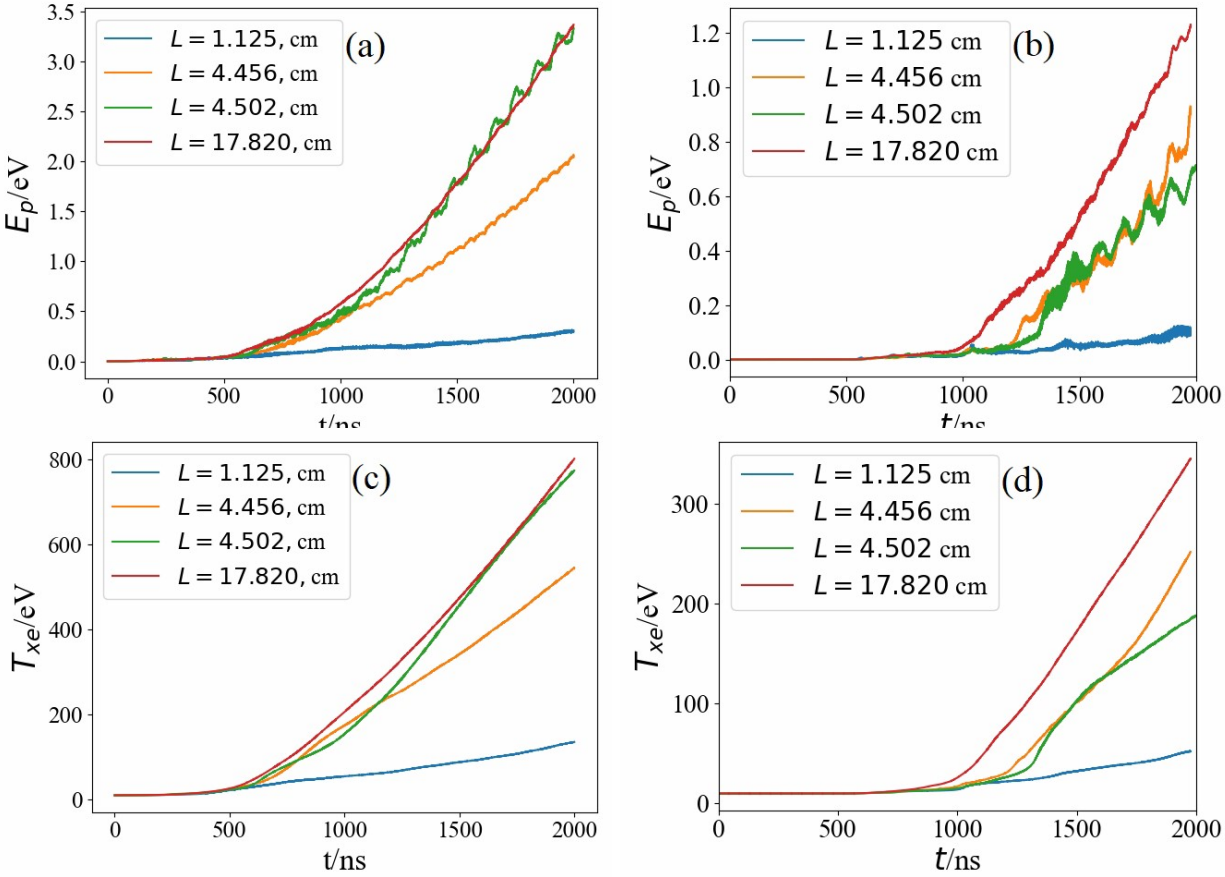

Figure 5.9: The effect of the azimuthal length on the electrostatic energy (E_p) and the electron temperature (T_{xe}). (a) and (c) are the PIC results ($N_{ppc} = 10^4$). (b) and (d) are the Vlasov results [The data used for the production of the PIC results are produced by Mina Papahn Zadeh].

5.9 The anomalous electron transport

Figs. 5.10a and 5.10b show the spatially averaged anomalous current for the Vlasov and PIC simulations, respectively. In these figures, the $E \times B$ current is calculated as $J_{E\times B} = \frac{-e\langle n_e E_x \rangle}{B_0}$, where the averaging is over the azimuthal length and a large time window. The $E \times B$ current is quite close to the moving average of the anomalous current $\langle J_{ze} \rangle$. This effect was also observed in all other simulations performed in this study with both PIC and Vlasov methods [8, 9]. Fig. 5.11 shows $\langle J_{ze} \rangle$ for the PIC and Vlasov simulations. Because the wasted energy is proportional to the total time average of $\langle J_{ze} \rangle$ (Eq. (5.3)), this quantity is also shown as horizontal lines in Fig. 5.11. Another reason for plotting these lines is that, in the absence of complete saturation, they help us better compare the results of different simulations. In Fig. 5.11, we see that similar to the electrostatic energy and electron temperature, the total time average of the $\langle J_{ze} \rangle$ is much smaller in the Vlasov simulation than the PIC simulations. During the nonlinear regime, the $\langle J_{ze} \rangle$ in the Vlasov simulation also generally remains much smaller than in the PIC simulations (except temporarily at $t \approx 1450$ ns). The value of $\langle J_{ze} \rangle$ of the PIC simulations with 10^3 and 10^4 particles per cell are close to each other, whereas the anomalous current of the simulation with 10^2 particles per cell is slightly larger than the other two. Similar to Figs. 5.8a and 5.8b, the shifted anomalous current in the Vlasov is also shown on Fig. 5.11, but it does not significantly affect the mentioned comparison of the PIC and Vlasov simulations.

Fig. 5.12 shows $\langle J_{ze} \rangle$ for different azimuthal lengths for both PIC and Vlasov simulations. We can see that, similar to the temperature and the electrostatic energy, the total time average of $\langle J_{ze} \rangle$ increases with the azimuthal length in both PIC and Vlasov simulations. Also, the transient behaviour of the moving average generally shows the same trend, except for some short times in the nonlinear regime. The total time average of $\langle J_{ze} \rangle$ for all azimuthal lengths is larger in the PIC simulations than in the Vlasov simulation.

To study the sensitivity of the $\langle J_{ze} \rangle$ to a small variation of the azimuthal length, this quantity is shown for $L = 156.8/k_0$ and $L = 158.4/k_0$ in Fig. 5.12. In Fig. 5.12b, we see that although this variation has a small effect on the total time average of $\langle J_{ze} \rangle$, it changes the transient behaviour. In this figure, the maximum $\langle J_{ze} \rangle \approx 0.025$ occurs at $t \approx 1450$ ns for $L = 158.4/k_0$, whereas it occurs at $t \approx 2000$ ns for $L = 156.8/k_0$. In Fig. 5.12a, we see that the total time average of $\langle J_{ze} \rangle$ in the PIC simulations is more sensitive to this small variation. In PIC simulations, although for $L = 158.4/k_0$ $\langle J_{ze} \rangle$ is generally much larger than when $L = 156.8/k_0$, they come close to each other in the last few nanoseconds.

5.10 Discussion and conclusion

In summary, physical characteristics of the ECDI are compared using the PIC and the Vlasov simulation methods. The compared characteristics include the observed growth rates in the linear regime, nonlinear saturation level, electron bunching, electron heating, anomalous current, and the effect of the azimuthal length on the saturation of the instability and the inverse cascade.

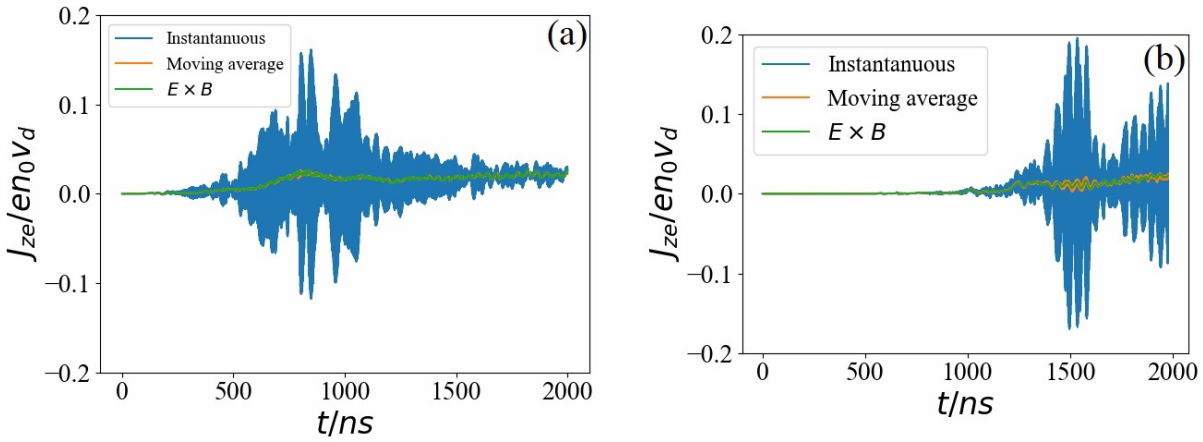

Figure 5.10: The electron anomalous current using $L = 156.8/k_0$ in a) PIC with 10^4 particles per cell b) Vlasov [The data used for the production of the PIC results are produced by Mina Papahn Zadeh].

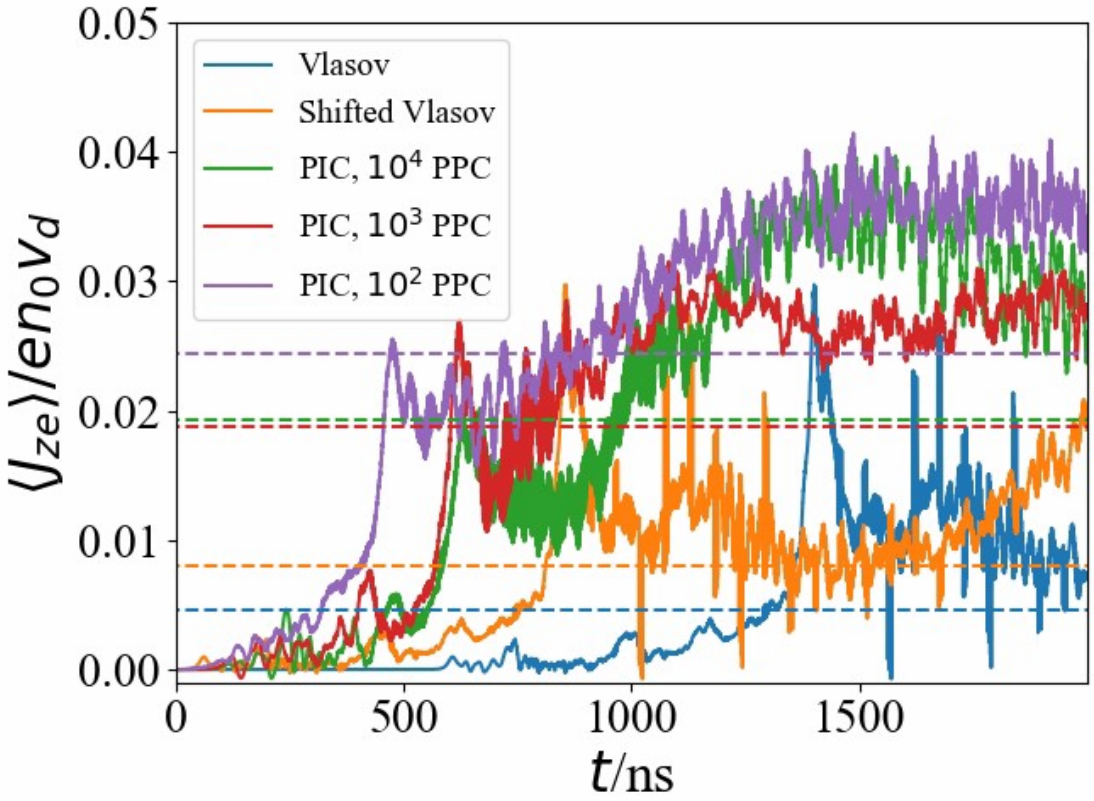

Figure 5.11: The moving average of the electron anomalous current, $L = 158.4/k_0$. The horizontal dashed lines show the total time average of each curve [The data used for the production of the PIC results are produced by Mina Papahn Zadeh].

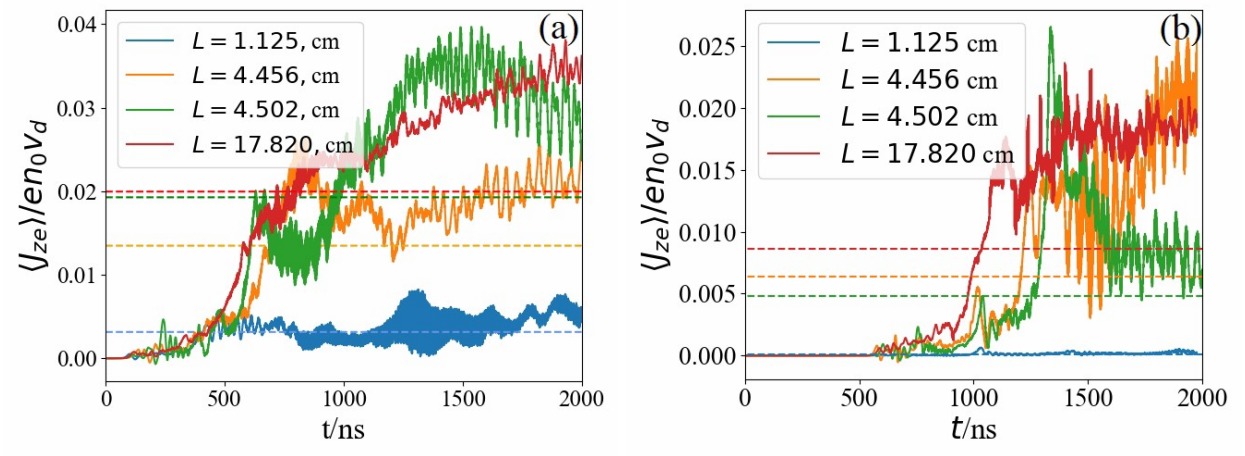

Figure 5.12: The effect of length on the $\langle J_{ze} \rangle$ in a) PIC simulation with $N_{ppc} = 10^4$ and b) Vlasov simulation. The horizontal dashed lines show the total time average of each curve [The data used for the production of the PIC results are produced by Mina Papahn Zadeh].

In the linear regime, resolving large variations of the growth rates with the wave vector requires a particularly high Fourier resolution, i.e., a long azimuthal length. Although the linear regime of PIC simulations with $156.8/k_0$ shows linear growth rates close to the theory, this was not true for the case of $L = 627/k_0$. For the latter case, the Vlasov simulation showed a better consistency with theory, especially for the low-growth rate modes that did not exist in the simulations with $L = 156.8/k_0$. This means that the low resolution in Fourier space might overshadow the adverse effect of the noise of the PIC simulation on the linear growth rates.

In this study, we referred to the appearance of modes with $k \lesssim k_0$ in the nonlinear regime that have no significant linear growth rate as the inverse cascade. The inverse cascade was clearly seen in the nonlinear regime of PIC and Vlasov simulations when L was sufficiently large. The inverse cascade happens along with the growth of the electrostatic energy in the first and other cyclotron peaks. An apparently similar process is discussed in the electromagnetic study of Ref. [25], where it is shown that the cyclotron peaks with $k > k_0$ are damped out while the first cyclotron peak grows. This process is not exactly the same as what we see in Figs. 5.4a to 5.4d of this study; because although we see the growth of the first cyclotron peak in that figure, other cyclotron peaks are also growing in the nonlinear regime. Therefore, the spectrum of the electric field in the late nonlinear regime remains discrete together with a notable energy in the $k \lesssim k_0$ region.

The inverse cascade has also been studied in the context of two-dimensional fluids[171, 172] and plasmas [173, 174]. The inverse cascade, i.e. energy flow toward the larger scales, is a result of the additional conserved quantity (enstrophy integral) in two-dimensional systems, such as in magnetized plasmas, where the motion in the plane perpendicular to the magnetic field is two-dimensional [173]. We believe that the inverse energy cascade, observed in our simulations, also occurs due to the two-dimensional nature of the electron dynamics, which remains strongly magnetized. It is interesting that in our simulations, the inverse cascade in real space

is accompanied by the formation and merging of electron structures in the phase space, and therefore, these two effects might be related. Studies of phase-space structures [175] have a long history; e.g., see reviews in Refs. [176, 110]. It is noteworthy that, because of the observed differences in the dynamics of the bunches in the PIC and Vlasov simulations, the merging of bunches might have been impacted by the numerical noise. In the PIC simulations, the merging eventually leads to a large solitary structure [177], whereas it terminates in a few co-existing bunches in the Vlasov simulations. The exact nature of these bunches and their probable impact on the inverse cascade are left for future studies.

The discrete nature of nk_0 modes that we observed in our simulations is at odds with the prediction of the ion-sound theory and suggests that the electrons remain magnetized in the nonlinear regime. Another characteristic of the Vlasov simulations that is not predicted by the ion-sound transition theory is the robust appearance of the backward waves over all the values of L considered. The backward waves are, however, not observed in the PIC simulations of this study. Since its introduction in Refs. [20, 21], the validity of the ion-sound turbulence theory has been a subject of debate[23, 11, 178, 25]. Ref. [25] shows that this theory is only valid for the large wave numbers satisfying $k\rho_e \gtrsim 1$. This conclusion is, however, not supported by our results because in our case, several behaviors are at odds with predictions of ion-sound turbulence theory despite $k_0\rho_e \approx 1.3$ initially. This suggests that the ion-sound theory might not be valid even for large k values. The discrepancy in the setup of problems and the parameter regime of the two studies makes a direct comparison of the behaviors difficult. It is known that the noise in the PIC simulations can facilitate the transition to the ion-sound regime by imitating the collisional effects of electrons [11]. In this study, we have also shown that reducing the azimuthal length L to $19.8/k_0$ can make the frequency spectrum of the PIC simulations similar to the ion-sound dispersion relation while hampering the inverse cascade. This effect, however, was not seen in the frequency spectrum of the Vlasov simulation with the same L, probably due to the absence of statistical noise.

In the nonlinear regime of PIC simulations, the electrostatic energy first remains close to the Vlasov results, but eventually it grows much faster than in the Vlasov simulations. The same trend was also observed for the electron temperature for all the values of L considered. Therefore, our study suggests that the statistical noise of the PIC simulations might contribute to the extreme electron heating that is observed in some simulations[8, 11]. Also, when the fluctuations of the anomalous current are smoothed by applying a moving average to it, the anomalous current of the PIC simulations remains higher than Vlasov except for some transient times.

An important conclusion of our study of the effect of azimuthal length is that decreasing this length can seriously impact the physics of the simulations. In many previous two-dimensional studies of the typical Hall thruster parameter regime, an azimuthal length of about 0.5 cm to 1.5 cm is used [79, 80, 165, 13, 166, 12], which our study finds inadequate for capturing the full physics of the ECDI. The effect of the azimuthal length L on the electrostatic energy, heating, and anomalous current was considered in two ways. First, we show that increasing the L increases these quantities in both PIC and Vlasov simulations. This is in

fact expected from the linear spectrum because a significant increase in L leads to many more unstable resonant modes being resolved in the simulation. Second, we have shown that the electrostatic energy, the electron temperature, and the anomalous current can be sensitive to a small variation in L. This sensitivity is generally much higher in the PIC simulations than in the Vlasov simulations. At present, we do not have a conclusive answer as to why this sensitivity exists. From the steep spectrum of linear growth rates, it is evident that small variations of L can drastically change the growth rate of the unstable modes. This means that this sensitivity can be partially due to the underlying physics of the ECDI problem. On the other hand, because this sensitivity is different in the PIC and Vlasov simulations, one can conclude that in addition to the physics of ECDI, numerical effects are partially responsible for this sensitivity.

It is possible to reduce the initial noise in the PIC simulations by using the quiet-start initialization [81]. However, this method only removes the noise in the initial time step, and after this time, the PIC simulations are affected by the noise. In fact, if the initial amplitudes are very small, the effect of the noise on them can be even amplified in the quiet start simulations[60]. Filtering can be used to reduce the noise, albeit with increased computational cost. There are many low-pass filters proposed in the literature, each with pros and cons[179]. Another method for reducing the noise of the PIC simulations is the delta-f method[105, 106, 107]. In this method, the distribution function is assumed to be a known function (usually Maxwellian) that is added to a small δf. The macroparticles are then only used to calculate the δf part, and the noise is reduced. We note that the filtering and the delta-f methods can also be used in the Vlasov simulations to reduce the discretization error in the velocity subspace [180, 181]. Another useful method for reducing the noise of PIC simulations is remapping. In this method, the macroparticles are frequently mapped onto a phase space grid where the distribution function is calculated [103, 104]. Investigating the effect of quiet-start, filtering, delta-f, and remapping on the ECDI simulations is beyond the scope of this study.

Many similarities and discrepancies in the PIC and Vlasov simulations discussed in this study need to be addressed in the broader context of 2D and 3D effects [80, 79] but are left for future studies. Future work can consider the electromagnetic effects using the full Maxwell equation in the simulations [25]. The electromagnetic effects might be particularly important in the study of the long-wavelength regions of the spectrum [182].

Acknowledgment

The authors acknowledge illuminating discussions with S. Janhunen. This work is partially supported in part by funding from the US Air Force Office of Scientific Research FA9550-15-1-0226 and the Natural Sciences and Engineering Council of Canada (NSERC) as well as computational resources from Digital Research Alliance of Canada (the Alliance).

Author Declarations

Conflict of interest

The authors have no conflicts to disclose.

Data Availability Statement

The data that support the findings of this study are available from the corresponding author upon reasonable request.

6 Nonlinear regimes of the electron cyclotron drift instability in Vlasov simulations

6.1 Preface

In the previous chapter, we described the ECDI through the continuum Vlasov simulations and compared the results with PIC simulations. In this chapter, other nonlinear characteristics of the ECDI are demonstrated and confirmed, using the continuum Vlasov simulation. In particular, we demonstrate the nonlinear transitions in the mode saturation and show that the ion sound turbulence theory is not likely to be valid due to these transitions.

This chapter is based on an article published in the Physics of Plasma journal [157]. The author of this thesis (A. Tavassoli) is the first author of the published article and had the highest contribution among the co-authors of this article. This contribution is as follows.

- Leading the investigation, and formal analysis of the study.
- Managing comments, suggestions, and discussions of the co-authors and reflecting them in the text of the article.
- Organizing, writing, and preparing most of the text of the article throughout the preparation and submission processes.
- Having a dominant role in the development of the "semi-Lagrangian Vlasov" code used in the article.
- Running all the simulations in the article and producing the data for making the corresponding figures.
- Post-processing with Python and producing all figures of the article.
- Being the corresponding author of the article. All correspondence with the editorial office during the publication process was done through the corresponding author.
- Reflecting the comments of the reviewers in the text of the article and preparing the text of the reply to reviewers, after discussing them with the co-others.

All the figures included in this chapter are produced by the author of this thesis.

6.2 Abstract

We report on a novel investigation of the nonlinear regime of the electron cyclotron drift instability using a grid-based Vlasov simulation. It is shown that the instability occurs as a series of cyclotron resonances with the electron beam mode due to the $E \times B$ drift. In the nonlinear regime, we observe condensation of fluctuations energy toward the lowest resonance mode and below, i.e., an inverse energy cascade. It is shown that the characteristics of the nonlinear saturation state remain far from the ion-sound regime.

It is widely accepted that the anomalous transport across the magnetic field in partially magnetized plasmas results from turbulent electrostatic fluctuations. The exact mechanism of such fluctuations in various conditions, in particular those typical for Hall thrusters, is still a subject of debate. In recent years, the electron cyclotron drift instability (ECDI), or simply the electron drift instability (EDI), has attracted a great deal of attention as a mechanism of the anomalous transport in partially magnetized plasmas, especially in the strong electric field regions, where other effects, e.g., density and magnetic field gradients, are less important [11, 12, 8, 166]. This instability is also of interest for space physics, in particular, as a dissipation mechanism for collisionless shock waves [25].

The ECDI is a reactive instability driven by the relative drift velocity between electrons and ions in partially magnetized plasmas with crossed E and B fields. An electric field $\mathbf{E}_0$ applied across the magnetic field generates an $E \times B$ drift velocity $\mathbf{v}_d = \frac{\mathbf{E}_0 \times \mathbf{B}_0}{B^2}$ of the bulk electrons (the ions are assumed to be unmagnetized). The instability occurs when the resonances of Bernstein-type (cyclotron) modes and the ion-sound mode become possible due to the Doppler frequency shift due to the electron $E \times B$ drift. Under the conditions in Hall thrusters, where the magnetic field $\mathbf{B}_0$ and the electric field $\mathbf{E}_0$ are applied in the radial and axial directions, respectively, the fluctuations propagate in the azimuthal direction [6]. Experiments [169, 183] report observations of such small-scale azimuthal fluctuations in the acceleration region of Hall thrusters are presumably responsible for anomalous axial electron transport.

The linear regime of the ECDI is well understood based on the linear dispersion relation [38, 184]. However, understanding of the nonlinear regimes remains elusive. In part, the understanding is obscured by the results of the linear theory that for finite and sufficiently large values of the wave vector along the magnetic field, $k_z v_{te} > \omega_{ce}$ (v_{te} is the electron thermal velocity and ω_{ce} is the electron cyclotron frequency), the cyclotron resonances are smeared out by the electron motion along the magnetic field, and the instability is reduced to the ion-sound instability driven by the electron $E \times B$ beam.

It has been suggested that even for purely perpendicular propagation, when $k_z = 0$ and the above linear effect is absent, the nonlinear resonance broadening due to the nonlinear diffusion may result in the overlapping resonances effectively demagnetizing the electron response. A nonlinear theory of the ECDI based on the resonance broadening in the strong turbulence regime [185, 186] was proposed in Refs. [20, 21, 178]. As a result, an initial strong ECDI instability would saturate and proceed further as a slow ion-sound instability, similar to the ion-sound instability in plasmas without a magnetic field. Such behavior

was also demonstrated in earlier Particle-in-Cell (PIC) simulations [20]. At the same time, it was argued that in similar PIC simulations, properties of the ECDI remain unlike those of unmagnetized ion-sound instability [23]. Comparison of the properties of ECDI with unmagnetized ion-sound instability in the context of the collisionless shock waves in space also showed significant differences [25].

A quasi-linear theory based on the assumption of unmagnetized ion-sound turbulence was used to explain the anomalous mobility caused by the ECDI [9]. In this approach, the anomalous current is calculated from the $E \times B$ drift, in the self-consistent electric field, i.e., $J_{ze} = \frac{\langle n_e \tilde{\mathbf{E}} \times \mathbf{B}_0 \rangle}{B_0^2}$, where n_e and $\tilde{\mathbf{E}}$ are the electron density and the self-consistent electric field and are calculated as for unmagnetized ion-sound turbulence. These results were validated against some particle-in-cell (PIC) simulations [13, 165, 187].

Many PIC simulations have been performed recently to investigate the nonlinear regimes of the ECDI in various conditions [11, 12, 8, 166, 159, 10, 79, 80, 188, 154]. In Ref. [11], one-dimensional (1D) PIC simulations of the ECDI are presented in the parameter regime close to the typical conditions of Hall thruster operation. Various aspects of the nonlinear behavior, such as the significant flattening of the distribution function from Maxwellian and the inverse cascade of electrostatic energy to low-k modes, were revealed. It was shown that the criteria of Refs. [20, 21] for electron demagnetization are not generally satisfied. Two-dimensional (2D) effects are also studied in a subsequent paper [12], where it is found that the nonlinear regime is affected by the long-wavelength modified-two-stream modes and the low harmonics of the ECDI modes, so that the magnetic field remains important, unlike the unmagnetized ion-sound instability.

A weakness of the PIC method is the significant amount of noise it introduces in the simulations due to the finite number of macro particles. It is known that the noise of PIC simulations can significantly affect the overall physics of a problem, potentially changing the outcome [60]. An example of such effects was observed in PIC simulations of the heat transport in electron temperature gradient turbulence, which can be dominated by noise effects [69]. The noise of PIC simulations can be reduced by increasing the number of the macro particles, but this reduction comes at a large computational cost because the noise only decreases as the inverse square root of the number of macro particles. In studies of the ECDI, there are concerns that the noise of PIC simulations can facilitate resonance broadening and transition to the ion-sound regime by enhancing the nonlinear diffusion effects [8, 11, 189].

An alternative to the PIC method is based on the Vlasov equation, which is known to be free of the statistical noise introduced by the discrete nature of the macro particles in PIC simulations. In this Letter, we report on novel investigations of the ECDI using low-noise, grid-based Vlasov simulations in one spatial and two velocity dimensions. Although Vlasov simulations of plasma instabilities are well studied and widely used in various settings [190] including applications relevant to Hall thrusters [191], to the best of our knowledge, this is the first attempt to specifically address the nonlinear regime of the ECDI using Vlasov simulations. We show that the nonlinear stage of the mode growth exhibits several transitions between different regimes dominated by the growth of the low-k modes, attaining increasing growth rates much larger than those of the high-k modes. An intense first cyclotron-resonance mode appears in the initial nonlinear stage, with even

longer wavelength modes appearing in the later stages. Similar transitions are also observed in the spatial profile of the electron density. This behavior is a signature of the inverse cascade of the electrostatic energy towards low-k modes. The wavelengths of these high-growth-rate low-k modes remain well below those of the ion-sound modes, which have a maximum growth rate of $1/\sqrt{2}\lambda_D$, where λ_D is the Debye length of electrons. This discrepancy suggests that the nonlinear regime of ECDI cannot be explained by the ion-sound turbulence theory for an unmagnetized plasma.

In our setup, we take $\mathbf{B}_0 = B_0\hat{\mathbf{y}}$, $\mathbf{E}_0 = E_0\hat{\mathbf{z}}$, and $\tilde{\mathbf{E}} = E_x\hat{\mathbf{x}}$. The code used in this study is a 1D2V Vlasov code that uses the well-known semi-Lagrangian method [48, 49, 90, 56]. A second-order operator splitting scheme is used in this method [52]. The Vlasov equations of the electrons and ions are split into three equations; the convection equation, the momentum balance equation in the $\hat{\mathbf{x}}$ direction, and the momentum balance equation in the $\hat{\mathbf{z}}$ direction, noting that the ions are unmagnetized and hence the last equation for ions is trivial. Each equation is then solved using the method of characteristics with cubic-spline interpolation. The Poisson equation is solved, following the convection steps, using the fast Fourier transform. In our simulation, we use parameters close to the typical operation regime of the Hall thrusters that were also used in the PIC simulations of Refs. [11, 12]; i.e., $E_0 = 200$ V/cm, $B_0 = 200$ G, ion mass $m_i = 133.3$ u (Xenon), density $n_0 = 10^{17}$ m^{-3}, electron temperature $T_{e0} = 10$ eV, and ion temperature $T_{i0} = 0.2$ eV. The length of the system is taken to be $L = 4.456$ cm, and 2048 cells are used to resolve it, giving a partial resolution of 0.29 λ_D. The velocity grids consist of 1200×1200 cells with a resolution of 0.054 v_{te} for the electrons and 200×200 cells with a resolution of 10^{-4} v_{te} for the ions. Due to the low-noise feature of the Vlasov simulations, an initial perturbation is required to excite the instability. Accordingly, we perturb the initial densities as $n_i = n_e = n_0\Big[1 + 1.41 \times 10^{-4}\cos\big(2\pi x/L\big)\Big]$. The boundary conditions are periodic in physical space and open in velocity space. The time step in our simulations is 1.1×10^{-11} s $\approx 0.2\ \omega_{pe}$. To confirm the validity of our results, we also repeated the simulation with finer grids and smaller time steps, and the results were in good agreement.

In the linear regime, the overlapping resonances of Bernstein and ion-sound modes lead to a resonance condition $\omega/v_d - nk_0 - k_x = 0$, where ω is the real frequency, k_x is the wave vector in the x-direction, $k_0 \equiv \omega_{ce}/v_d$, and $n = 1, 2, 3, \ldots$ shows the number of cyclotron resonances. The full dispersion relation and some of its important limits are discussed in Ref. [12]. To find the linear growth rates, the dispersion relation can be solved by an iterative method as discussed in Ref. [39]. For exclusive perpendicular propagation, that is $k_y = 0$, the unstable growth rates form discrete bands around the resonance wave vectors $k_x = nk_0$ (see Fig. 6.1a). The maximum growth rate of each band does not exactly belong to the corresponding resonance wave vector but to a slightly larger one. On the other hand, from simulation we obtain the amplitude of the individual Fourier modes using the fast Fourier transform (FFT) (Fig. 6.1b). We note that only the modes $k_x = 2m\pi/L$ are resolved by our simulation ($m = 1, 2, 3, \ldots$). In Fig. 6.1b, two modes around the first cyclotron resonance ($m = 31, 32$), two modes around the second resonance ($m = 55, 56$), and two modes around the third resonance ($m = 77, 78$) are plotted. These modes start to grow linearly after a few

nanoseconds, and the linear growth for most of them ends after about 450 ns to 600 ns. The derivative of the amplitude in the linear growth regime represents the growth rate of each mode. These growth rates are compared with the theoretical growth rates in Fig. 6.1a. We note that, due to the steep variations of the unstable growth rates in the 1D configuration, direct growth rate measurements can be highly affected by aliasing or numerical error in the simulations. Therefore, providing data to accurately make this measurement can be challenging for any numerical solver. Nevertheless, Fig. 6.1a shows that our low-noise Vlasov solver is capable of reproducing the theoretical growth rates with reasonable accuracy.

Fig. 6.1b and Fig. 6.2 show different modes and transitions observed in our simulations. The mode $m = 26$ is the dominant mode of the nonlinear regime. Because its wave vector is close to k_0 ($k_0 L/2\pi = 24.95$), in what follows, we refer to this mode as the "$k \approx k_0$" mode. The amplitude of this mode remains relatively small in the linear regime and exhibits several transitions between different growth regimes in the nonlinear regime (see Fig. 6.1b). In Fig. 6.1b, we have marked five of these transition times with $t_1 = 626$ ns, $t_2 = 718$ ns, $t_3 = 820$ ns, $t_4 = 1090$ ns, and $t_5 = 1225$ ns. Also, the mode $m = 2$ shows some transitions in Fig. 6.1b. This mode does not show any clear growth in the linear regime, whereas its amplitude grows significantly in the nonlinear regime. Several transitions can also be seen in the profile of the electron density in Fig. 6.2, where we have marked five of these transition times as $t'_1 = 626$ ns, $t'_2 = 690$ ns, $t'_3 = 800$ ns, $t'_4 = 1090$ ns, and $t'_5 = 1200$ ns. We note that these transition times are close to t_1 to t_5 in Fig. 6.1b, suggesting a possible correlation between the transitions in electron density and the dominant mode of the nonlinear regime.

In Fig. 6.2, for times before t'_1, the main observed mode is the dominant mode of the linear regime. Between t'_1 to t'_5, several transitions can be observed in the wave number and the phase velocity of the dominant modes. A general tendency for transition from shorter wavelengths to longer wavelengths is observed (the inverse cascade). These transitions can be seen for example at t'_3 and t'_4, where some of the preexisting equi-density lines are truncated. At about t'_5, we see a transition to the coherent regime (where $k \approx k_0$ is the dominant mode) along with the appearance of some long-wavelength modes with a characteristic size of about the system length ($m = 1$ and $m = 2$).

In Fig. 6.3a, the amplitudes of various Fourier modes of the electric field (E_k) are shown. The simulated growth rates, defined by $\gamma_{sim}(k,t) \equiv \frac{\mathrm{d} \ln E_k}{\mathrm{d}t}$, are shown in Fig. 6.3b. To exclude the fast fluctuations of amplitude, the moving average of E_k (with a window of $3/\omega_{pi}$ in length) is used to calculate γ_{sim}. In Fig. 6.1b and at about $t \approx 550$ ns, the modes $m = 2, 26$ show a fast transition to high amplitudes. Fig. 6.3b shows that, at the beginning of nonlinear regime (about $t = 600$ ns), most of the modes with a small linear growth rate show a similar transition. An explanation for this transition can be that the low-growth-rate modes are nonlinearly locked to the high-growth-rate modes of the linear regime. For some of the modes, such as $m = 2, 26$, this transition starts sooner than for others, and the difference in transition start times forms some "secondary discrete bands" of high-growth-rate modes, with $k \approx nk_0/3$, at the imminent nonlinear regime (see $t \approx 500$ ns to $t \approx 550$ ns in Fig. 6.3b).

In the early nonlinear regime, the inverse cascade can be observed in the spectrum of the electric field and

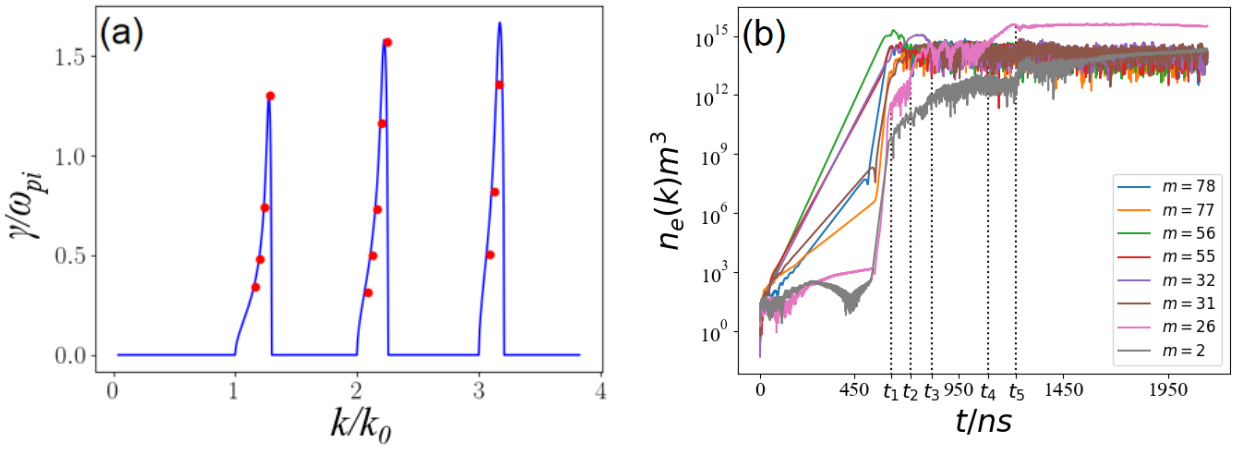

Figure 6.1: a) Comparison of theoretical growth rates (blue lines) and growth rates found from simulation (red circles). b) Amplitudes of individual Fourier modes of electron density.

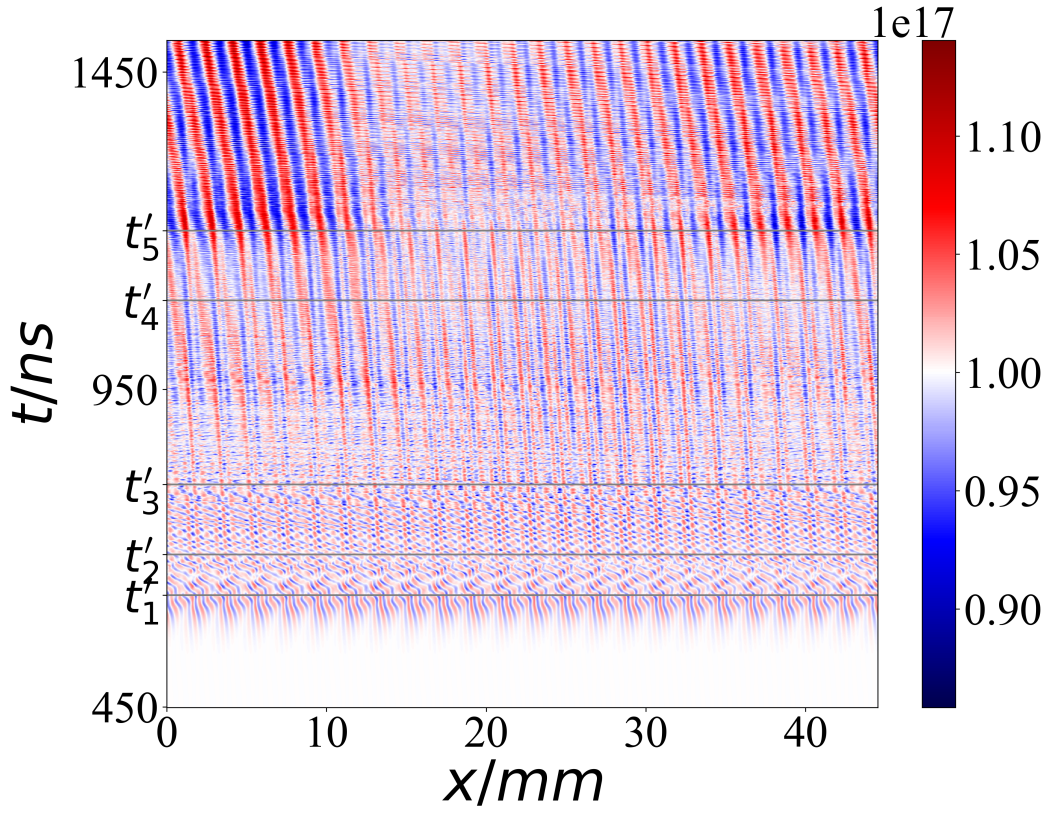

Figure 6.2: The profile of the electron density in m^{-3}. 1 ns= 17.84 ω_{pe}^{-1}, 1 mm=13.45 λ_D.

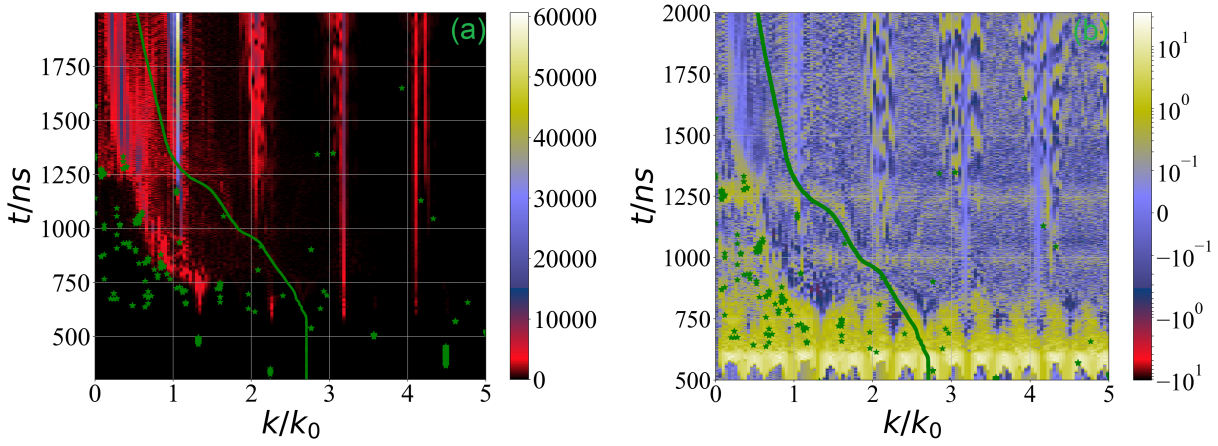

Figure 6.3: a) E_k in V/m. b) γ_{sim} in ω_{pi}. The evolution of the k^*_{is} value is shown by a green line. Green $*$ markers show the (k,t) positions of the most unstable modes in simulations (k^*_{sim}); the green color is not related to the mode amplitudes. 1 ns= 17.84 ω_{pe}^{-1}.

the growth rates in Figs. 6.3a and 6.3b. It is observed that the inverse cascade continues until $t \approx 1200$ ns to $t \approx 1250$ ns. We note that this time approximately coincides with t_5, which marks the transition of $k \approx k_0$ to the saturated state (see Fig. 6.1b). The quantity $k^*_{sim}(t)$ is defined as the maximum k of the function γ_{sim} at each time instant and is also shown in Figs. 6.3a and 6.3b. Fig. 6.3b shows that during the inverse cascade, the maximum growth rates mostly belong to low-k modes, leading to an increasing amplitude of these modes in Fig. 6.3a. On the other hand, Ref. [21] derives the ion-sound growth rate for the nonlinear regime of the ECDI as $\gamma_{is}(k,t) = \left[\pi/8(m_e/m_i)\right]^{1/2} k v_d \left(1+k^2\lambda_D^2\right)^{-3/2}$. Therefore, the maximum growth rate is expected to occur at $k^*_{is} = \frac{1}{\sqrt{2}\lambda_D}$. Nevertheless, Figs. 6.3a and 6.3b show that k^*_{is} and k^*_{sim} remain far from each other during the nonlinear evolution of ECDI. To calculate λ_D in k^*_{is}, we have replaced the electron temperature from the simulation (see Fig. 6.6), i.e., $\lambda_D(t) = \sqrt{\epsilon_0 \langle T_{xe}\rangle_L / n_0 e^2}$, where $\langle T_{xe}\rangle_L$ is the spatially averaged electron temperature along the x-direction.

The frequency spectrum of E_x in the nonlinear regime is shown in Fig. 6.4. Similar to the PIC simulations [11], the dominant frequencies of E_x are found to be close to ω_{pi} and its harmonics. Quite different from the ion-sound dispersion relation, the frequency spectrum maintains its discrete feature in the nonlinear regime. The discreteness of the frequency spectrum is also shown in the PIC simulation of Ref. [11]. Another point in Fig. 6.4 is the appearance of the waves moving in the opposite direction of the $E \times B$ drift (backward waves). These waves (also seen at some locations in Fig. 6.2) are usually a result of the strong modification of the electron distribution function due to trapping in high-amplitude potential wells of the electric field [88, 136, 16, 30]. A similar feature of the backward waves has also been observed experimentally in the Hall thruster plasma [169, 170].

The inverse cascade can also be seen in the spectrum of the anomalous current, J_k, in Fig. 6.5a. Due to the inverse energy cascade, intense modes are seen in the region $k \lesssim k_0$, similar to previous works [12, 11, 168, 188].

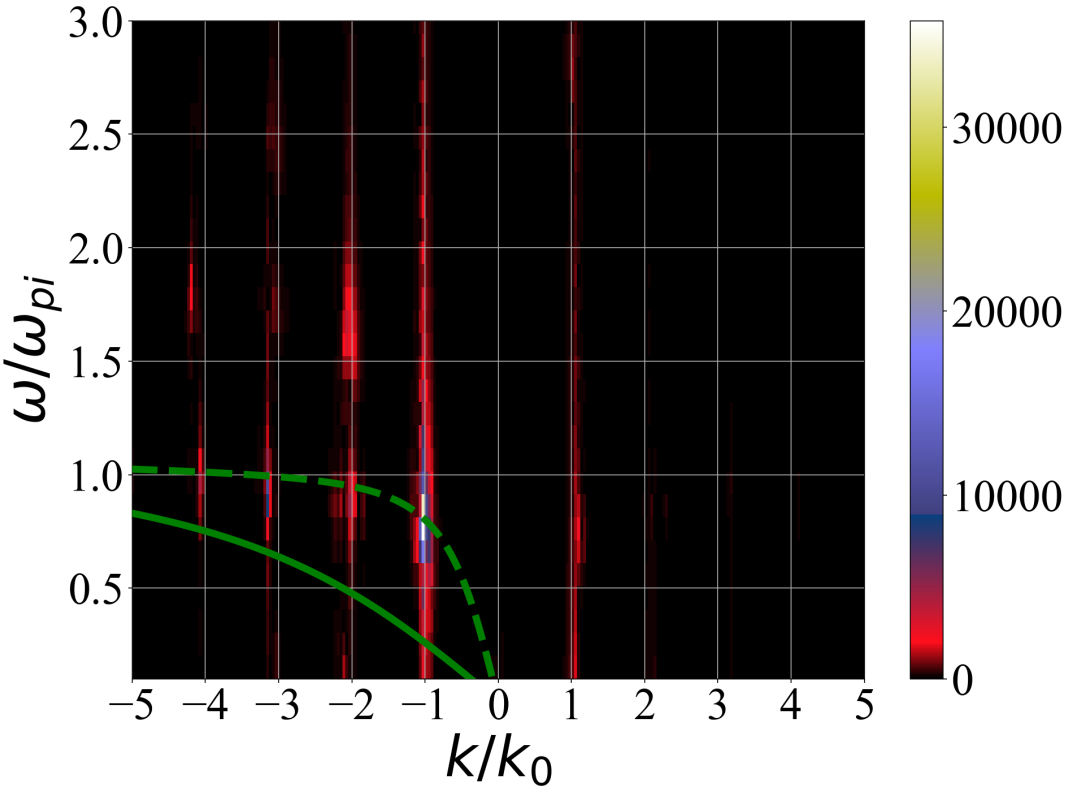

Figure 6.4: The frequency spectrum of E_x, in the nonlinear regime. The green solid line and the green dashed line show the ion-sound dispersion relation with the initial temperature and the average temperature at $t = 2139$ ns, respectively. In the setup of our problem $k_0\lambda_D = 0.2615$.

This is consistent with the notion that the long-wavelength modes provide the dominant contribution to anomalous transport. In the low-k region of this figure, k^*_{sim} appears in advance of the intense modes of the anomalous current. This suggests that the intense modes of anomalous current likely resulted from the growth of low-k modes of the electric field. This suggests the inverse cascade in the electric field fluctuations has an important role in the formation of the anomalous current. We note that the spectrum of the anomalous current does not show the same coherency as the electric field in Fig. 6.3a, and $k \approx k_0$ ($m = 26$) is just one mode among other intense modes. Fig. 6.5b shows the spatially averaged anomalous current and its moving average. The moving average of the anomalous current is close to the moving average of the $E \times B$ anomalous current, as suggested in Ref. [9] and also confirmed in Ref. [192]. This observation is in contrast to the PIC simulation of Ref. [11], where the $E \times B$ current is shown to be much smaller than the simulated current. Explaining this discrepancy requires an accurate comparison between the two simulations that takes into account any notable difference in the physical parameters, numerical parameters, initial conditions, and post-processing; such a comparison is beyond the scope of this study.

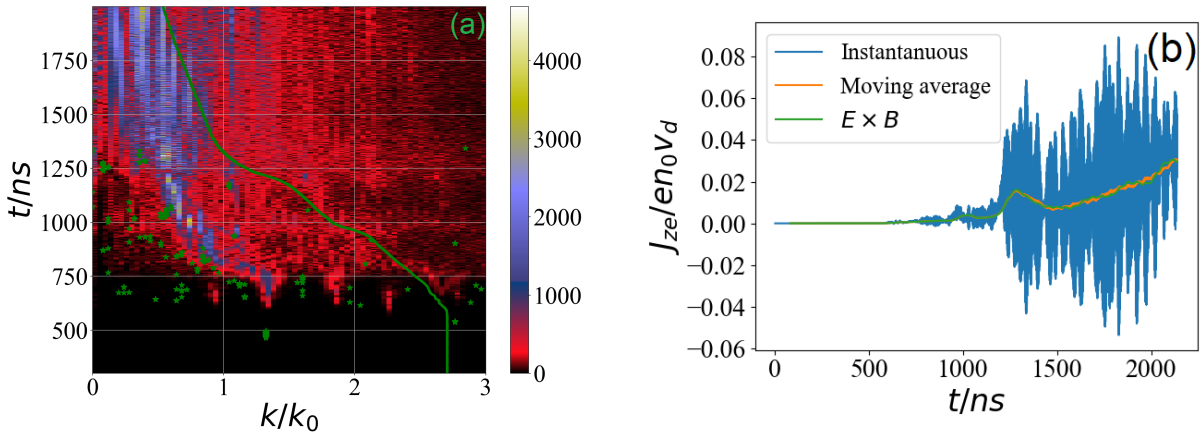

Figure 6.5: a) J_k in A/m^2, b) Comparison of the instantaneous and moving average of the anomalous current with the $E \times B$ anomalous current ($e \langle n_e E_x \rangle / B_0$). In figure (a), the green line and the green $*$ markers pinpoint the same locations as Fig. 6.3 (k^*_{is} and k^*_{sim}). 1 ns= 17.84 ω^{-1}_{pe}

.

Fig. 6.6 shows the evolution of the potential energy $E_p \equiv \frac{1}{2n_0 L} \int_0^L \epsilon_0 E_x^2 \, \mathrm{d}x$ and the spatially averaged electron temperatures. The electron temperature in the x- and z-directions ($\langle T_{xe} \rangle_L$ and $\langle T_{ze} \rangle_L$) are essentially identical during the simulation. In the deep nonlinear regime (after about $t = 1300$ ns), the temperatures and potential energy all grow as t^2. The similarity between the growth rates of the temperature and the potential energy is in contrast to those obtained from the ion-sound turbulence theory developed in Refs. [20, 178], where these quantities are expected to have different growth rates. Similar to previous PIC simulations [11, 8], no saturation is obtained in the nonlinear regime. In Ref. [8], it is suggested that the saturation occurs because of the ion trapping and only when particles are artificially replaced in the simulations when they are displaced

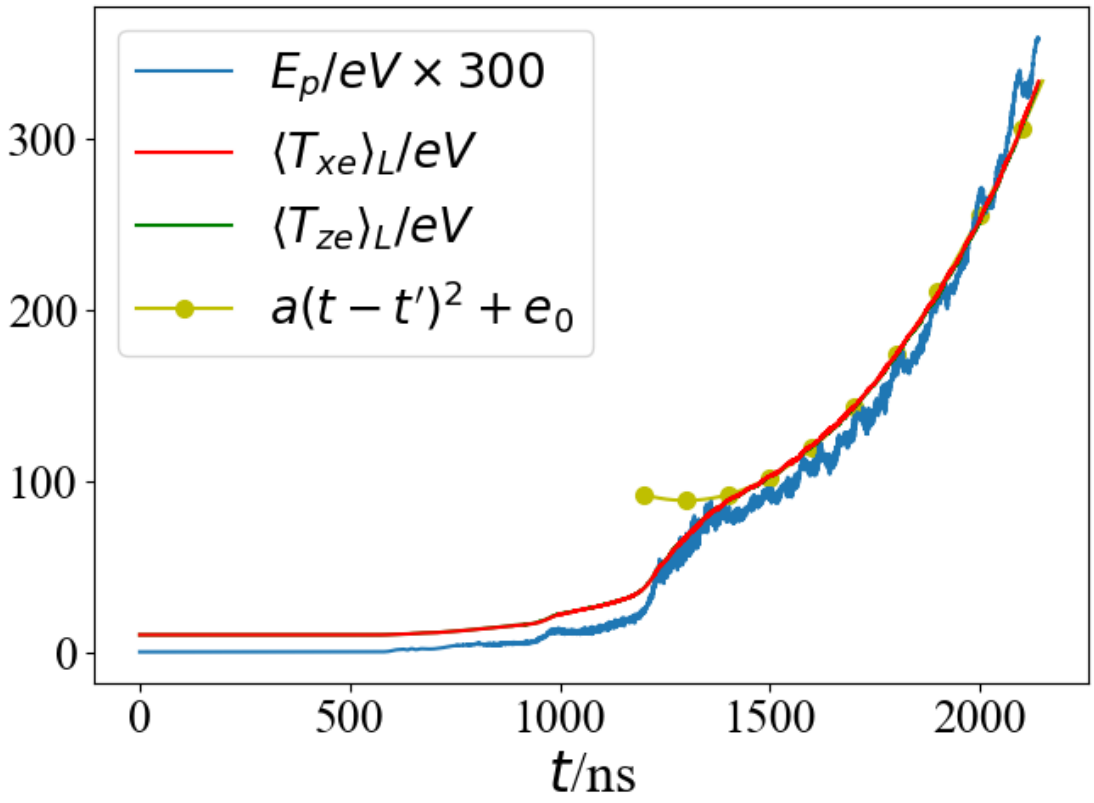

Figure 6.6: The potential energy (E_p) and spatially averaged electron temperature along x ($\langle T_{xe} \rangle$) and z ($\langle T_{ze} \rangle$). For clarity, E_p is re-scaled by a factor of 300; $t' = 1300$ ns, $a = 3.4 \times 10^{-4}$ eV/ns^2, and $e_0 = 88.4$ eV. 1 eV=0.1 T_{e0} and 1 ns= 17.84 ω_{pe}^{-1}

.

beyond some fixed axial distance (the virtual axial length model). No such particle replacement process is present in our Vlasov simulation, although it may exist naturally in azimuthal-axial simulations [160, 80, 192, 79] where particles move out of the region where there is a strong electric field.

In summary, we investigated the nonlinear regime of the ECDI using a high-resolution Vlasov simulation. This simulation is believed to be free of the statistical noise inherent in PIC simulations. A mode with $k \approx k_0$ goes through some transitions before it becomes dominant in the nonlinear regime. A somewhat similar behavior is observed in the electron density profile. It is shown that, in the early nonlinear regime, many modes with low linear growth rates show a fast transition to large amplitudes. This growth occurs as a result of a nonlinear locking of these modes to the modes with large linear growth rates, resulting in fast-growing secondary (nonlinear) modes. These transitions are followed by an inverse cascade towards the low-k modes in the nonlinear regime. The inverse cascade terminates at a particular time that is approximately the saturation time of the mode with $k \approx k_0$. The k_0 mode remains the dominant electric field mode after this time. As a result of the inverse cascade, the value of the maximum-growth-rate wave vector is much smaller than what is predicted by ion-sound turbulence theory ($k = 1/\sqrt(2)\lambda_D$), suggesting that the conditions for the applicability of the ion-sound weak turbulence theory are not likely to be valid in the nonlinear regimes of our simulation. One can expect that the resonance broadening due to the nonlinear diffusion will be even weaker in 2D and 3D simulations. In simulations that involve the direction along the magnetic field, the Modified Two-Stream Instability (MTSI) becomes important [12, 79, 188]. It is somewhat surprising that in the latter cases the linear effects of the finite wave vector along the magnetic field do not annihilate the resonant nature of the ECDI [12, 79, 188], perhaps due to the fact that the most unstable MTSI modes have long wavelengths. Such effects also depend on the specific parameters of the system, e.g., length of the region along the magnetic field. Finally, we note that some observations in our Vlasov simulation are difficult to compare with existing published PIC simulations. Direct head-to-head benchmarking of PIC and Vlasov simulations is suggested for future work.

Acknowledgment

This work is partially supported in part by US Air Force Office of Scientific Research FA9550-15-1-0226, the Natural Sciences and Engineering Council of Canada (NSERC), and Compute Canada computational resources.

Author Declarations

Conflict of interest

The authors have no conflicts to disclose.

Data Availability Statement

The data that support the findings of this study are available from the corresponding author upon reasonable request.

7 Summary and discussion

In summary, we investigated several phenomena in different regimes of the unmagnetized Buneman and the electron cyclotron drift instabilities. For this purpose, we developed, tested, and used a semi-Lagrangian Vlasov simulation code. The linear regime of these instabilities was investigated and compared with analytical theory to measure the accuracy of different numerical methods and the role of numerical noise. For the nonlinear regimes, comparisons of the results of our Vlasov code against the available PIC codes provided valuable insight into the specific effect of numerical PIC noise on the physics of the problem.

In Chapter 3, we discussed the setup of the Buneman instability and the basic equations that govern its linear and nonlinear regime. Using the results of several random-start PIC simulations, we showed that these simulations show a linear growth rate higher than the theory. This discrepancy was attributed to the early trapping of particles that leads to a small flattening in the distribution function and increases the growth rates. On the other hand, the linear growth rates measured by the Vlasov simulations were consistent with the theory. We also investigated the effect of the quiet start on the accuracy of the linear growth rates in the PIC simulations. Although the quiet-start did not completely solve the problem, it mitigated some noise problems but only when the maximum-growth-rate modes were perturbed initially.

In Chapter 4, we investigated the nonlinear regime of the Buneman instability using our semi-Lagrangian Vlasov code. Although the focus of this chapter was on the backward waves, other nonlinear phenomena such as ion and electron trapping and nonlinear heating were also discussed. The backward waves are associated with a wide plateau in the electron velocity distribution function that spreads to the negative velocities. A linear theory based on the nonlinearly modified distribution function was also introduced. It was shown that the nonlinear forward and backward waves could be explained based on this theory. In addition, an approximate threshold of the initial drift velocity for the generation of backward waves was calculated.

In Chapter 5, we discussed several phenomena through the Vlasov and PIC simulation of ECDI and compared the results of the two methods. In particular, it was shown that the intensity of ECDI fluctuations, the heating, and the anomalous current are much larger in the PIC simulations than in the Vlasov simulations. The inverse cascade was demonstrated and associated with the merging of the electron bunches in the phase space. It was also shown how the azimuthal length of the simulations could affect the physics of the ECDI problem, as well as the results of the comparison between PIC and Vlasov.

Finally, in Chapter 6, we discussed the nonlinear regime of the electron-cyclotron drift instability. Using the results of a simulation with our semi-Lagrangian Vlasov code, we demonstrated the inverse cascade and showed that the behavior of the ECDI modes remains distinct from the predictions of the ion-sound turbulence

theory. The inverse cascade is shown to happen through several transitions in the nonlinear regime.

Chapters 3, 4, 5, and 6 of this thesis were based on published or submitted manuscripts, in which the author of this thesis was the first author. In particular, Chapter 3 is based on Ref. [60], Chapter 4 is based on Ref. [88], Ref. Chapter 6 is based on [157]. Chapter 5 is based on Ref. [193], which has recently been submitted to the journal Physics of Plasmas. The exact contribution of the author of this thesis in these works is clarified in the preface to each chapter.

Plasma simulations are often so expensive that even today's most powerful supercomputers are unable to perform them with realistic sizes and parameters. This means that, in many simulations, a trade-off between the accuracy and the computational size of the problem is inevitable. A bottleneck in increasing the performance of the Vlasov simulations is the number of grid points in which the distribution function is essentially zero. This problem is exacerbated in the high-dimensional simulations because of the large hypervolume of the phase space occupied by these points. In our semi-Lagrangian Vlasov code, we ameliorated this problem by using time-dependent boundaries. This technique is particularly useful for simulations that include a wide range of the temperatures, such as the ECDI. A more powerful tool can be an adaptive mesh in the phase space, which effectively focuses the computational power among the different regions of the phase space [194, 195].

The current Vlasov code is parallelized with the shared-memory method. Distributed-memory parallelization of this code (or a hybrid shared-memory distributed-memory approach) is likely to improve its scaling. However, one should note that the current cubic spline interpolation is a global interpolation scheme that requires an all-to-all communication pattern between the nodes. Although the distributed memory parallelization is done using these global schemes [59], a better scaling can be achieved using a local cubic spline scheme [196]. There is also a class of the local conservative interpolation schemes suggested in the literature [197]. We note that local interpolation schemes are, in general, more oscillatory and less stable than the global schemes [198]. Another promising local interpolation scheme that can further reduce the communication overhead without compromising the accuracy is the discontinuous Galerkin [199, 200, 201]. The parallelization on GPU is another approach that has been successfully implemented in some recent works [180, 202, 203].

Our study is limited to one spatial dimension. Further studies are necessary to investigate how 2D and 3D effects may affect our physics results, e.g., to what extent backward waves and the inverse cascade will be modified in 2D and 3D geometries. Two-dimensional simulations with plasma sources and/or self-consistent ionization [80, 152, 204] would be the next required step in Vlasov simulations of E×B plasmas. To our knowledge, there are some initial attempts at 3D simulations of the ECDI, mostly using the PIC method [204, 205, 206, 207].

The choice between the PIC and Vlasov simulations is usually dictated by the particular problem of interest and computational resources. The PIC method uses the macroparticles to effectively apply most of the velocity resolution in the particular regions of the phase space that it is mostly required. Therefore, it

has an advantage over the Vlasov methods with fixed meshes. However, some findings of this thesis suggest that the PIC simulations might be inaccurate for the study of small-amplitude phenomena such as weak instabilities or modifications in the tail of the distribution function. Also, there are some phenomena such as the transition to ion-sound turbulence and anomalous transport that can be sensitive to artificial collisions of the PIC method. Although using the PIC method for studying these phenomena might be preferred in some cases, our results suggest that the results of such studies should be interpreted with extra care.

Some findings of this thesis can be interpreted as cautionary advice for future studies, especially for 2- or 3-dimensional simulations, where the extra cost of the added dimensions might compel researchers to use simplifications that have physical consequences. For example, the computational restrictions might limit the viability of using a large number of particles per cell or the size of the simulation domain. In the Chapter 3, we show that even for 10^5 particles per cell, the linear growth rates can still be inaccurate. Also, in the Chapter 5, inaccuracies of the linear growth rates were observed even for $N_{ppc} = 10^4$. In the studies of the Bunemann instability and ECDI, a short length in the direction of propagation can lead to a low resolution in the Fourier space, which limits the number of unstable eigenmodes. In Chapter 5, we show that a short azimuthal length can impede the process of inverse cascade and mislead to a frequency spectrum that almost agrees with the predictions of the ion-turbulence theory. A short box length can also make the anomalous current significantly smaller. These points, along with others mentioned in this thesis, need to be considered and addressed in future computational studies.

References

[1] Vincent M Donnelly and Avinoam Kornblit. Plasma etching: Yesterday, today, and tomorrow. *Journal of Vacuum Science & Technology A: Vacuum, Surfaces, and Films*, 31(5):050825, 2013.

[2] Dan Lev, Roger M Myers, Kristina M Lemmer, Jonathan Kolbeck, Hiroyuki Koizumi, and Kurt Polzin. The technological and commercial expansion of electric propulsion. *Acta Astronautica*, 159:213–227, 2019.

[3] Samuel E Wurzel and Scott C Hsu. Progress toward fusion energy breakeven and gain as measured against the lawson criterion. *Physics of Plasmas*, 29(6):062103, 2022.

[4] KE Tsiolkovskiy. Works of rocket technology. *NASA Technical Translation, TTF-243, NASA*, 1965.

[5] Oleksandr Chapurin. *Flows and instabilities in low-temperature plasmas with ionization and charge-exchange processes*. PhD thesis, University of Saskatchewan, 2022.

[6] Jean-Pierre Boeuf. Tutorial: Physics and modeling of hall thrusters. *Journal of Applied Physics*, 121(1):011101, 2017.

[7] Dan M Goebel and Ira Katz. *Fundamentals of electric propulsion: ion and Hall thrusters*. John Wiley & Sons, 2008.

[8] Trevor Lafleur, SD Baalrud, and Pascal Chabert. Theory for the anomalous electron transport in hall effect thrusters. i. insights from particle-in-cell simulations. *Physics of Plasmas*, 23(5):053502, 2016.

[9] Trevor Lafleur, SD Baalrud, and Pascal Chabert. Theory for the anomalous electron transport in hall effect thrusters. ii. kinetic model. *Physics of Plasmas*, 23(5):053503, 2016.

[10] JC Adam, A Héron, and G Laval. Study of stationary plasma thrusters using two-dimensional fully kinetic simulations. *Physics of Plasmas*, 11(1):295–305, 2004.

[11] Salomon Janhunen, Andrei Smolyakov, Oleksandr Chapurin, Dmytro Sydorenko, Igor Kaganovich, and Yevgeni Raitses. Nonlinear structures and anomalous transport in partially magnetized e× b plasmas. *Physics of Plasmas*, 25(1):011608, 2018.

[12] Salomon Janhunen, Andrei Smolyakov, Dmytro Sydorenko, Marilyn Jimenez, Igor Kaganovich, and Yevgeny Raitses. Evolution of the electron cyclotron drift instability in two-dimensions. *Physics of Plasmas*, 25(8):082308, 2018.

[13] Trevor Lafleur, Roberto Martorelli, Pascal Chabert, and Anne Bourdon. Anomalous electron transport in hall-effect thrusters: Comparison between quasi-linear kinetic theory and particle-in-cell simulations. *Physics of Plasmas*, 25(6):061202, 2018.

[14] A Héron and JC Adam. Anomalous conductivity in hall thrusters: Effects of the non-linear coupling of the electron-cyclotron drift instability with secondary electron emission of the walls. *Physics of Plasmas*, 20(8):082313, 2013.

[15] P Coche and L Garrigues. A two-dimensional (azimuthal-axial) particle-in-cell model of a hall thruster. *Physics of Plasmas*, 21(2):023503, 2014.

[16] K. Hara and C. Treece. Ion kinetics and nonlinear saturation of current-driven instabilities relevant to hollow cathode plasmas. *Plasma Sources Science and Technology*, 28(5):055013, 2019.

[17] Benjamin Jorns, Dan M Goebel, and Ioannis G Mikellides. Investigation of energetic ions in a 100-a hollow cathode. In *50th AIAA/ASME/SAE/ASEE Joint Propulsion Conference*, page 3826, 2014.

[18] Alejandro Lopez Ortega and Ioannis G Mikellides. The importance of the cathode plume and its interactions with the ion beam in numerical simulations of hall thrusters. *Physics of Plasmas*, 23(4):043515, 2016.

[19] Alejandro Lopez Ortega, Benjamin A Jorns, and Ioannis G Mikellides. Hollow cathode simulations with a first-principles model of ion-acoustic anomalous resistivity. *Journal of Propulsion and Power*, 34(4):1026–1038, 2018.

[20] Martin Lampe, Wallace M Manheimer, John B McBride, Joseph H Orens, R Shanny, and RN Sudan. Nonlinear development of the beam-cyclotron instability. *Physical Review Letters*, 26(20):1221, 1971.

[21] M Lampe, WM Manheimer, JB McBride, JH Orens, K Papadopoulos, R Shanny, and RN Sudan. Theory and simulation of the beam cyclotron instability. *The Physics of Fluids*, 15(4):662–675, 1972.

[22] DW Forslund, RL Morse, and CW Nielson. Nonlinear electron-cyclotron drift instability and turbulence. *Physical Review Letters*, 27(21):1424, 1971.

[23] DW Forslund, RL Morse, and CW Nielson. On anomalous resistance due to cross-field electron-ion streaming instabilities. *The Physics of Fluids*, 15(12):2363–2366, 1972.

[24] L Muschietti and Bertrand Lembège. Electron cyclotron microinstability in the foot of a perpendicular shock: A self-consistent pic simulation. *Advances in Space Research*, 37(3):483–493, 2006.

[25] Laurent Muschietti and Bertrand Lembège. Microturbulence in the electron cyclotron frequency range at perpendicular supercritical shocks. *Journal of Geophysical Research: Space Physics*, 118(5):2267–2285, 2013.

[26] H Che, JF Drake, M Swisdak, and PH Yoon. Nonlinear development of streaming instabilities in strongly magnetized plasma. *Physical Review Letters*, 102(14):145004, 2009.

[27] Haihong Che. Electron two-stream instability and its application in solar and heliophysics. *Modern Physics Letters A*, 31(19):1630018, 2016.

[28] P. Hellinger, P. Travnicek, and J. D. Menietti. Effective collision frequency due to ion-acoustic instability: Theory and simulations. *Geophysical Research Letters*, 31(10):L10806, 2004.

[29] H Che, JF Drake, M Swisdak, and PH Yoon. Electron holes and heating in the reconnection dissipation region. *Geophysical Research Letters*, 37(11), 2010.

[30] L. P. Dyrud and M. M. Oppenheim. Electron holes, ion waves, and anomalous resistivity in space plasmas. *Journal of Geophysical Research — Space Physics*, 111(A1):A01302, 2006.

[31] B. E. Carlsten, K. A. Bishofberger, and R. J. Faehl. Compact two-stream generator of millimeter- and submillimeter-wave radiation. *Physics of Plasmas*, 15(7):073101, 2008.

[32] E. A. Startsev and R. C. Davidson. Two-stream instability for a longitudinally compressing charged particle beam. *Physics of Plasmas*, 13(6):062108, 2006.

[33] C Boniface, L Garrigues, GJM Hagelaar, JP Boeuf, D Gawron, and S Mazouffre. Anomalous cross field electron transport in a hall effect thruster. *Applied Physics Letters*, 89(16):161503, 2006.

[34] Francis F. Chen. *Introduction to Plasma Physics and Controlled Fusion*. Springer, Switzerland, third edition, 2016.

[35] José A Bittencourt. *Fundamentals of plasma physics*. Springer Science & Business Media, 2013.

[36] Dwight Roy Nicholson and Dwight R Nicholson. *Introduction to plasma theory*. Wiley New York, 1983.

[37] Thomas H Stix. *Waves in plasmas*. Springer Science & Business Media, 1992.

[38] S Peter Gary. *Theory of space plasma microinstabilities*. Number 7. Cambridge University Press, 1993.

[39] J Cavalier, N Lemoine, G Bonhomme, S Tsikata, C Honore, and D Gresillon. Hall thruster plasma fluctuations identified as the e× b electron drift instability: Modeling and fitting on experimental data. *Physics of Plasmas*, 20(8):082107, 2013.

[40] Jeffrey William Banks and Jeffrey Alan Furst Hittinger. A new class of nonlinear finite-volume methods for vlasov simulation. *IEEE Transactions on Plasma Science*, 38(9):2198–2207, 2010.

[41] Charles K Birdsall and A Bruce Langdon. *Plasma physics via computer simulation*. Taylor & Francis, 2004.

[42] A Bottino and E Sonnendrücker. Monte carlo particle-in-cell methods for the simulation of the vlasov–maxwell gyrokinetic equations. *Journal of Plasma Physics*, 81(5), 2015.

[43] Katharina Kormann, Klaus Reuter, and Markus Rampp. A massively parallel semi-lagrangian solver for the six-dimensional vlasov–poisson equation. *The International Journal of High Performance Computing Applications*, 33(5):924–947, 2019.

[44] Satoshi Tanaka, Kohji Yoshikawa, Takashi Minoshima, and Naoki Yoshida. Multidimensional vlasov–poisson simulations with high-order monotonicity-and positivity-preserving schemes. *The Astrophysical Journal*, 849(2):76, 2017.

[45] Adrien Revel, Serhiy Mochalskyy, Ivar Mauricio Montellano, Dirk Wünderlich, Ursel Fantz, and Tiberiu Minea. Massive parallel 3d pic simulation of negative ion extraction. *Journal of Applied Physics*, 122(10):103302, 2017.

[46] Scott O'Connor, Zane D Crawford, John P Verboncoeur, John Luginsland, and B Shanker. A set of benchmark tests for validation of 3-d particle in cell methods. *IEEE Transactions on Plasma Science*, 49(5):1724–1731, 2021.

[47] Phillip Colella. High-order finite-volume methods on locally-structured grids. *Discrete and Continuous Dynamical Systems-Series A*, 36(8):4247–4270, 2016.

[48] Chio-Zong Cheng and Georg Knorr. The integration of the vlasov equation in configuration space. *Journal of Computational Physics*, 22(3):330–351, 1976.

[49] CZ Cheng. The integration of the vlasov equation for a magnetized plasma. *Journal of Computational Physics*, 24(4):348–360, 1977.

[50] Eric Sonnendrücker, Jean Roche, Pierre Bertrand, and Alain Ghizzo. The semi-lagrangian method for the numerical resolution of the vlasov equation. *Journal of Computational Physics*, 149(2):201–220, 1999.

[51] Raymond J Spiteri, Arash Tavassoli, Siqi Wei, and Andrei Smolyakov. Practical 3-splitting beyond strang. *arXiv preprint arXiv:2302.08034*, 2023.

[52] Shev MacNamara and Gilbert Strang. Operator splitting. In *Splitting methods in communication, imaging, science, and engineering*, pages 95–114. Springer, 2016.

[53] Bertil Gustafsson, Heinz-Otto Kreiss, and Joseph Oliger. *Time dependent problems and difference methods*, volume 24. John Wiley & Sons, 1995.

[54] Andrew Staniforth and Jean Côté. Semi-lagrangian integration schemes for atmospheric models—a review. *Monthly Weather Review*, 119(9):2206–2223, 1991.

[55] J Harold Ahlberg, Edwin Norman Nilson, and Joseph Leonard Walsh. *The theory of splines and their applications*. Academic Press, 1967.

[56] Magdi Shoucri. The method of characteristics for the numerical solution of hyperbolic differential equations. In Albert R. Baswell, editor, *Advances in Mathematics Research, Volume 8*, chapter 1, pages 1–87. Nova Science Publishers, Inc., New York, 2009.

[57] Intel® oneAPI Math Kernel Library. `https://www.intel.com/content/www/us/en/develop/documentation/get-started-with-mkl-for-dpcpp/top.html`. Accessed: February 24, 2023.

[58] The openMP API specification for parallel programming. `https://www.openmp.org`. Accessed: February 24, 2023.

[59] Olivier Coulaud, Eric Sonnendrücker, Eric Dillon, Pierre Bertrand, and Alain Ghizzo. Parallelization of semi-lagrangian vlasov codes. *Journal of Plasma Physics*, 61(3):435–448, 1999.

[60] Arash Tavassoli, Oleksandr Chapurin, Marilyn Jimenez, Mina Papahn Zadeh, Trevor Zintel, Meghraj Sengupta, Lénaïc Couëdel, Raymond J Spiteri, Magdi Shoucri, and Andrei Smolyakov. The role of noise in pic and vlasov simulations of the buneman instability. *Physics of Plasmas*, 28(12):122105, 2021.

[61] A Bruce Langdon. Kinetic theory for fluctuations and noise in computer simulation of plasma. *The Physics of Fluids*, 22(1):163–171, 1979.

[62] James Juno, Ammar Hakim, Jason TenBarge, Eric Shi, and William Dorland. Discontinuous galerkin algorithms for fully kinetic plasmas. *Journal of Computational Physics*, 353:110–147, 2018.

[63] S Von Alfthan, D Pokhotelov, Y Kempf, S Hoilijoki, I Honkonen, A Sandroos, and M Palmroth. Vlasiator: First global hybrid-vlasov simulations of earth's foreshock and magnetosheath. *Journal of Atmospheric and Solar-Terrestrial Physics*, 120:24–35, 2014.

[64] Z Lin, L Chen, and F Zonca. Role of nonlinear toroidal coupling in electron temperature gradient turbulence. *Physics of Plasmas*, 12(5):056125, 2005.

[65] Z Lin, L Chen, Y Nishimura, H Qu, T S Hahm, J Lewandowski, G Rewoldt, W X Wang, P H Diamond, C Holland, F Zonca, and Y Li. Electron thermal transport in tokamak ETG or TEM turbulences?, Jan 2005.

[66] W Dorland, F Jenko, Mike Kotschenreuther, and BN Rogers. Electron temperature gradient turbulence. *Physical Review Letters*, 85(26):5579, 2000.

[67] Frank Jenko, W Dorland, M Kotschenreuther, and BN Rogers. Electron temperature gradient driven turbulence. *Physics of Plasmas*, 7(5):1904–1910, 2000.

[68] F Jenko and W Dorland. Prediction of significant tokamak turbulence at electron gyroradius scales. *Physical Review Letters*, 89(22):225001, 2002.

[69] WM Nevins, GW Hammett, Andris M Dimits, W Dorland, and DE Shumaker. Discrete particle noise in particle-in-cell simulations of plasma microturbulence. *Physics of Plasmas*, 12(12):122305, 2005.

[70] I Holod and Z Lin. Statistical analysis of fluctuations and noise-driven transport in particle-in-cell simulations of plasma turbulence. *Physics of Plasmas*, 14(3):032306, 2007.

[71] Lopamudra Palodhi, Francesco Califano, Mark E Dieckmann, and Francesco Pegoraro. Counterstreaming beams in magnetised vlasov plasma. *Pramana*, 93(6):1–10, 2019.

[72] Miles M Turner. Kinetic properties of particle-in-cell simulations compromised by monte carlo collisions. *Physics of Plasmas*, 13(3):033506, 2006.

[73] WM Nevins, J Candy, S Cowley, T Dannert, A Dimits, W Dorland, C Estrada-Mila, GW Hammett, F Jenko, MJ Pueschel, et al. Characterizing electron temperature gradient turbulence via numerical simulation. *Physics of Plasmas*, 13(12):122306, 2006.

[74] J Juno, MM Swisdak, JM Tenbarge, V Skoutnev, and A Hakim. Noise-induced magnetic field saturation in kinetic simulations. *Journal of Plasma Physics*, 86(4), 2020.

[75] Fabio Riva, Carrie F Beadle, and Paolo Ricci. A methodology for the rigorous verification of particle-in-cell simulations. *Physics of Plasmas*, 24(5):055703, 2017.

[76] Frederik Kesting and Giuliano Franchetti. Propagation of numerical noise in particle-in-cell tracking. *Physical Review Special Topics-Accelerators and Beams*, 18(11):114201, 2015.

[77] Miles M Turner. Verification of particle-in-cell simulations with monte carlo collisions. *Plasma Sources Science and Technology*, 25(5):054007, 2016.

[78] Miles M Turner, Aranka Derzsi, Zoltan Donko, Denis Eremin, Sean J Kelly, Trevor Lafleur, and Thomas Mussenbrock. Simulation benchmarks for low-pressure plasmas: Capacitive discharges. *Physics of Plasmas*, 20(1):013507, 2013.

[79] Willca Villafana, Federico Petronio, Andrew Christopher Denig, Marilyn Jimenez Jimenez, Denis Eremin, Laurent Garrigues, Francesco Taccogna, Alejandro Alvarez-Laguna, Jean-Pierre Boeuf, Anne Bourdon, et al. 2d radial-azimuthal particle-in-cell benchmark for e x b discharges. *Plasma Sources Science and Technology*, 2021.

[80] Thomas Charoy, Jean-Pierre Boeuf, Anne Bourdon, Johan A Carlsson, Pascal Chabert, B Cuenot, Denis Eremin, Laurent Garrigues, Kentaro Hara, Igor D Kaganovich, et al. 2d axial-azimuthal particle-in-cell benchmark for low-temperature partially magnetized plasmas. *Plasma Sources Science and Technology*, 28(10):105010, 2019.

[81] John M Dawson. Particle simulation of plasmas. *Reviews of Modern Physics*, 55(2):403, 1983.

[82] Jack A Byers and Mahesh Grewal. Perpendicularly propagating plasma cyclotron instabilities simulated with a one-dimensional computer model. *The Physics of Fluids*, 13(7):1819–1830, 1970.

[83] AA Galeev and RZ Sagdeev. Current instabilities and anomalous resistivity of plasma. *Basic Plasma Physics: Selected Chapters, Handbook of Plasma Physics, Volume 1*, page 271, 1984.

[84] H. Che. How anomalous resistivity accelerates magnetic reconnection. *Physics of Plasmas*, 24(8):082115, 2017.

[85] Martin Lampe, Irving Haber, Joseph H Orens, and Jay P Boris. Two-dimensional study of electron-ion streaming instabilities. *The Physics of Fluids*, 17(2):428–439, 1974.

[86] AR Niknam, D Komaizi, and M Hashemzadeh. Simulation of low frequency buneman instability of a current-driven plasma by particle in cell method. *Physics of Plasmas*, 18(2):022301, 2011.

[87] Roopendra Singh Rajawat and Sudip Sengupta. Particle-in-cell simulation of buneman instability beyond quasilinear saturation. *Physics of Plasmas*, 24(12):122103, 2017.

[88] Arash Tavassoli, Magdi Shoucri, Andrei Smolyakov, Mina Papahn Zadeh, and Raymond J Spiteri. Backward waves in the nonlinear regime of the buneman instability. *Physics of Plasmas*, 28(2):022307, 2021.

[89] Paul A. Lynn. *Signal Recovery, Detection and Prediction*. Macmillan Education UK, London, 1989.

[90] Réal RJ Gagné and Magdi M Shoucri. A splitting scheme for the numerical solution of a one-dimensional vlasov equation. *Journal of Computational Physics*, 24(4):445–449, 1977.

[91] B.D. Dudson, M.V. Umansky, X.Q. Xu, P.B. Snyder, and H.R. Wilson. BOUT++: A Framework for Parallel Plasma Fluid Simulations. *Computer Physics Communications*, 180(9):1467–1480, 2009.

[92] B.D. Dudson, A. Allen, G. Breyiannis, E. Brugger, J. Buchanan, L. Easy, S. Farley, I. Joseph, M. Kim, A.D. McGann, et al. BOUT++: Recent and Current Developments. *Journal of Plasma Physics*, 81(1), 2015.

[93] A.C. Hindmarsh, P.N. Brown, K.E. Grant, S.L. Lee, R. Serban, D.E. Shumaker, and C.S. Woodward. SUNDIALS: Suite of Nonlinear and Differential/Algebraic Equation Solvers. *ACM Transactions on Mathematical Software (TOMS)*, 31(3):363–396, 2005.

[94] Dmytro Sydorenko. *Particle-in-Cell Simulations of Electron Dynamics in Low Pressure Discharges with Magnetic Fields*. PhD thesis, University of Saskatchewan, 2006.

[95] Chet Nieter and John R Cary. Vorpal: a versatile plasma simulation code. *Journal of Computational Physics*, 196(2):448–473, 2004.

[96] JM Hammersley and DC Handscomb. Monte carlo methods. *Ltd., London*, 40, 1964.

[97] J Gonichon, SC Chen, LC-L Lin, and RJ Temkin. Quiet start and autotasking for parmela. In *Proceedings of International Conference on Particle Accelerators*, pages 2696–2698. IEEE, 1993.

[98] Paul Bratley and Bennett L Fox. Algorithm 659: Implementing sobol's quasirandom sequence generator. *ACM Transactions on Mathematical Software (TOMS)*, 14(1):88–100, 1988.

[99] SE Parker and WW Lee. A fully nonlinear characteristic method for gyrokinetic simulation. *Physics of Fluids B: Plasma Physics*, 5(1):77–86, 1993.

[100] Brett Scheiner and Patrick J Adrian. Why the particle-in-cell method captures instability enhanced collisions. *Physics of Plasmas*, 26(3):034501, 2019.

[101] Hideo Okuda and Charles K Birdsall. Collisions in a plasma of finite-size particles. *The Physics of Fluids*, 13(8):2123–2134, 1970.

[102] Thomas H Dupree. Kinetic theory of plasma and the electromagnetic field. *The Physics of Fluids*, 6(12):1714–1729, 1963.

[103] Bei Wang, Gregory H Miller, and Phillip Colella. A particle-in-cell method with adaptive phase-space remapping for kinetic plasmas. *SIAM Journal on Scientific Computing*, 33(6):3509–3537, 2011.

[104] Andrew Myers, Phillip Colella, and B Van Straalen. A 4th-order particle-in-cell method with phase-space remapping for the vlasov–poisson equation. *SIAM Journal on Scientific Computing*, 39(3):B467–B485, 2017.

[105] Ahmet Y Aydemir. A unified monte carlo interpretation of particle simulations and applications to non-neutral plasmas. *Physics of Plasmas*, 1(4):822–831, 1994.

[106] Stephan Brunner, Ernest Valeo, and John A Krommes. Collisional delta-f scheme with evolving background for transport time scale simulations. *Physics of Plasmas*, 6(12):4504–4521, 1999.

[107] Simon J Allfrey and Roman Hatzky. A revised δf algorithm for nonlinear pic simulation. *Computer Physics Communications*, 154(2):98–104, 2003.

[108] O Buneman. Instability, turbulence, and conductivity in current-carrying plasma. *Physical Review Letters*, 1(1):8, 1958.

[109] Oscar Buneman. Dissipation of currents in ionized media. *Physical Review*, 115(3):503, 1959.

[110] Ian Horner Hutchinson. Electron holes in phase space: What they are and why they matter. *Physics of Plasmas*, 24(5):055601, 2017.

[111] Francesco Califano, L Galeotti, and C Briand. Electrostatic coherent structures: The role of the ions dynamics. *Physics of Plasmas*, 14(5):052306, 2007.

[112] Alain Ghizzo, Magdi M Shoucri, Pierre Bertrand, Marc Feix, and Eric Fijalkow. Nonlinear evolution of the beam-plasma instabilities. *Physics Letters A*, 129(8-9):453–458, 1988.

[113] Magdi Shoucri. Formation of electron holes in the long-time evolution of the bump-on-tail instability. *Laser and Particle Beams*, 35(4):706, 2017.

[114] A Ghizzo, B Izrar, P Bertrand, E Fijalkow, MR Feix, and M Shoucri. Stability of bernstein–greene–kruskal plasma equilibria. numerical experiments over a long time. *The Physics of Fluids*, 31(1):72–82, 1988.

[115] Giovanni Manfredi. Long-time behavior of nonlinear landau damping. *Physical Review Letters*, 79(15):2815, 1997.

[116] Georg Knorr. Two-dimensional turbulence of electrostatic vlasov plasmas. *Plasma Physics*, 19(6):529, 1977.

[117] Cédric Villani. Particle systems and nonlinear landau damping. *Physics of Plasmas*, 21(3):030901, 2014.

[118] J. Buchner and N. Elkina. Anomalous resistivity of current-driven isothermal plasmas due to phase space structuring. *Physics of Plasmas*, 13(8):082304, 2006.

[119] B Shokri and AR Niknam. Nonlinear dynamic of low-frequency buneman instability of a current-driven plasma. *Physics of Plasmas*, 12(6):062110, 2005.

[120] K. Hara, I. D. Kaganovich, and E. A. Startsev. Generation of forerunner electron beam during interaction of ion beam pulse with plasma. *Physics of Plasmas*, 25(1):011609, 2018.

[121] Charles J Bartlett. Nonadiabatic behavior of plasma oscillations. *The Physics of Fluids*, 11(4):822–831, 1968.

[122] O Ishihara, A Hirose, and AB Langdon. Nonlinear saturation of the buneman instability. *Physical Review Letters*, 44(21):1404, 1980.

[123] O Ishihara, A Hirose, and AB Langdon. Nonlinear evolution of buneman instability. *The Physics of Fluids*, 24(3):452–464, 1981.

[124] A Hirose, O Ishihara, and AB Langdon. Nonlinear evolution of buneman instability. ii. ion dynamics. *The Physics of Fluids*, 25(4):610–616, 1982.

[125] PH Yoon. Weak turbulence theory for reactive instability. *Physics of Plasmas*, 17(11):112316, 2010.

[126] PH Yoon and T Umeda. Nonlinear turbulence theory and simulation of buneman instability. *Physics of Plasmas*, 17(11):112317, 2010.

[127] Y. S. Sigov and V. D. Levchenko. Beam-plasma interaction and correlation phenomena in open vlasov systems. *Plasma Physics and Controlled Fusion*, 38(12A):A49–A65, 1996.

[128] Ro Ko Mazitov. Damping of plasma waves. *Journal of Applied Mechanics and Technical Physics*, 6(1):22–25, 1965.

[129] Nicholas A Krall and Alvin W Trivelpiece. *Principles of Plasma Physics*. McGraw-Hill, 1973.

[130] Francesco Valentini, Thomas M O'Neil, and Daniel HE Dubin. Excitation of nonlinear electron acoustic waves. *Physics of Plasmas*, 13(5):052303, 2006.

[131] Francesco Valentini, Denise Perrone, Francesco Califano, Francesco Pegoraro, Pierluigi Veltri, PJ Morrison, and TM O'Neil. Undamped electrostatic plasma waves. *Physics of Plasmas*, 19(9):092103, 2012.

[132] F Valentini, D Perrone, Francesco Califano, Francesco Pegoraro, P Veltri, PJ Morrison, and TM O'Neil. Response to "comment on 'undamped electrostatic plasma waves'"[phys. plasmas 20, 034701 (2013)]. *Physics of Plasmas*, 20(3):034701, 2013.

[133] James Paul Holloway and JJ Dorning. Undamped plasma waves. *Physical Review A*, 44(6):3856, 1991.

[134] Hans Schamel. Comment on "undamped electrostatic plasma waves"[phys. plasmas 19, 092103 (2012)]. *Physics of Plasmas*, 20(3):092103, 2013.

[135] J Pavan, PH Yoon, and T Umeda. Quasilinear theory and simulation of buneman instability. *Physics of Plasmas*, 18(4):042307, 2011.

[136] Neeraj Jain, Takayuki Umeda, and Peter H Yoon. Modeling nonlinear development of buneman instability with linear dispersion theory. *Plasma Physics and Controlled Fusion*, 53(2):025010, 2011.

[137] Guo Jun and Yu Bin. Competition between buneman and langmuir instabilities. *Chinese Physics Letters*, 29(3):035203, 2012.

[138] P. H. Yoon. Weak turbulence theory for beam-plasma interaction. *Physics of Plasmas*, 25(1):011603, 2018.

[139] Francesco Valentini, Francesco Califano, Denise Perrone, Francesco Pegoraro, and Pierluigi Veltri. New ion-wave path in the energy cascade. *Physical Review Letters*, 106(16):165002, 2011.

[140] TW Johnston, Y Tyshetskiy, A Ghizzo, and P Bertrand. Persistent subplasma-frequency kinetic electrostatic electron nonlinear waves. *Physics of Plasmas*, 16(4):042105, 2009.

[141] Liang Xu, Andrei Smolyakov, Salomon Janhunen, and Igor Kaganovich. Self-acceleration and energy channeling in the saturation of the ion-sound instability in a bounded plasma. *Physics of Plasmas*, 27(8):080702, 2020.

[142] DE Smith, EJ Powers, and GS Caldwell. Fast-fourier-transform spectral-analysis techniques as a plasma fluctuation diagnostic tool. *IEEE Transactions on Plasma Science*, 2(4):261–272, 1974.

[143] E. A. Jackson. Drift instabilities in a maxwellian plasma. *Physics of Fluids*, 3(5):786–792, 1960.

[144] A. B. Mikhailovskii. *Theory of Plasma Instabilities*, volume 1: Instabilities of a homogeneous plasma. Springer, New York, 1974.

[145] S. Tsikata, N. Lemoine, V. Pisarev, and D. M. Gresillon. Dispersion relations of electron density fluctuations in a hall thruster plasma, observed by collective light scattering. *Physics of Plasmas*, 16(3):033506, 2009.

[146] T Miyake, Y Omura, H Matsumoto, and H Kojima. Two-dimensional computer simulations of electrostatic solitary waves observed by geotail spacecraft. *Journal of Geophysical Research: Space Physics*, 103(A6):11841–11850, 1998.

[147] MM Oppenheim, G Vetoulis, DL Newman, and MV Goldman. Evolution of electron phase-space holes in 3d. *Geophysical Research Letters*, 28(9):1891–1894, 2001.

[148] QM Lu, Bertrand Lembege, JB Tao, and S Wang. Perpendicular electric field in two-dimensional electron phase-holes: A parameter study. *Journal of Geophysical Research: Space Physics*, 113(A11), 2008.

[149] VL Krasovsky, H Matsumoto, and Y Omura. Effect of trapped-particle deficit and structure of localized electrostatic perturbations of different dimensionality. *Journal of Geophysical Research: Space Physics*, 109(A4), 2004.

[150] KJ Reitzel and GJ Morales. Dynamics of narrow electron streams in magnetized plasmas. *Physics of Plasmas*, 5(11):3806–3815, 1998.

[151] Jean-Pierre Boeuf and Laurent Garrigues. E× b electron drift instability in hall thrusters: Particle-in-cell simulations vs. theory. *Physics of Plasmas*, 25(6):061204, 2018.

[152] Thomas Charoy, Trevor Lafleur, A Alvarez Laguna, Anne Bourdon, and Pascal Chabert. The interaction between ion transit-time and electron drift instabilities and their effect on anomalous electron transport in hall thrusters. *Plasma Sources Science and Technology*, 30(6):065017, 2021.

[153] M Sengupta and A Smolyakov. Mode transitions in nonlinear evolution of the electron drift instability in a 2d annular e× b system. *Physics of Plasmas*, 27(2):022309, 2020.

[154] Zahra Asadi, Francesco Taccogna, and Mehdi Sharifian. Numerical study of electron cyclotron drift instability: Application to hall thruster. *Frontiers in Physics*, 7:140, 2019.

[155] Kentaro Hara and Sedina Tsikata. Cross-field electron diffusion due to the coupling of drift-driven microinstabilities. *Physical Review E*, 102(2):023202, 2020.

[156] Debraj Mandal, Yves Elskens, Nicolas Lemoine, and Fabrice Doveil. Cross-field chaotic transport of electrons by e× b electron drift instability in hall thruster. *Physics of Plasmas*, 27(3):032301, 2020.

[157] Arash Tavassoli, Andrei Smolyakov, Magdi Shoucri, and Raymond J Spiteri. Nonlinear regimes of the electron cyclotron drift instability in vlasov simulations. *Physics of Plasmas*, 29(3):030701, 2022.

[158] AI Sukhorukov and P Stubbe. On the bernstein–landau paradox. *Physics of Plasmas*, 4(7):2497–2507, 1997.

[159] A Ducrocq, JC Adam, A Héron, and G Laval. High-frequency electron drift instability in the cross-field configuration of hall thrusters. *Physics of Plasmas*, 13(10):102111, 2006.

[160] J. P. Boeuf and L. Garrigues. E x b electron drift instability in hall thrusters: Particle-in-cell simulations vs. theory. *Physics of Plasmas*, 25(6):061204, 2018.

[161] Krzysztof Stasiewicz. Stochastic ion and electron heating on drift instabilities at the bow shock. *Monthly Notices of the Royal Astronomical Society: Letters*, 496(1):L133–L137, 2020.

[162] Charles FF Karney and Abraham Bers. Stochastic ion heating by a perpendicularly propagating electrostatic wave. *Physical Review Letters*, 39(9):550, 1977.

[163] Charles FF Karney. Stochastic ion heating by a lower hybrid wave. *The Physics of Fluids*, 21(9):1584–1599, 1978.

[164] Charles FF Karney. Stochastic ion heating by a lower hybrid wave: Ii. *The Physics of Fluids*, 22(11):2188–2209, 1979.

[165] Vivien Croes, Antoine Tavant, Romain Lucken, Roberto Martorelli, Trevor Lafleur, Anne Bourdon, and Pascal Chabert. The effect of alternative propellants on the electron drift instability in hall-effect thrusters: Insight from 2d particle-in-cell simulations. *Physics of Plasmas*, 25(6):063522, 2018.

[166] Vivien Croes, Trevor Lafleur, Zdeněk Bonaventura, Anne Bourdon, and Pascal Chabert. 2d particle-in-cell simulations of the electron drift instability and associated anomalous electron transport in hall-effect thrusters. *Plasma Sources Science and Technology*, 26(3):034001, 2017.

[167] M Shoucri. *Numerical Solution of Hyperbolic Differential Equations*. Nova Science Pub Incorporated, 2008.

[168] A. Smolyakov, T. Zintel, L. Couedel, D. Sydorenko, A. Umnov, E. Sorokina, and N. Marusov. Anomalous electron transport in one-dimensional electron cyclotron drift turbulence. *Plasma Physics Reports*, 46(5):496–505, 2020.

[169] Sedina Tsikata, N Lemoine, V Pisarev, and DM Gresillon. Dispersion relations of electron density fluctuations in a hall thruster plasma, observed by collective light scattering. *Physics of Plasmas*, 16(3):033506, 2009.

[170] Sedina Tsikata, Cyrille Honoré, N Lemoine, and DM Grésillon. Three-dimensional structure of electron density fluctuations in the hall thruster plasma: E× b mode. *Physics of Plasmas*, 17(11):112110, 2010.

[171] Robert H Kraichnan. Inertial ranges in two-dimensional turbulence. *The Physics of Fluids*, 10(7):1417–1423, 1967.

[172] Shiyi Chen, Robert E Ecke, Gregory L Eyink, Michael Rivera, Minping Wan, and Zuoli Xiao. Physical mechanism of the two-dimensional inverse energy cascade. *Physical Review Letters*, 96(8):084502, 2006.

[173] Akira Hasegawa, Carol G Maclennan, and Yuji Kodama. Nonlinear behavior and turbulence spectra of drift waves and rossby waves. *The Physics of Fluids*, 22(11):2122–2129, 1979.

[174] Hua Xia and MG Shats. Inverse energy cascade correlated with turbulent-structure generation in toroidal plasma. *Physical Review Letters*, 91(15):155001, 2003.

[175] T. H. Dupree. Theory of phase-space density holes. *Physics of Fluids*, 25(2):277–289, 1982.

[176] B. Eliasson and P. K. Shukla. Formation and dynamics of coherent structures involving phase-space vortices in plasmas. *Physics Reports*, 422(6):225–290, 2006.

[177] Nakul Nuwal, Igor D. Kaganovich, and Deborah A. Levin. Excitation of long electrostatic solitary waves in ion beam neutralization process. *Physics of Plasmas*, 29(10):100702, 2022.

[178] Martin Lampe, Wallace M Manheimer, John B McBride, and Joseph H Orens. Anomalous resistance due to cross-field electron-ion streaming instabilities. *The Physics of Fluids*, 15(12):2356–2362, 1972.

[179] J-L Vay, Cameron GR Geddes, Estelle Cormier-Michel, and David P Grote. Numerical methods for instability mitigation in the modeling of laser wakefield accelerators in a lorentz-boosted frame. *Journal of Computational Physics*, 230(15):5908–5929, 2011.

[180] Michel Mehrenberger, Christophe Steiner, Luca Marradi, Nicolas Crouseilles, Eric Sonnendrücker, and Bedros Afeyan. Vlasov on gpu (vog project). In *ESAIM: Proceedings*, volume 43, pages 37–58. EDP Sciences, 2013.

[181] Alexander J Klimas and Adolfo F Viñas. Absence of recurrence in fourier–fourier transformed vlasov–poisson simulations. *Journal of Plasma Physics*, 84(4), 2018.

[182] JD Callen and GE Guest. Electromagnetic effects on electrostatic modes in a magnetized plasma. *Nuclear Fusion*, 13(1):87, 1973.

[183] Zachariah A Brown and Benjamin A Jorns. Spatial evolution of small wavelength fluctuations in a hall thruster. *Physics of Plasmas*, 26(11):113504, 2019.

[184] DW Forslund, RL Morse, and CW Nielson. Electron cyclotron drift instability. *Physical Review Letters*, 25(18):1266, 1970.

[185] Thurman Henry Dupree. A perturbation theory for strong plasma turbulence. *The Physics of Fluids*, 9(9):1773–1782, 1966.

[186] CT Dum and RN Sudan. Saturation of nonlinear explosive instabilities. *Physical Review Letters*, 23(20):1149, 1969.

[187] Thomas Charoy, Trevor Lafleur, Antoine Tavant, Pascal Chabert, and A Bourdon. A comparison between kinetic theory and particle-in-cell simulations of anomalous electron transport in e× b plasma discharges. *Physics of Plasmas*, 27(6):063510, 2020.

[188] F. Taccogna, P. Minelli, Z. Asadi, and G. Bogopolsky. Numerical studies of the exb electron drift instability in hall thrusters. *Plasma Sources Science & Technology*, 28(6):64002–64002, 2019.

[189] Igor D Kaganovich, Andrei Smolyakov, Yevgeny Raitses, Eduardo Ahedo, Ioannis G Mikellides, Benjamin Jorns, Francesco Taccogna, Renaud Gueroult, Sedina Tsikata, Anne Bourdon, et al. Physics of e× b discharges relevant to plasma propulsion and similar technologies. *Physics of Plasmas*, 27(12):120601, 2020.

[190] F. Califano, G. Manfredi, and F. Valentini. Special issue: The vlasov equation, from space to laboratory plasmas. *Journal of Plasma Physics*, 82(6):701820603, 2016.

[191] K. Hara and K. Hanquist. Test cases for grid-based direct kinetic modeling of plasma flows. *Plasma Sources Science & Technology*, 27(6):065004, 2018.

[192] Marilyn Jimenez. 2d3v particle-in-cell simulations of electron cyclotron drift instability and anomalous electron transport in $e \times b$ plasmas. Master's thesis, University of Saskatchewan, 2021.

[193] Arash Tavassoli, Mina Papahn Zadeh, Andrei Smolyakov, Magdi Shoucri, and Raymond J Spiteri. The electron cyclotron drift instability: a comparison of particle-in-cell and continuum vlasov simulations. *arXiv preprint arXiv:2211.05892*, 2022.

[194] Robert R Arslanbekov, Vladimir I Kolobov, and Anna A Frolova. Kinetic solvers with adaptive mesh in phase space. *Physical Review E*, 88(6):063301, 2013.

[195] Vladimir Kolobov, Robert Arslanbekov, and Dmitry Levko. Kinetic solvers with adaptive mesh in phase space for low-temperature plasmas. In *Journal of Physics: Conference Series*, volume 1225, page 012016. IOP Publishing, 2019.

[196] Nicolas Crouseilles, Guillaume Latu, and Eric Sonnendrücker. A parallel vlasov solver based on local cubic spline interpolation on patches. *Journal of Computational Physics*, 228(5):1429–1446, 2009.

[197] Nicolas Crouseilles, Michel Mehrenberger, and Eric Sonnendrücker. Conservative semi-lagrangian schemes for vlasov equations. *Journal of Computational Physics*, 229(6):1927–1953, 2010.

[198] Takayuki Umeda, Yasuhiro Nariyuki, and Daichi Kariya. A non-oscillatory and conservative semi-lagrangian scheme with fourth-degree polynomial interpolation for solving the vlasov equation. *Computer Physics Communications*, 183(5):1094–1100, 2012.

[199] Lukas Einkemmer and Alexander Ostermann. Convergence analysis of a discontinuous galerkin/strang splitting approximation for the vlasov–poisson equations. *SIAM Journal on Numerical Analysis*, 52(2):757–778, 2014.

[200] Lukas Einkemmer. A study on conserving invariants of the vlasov equation in semi-lagrangian computer simulations. *Journal of Plasma Physics*, 83(2), 2017.

[201] Lukas Einkemmer. A performance comparison of semi-lagrangian discontinuous galerkin and spline based vlasov solvers in four dimensions. *Journal of Computational Physics*, 376:937–951, 2019.

[202] Lukas Einkemmer. Semi-lagrangian vlasov simulation on gpus. *Computer Physics Communications*, 254:107351, 2020.

[203] A Sandroos, Ilja Honkonen, Sebastian von Alfthan, and Minna Palmroth. Multi-gpu simulations of vlasov's equation using vlasiator. *Parallel Computing*, 39(8):306–318, 2013.

[204] W Villafana, G Fubiani, L Garrigues, G Vigot, B Cuenot, and O Vermorel. 3d particle-in-cell modeling of anomalous electron transport driven by the electron drift instability in hall thrusters. In *37th International Electric Propulsion Conference (IEPC-2022)*, 2022.

[205] Joseph Theis, Gregory Werner, Thomas Jenkins, and John Cary. Speed-limited particle-in-cell simulations of hall thrusters in 3d. In *APS Division of Plasma Physics Meeting Abstracts*, volume 2021, pages JO08–006, 2021.

[206] Andrew Powis, Johan Carlsson, Stephane Ethier, Alexander Khaneles, Grant Johnson, Maxwell Rosen, and Igor Kaganovich. An open source, three-dimensional kinetic code for modelling low-temperature plasmas on modern supercomputing architectures. *Bulletin of the American Physical Society*, 2022.

[207] Andrew Tasman Powis. *Particle Methods for Modeling Magnetospheric Diagnostics and Low-Temperature Plasma Physics*. PhD thesis, Princeton University, 2021. Accessed: February 24, 2023.

Appendix A

Convergence of the Vlasov simulation

In Fig. 5.8, we showed that, in the nonlinear regime of the ECDI, the electrostatic energy and the temperature were much higher in the PIC simulations than in the Vlasov simulations. The same trend can also be seen in the anomalous transport results of Fig. 5.11. We also showed that in those figures, the PIC results do not converge to the Vlasov results, even for $N_{ppc} = 10^4$. However, in those figures, we did not show the convergence of the Vlasov simulations with respect to the velocity grid, which is somewhat similar to the convergence of PIC with respect to the number of macroparticles. In Fig. A.1, we can see that the electrostatic energy, the temperature, and the anomalous current of Vlasov results are in good agreement for sufficiently small ΔV. We note that for producing the results of the Chapter 5 and Chapter 6, we have used the maximum resolution shown in Fig. A.1. It is possible that by increasing the N_{ppc}, in the PIC simulations, the results finally converge to the Vlasov results. However, confirming this hypothesis has a lot of computational costs and is therefore left for future studies.

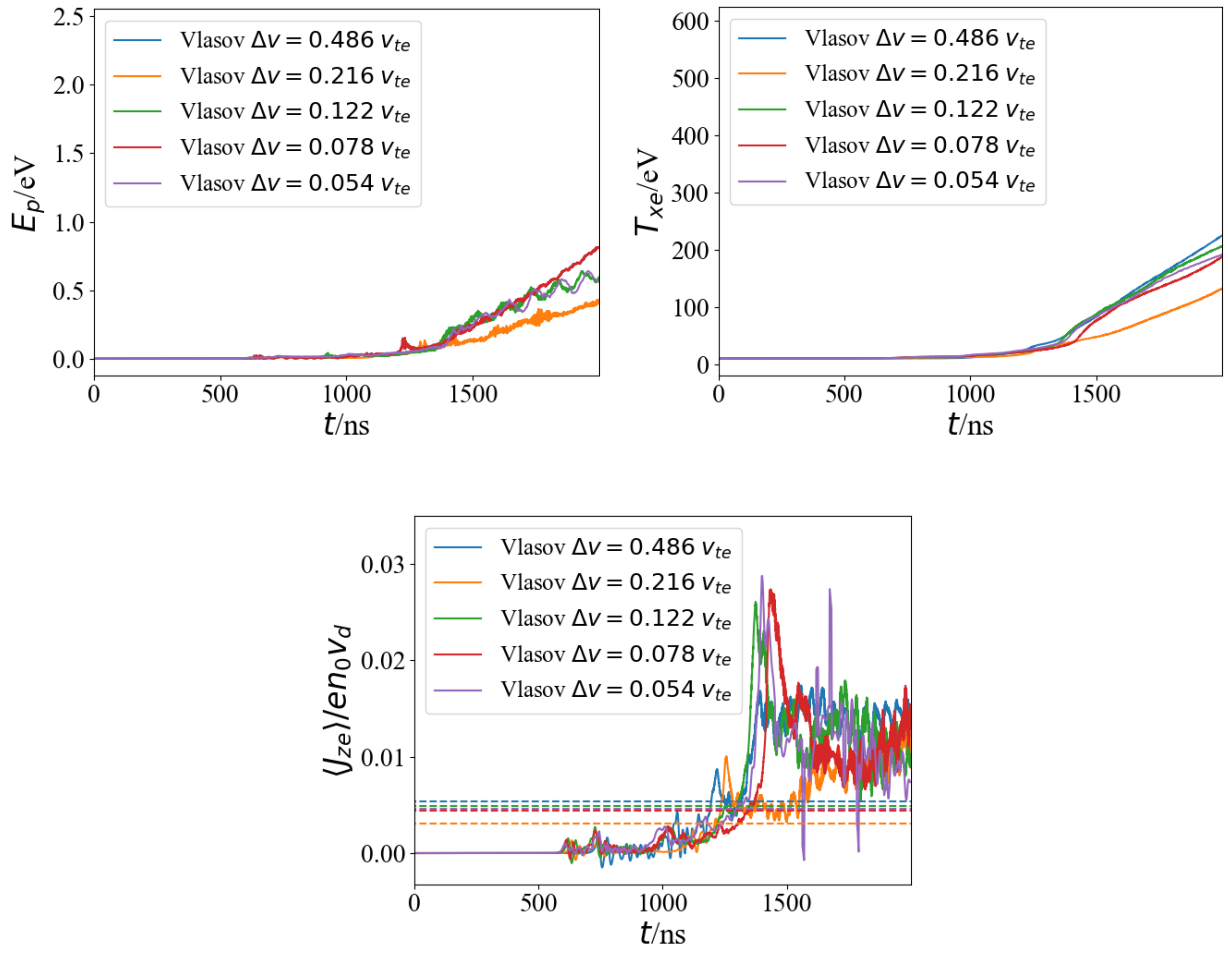

Figure A.1: The convergence of the Vlasov simulation of ECDI with respect to the velocity resolution. The parameter regime is the same as Figs. 5.8 and 5.11 .